Molecular Dynamics Simulation Studies of Dynamical Properties of Supercooled Liquids

Hideyuki Mizuno

2012

Contents

Chapter 1

General introduction

1.1 Supercooled liquids and the glass transition

Glasses are disordered materials that lack the periodicity of crystals but behave mechanically similar to solids. Such disordered solids are ubiquitous in our world, e.g., window glass, optical fiber, plastics, photovoltaic cells, and so on. Window glass is primarily composed of sand, lime, and soda and is important in building applications. Most optical fibers are composed of highly purified silica. Amorphous silicon is now used in almost all photovoltaic cells. Most engineering plastics are amorphous solids. In addition, amorphous metal alloys are used in industrial applications. Glasses clearly play a significant role in modern life.

The most common way of making a glass is to cool a liquid, while simultaneously avoiding crystallization. Figure 1.1 shows the specific volume (or enthalpy) as a function of temperature for a typical liquid at a constant pressure [32]. Cooling a liquid from high temperatures may cause crystallization to occur at the melting point T_m. This first-order phase transition usually results in a decrease in the specific volume (or the enthalpy). However, if the liquid is cooled sufficiently fast, then crystallization can be avoided [4]. A liquid at a temperature below the melting point, i.e., a liquid in the supercooled state, is called a supercooled liquid. As shown in Fig. 1.1, the specific volume, enthalpy, and other thermodynamic properties of a supercooled liquid can be obtained by extrapolation: the properties of a liquid at temperatures below the T_m are determined using the properties of a liquid at temperatures above the T_m. Thermodynamically, the crystal is regarded as the equilibrium state below the melting point T_m, whereas the supercooled liquid state is considered to be metastable. Nevertheless, the supercooled liquid can be regarded as being in the equilibrium state as long as no crystal nuclei are present. When the supercooled liquid is further cooled, the motion of the molecules decreases until the glass transition temperature (T_g) is reached, at which point the molecules no longer rearrange significantly. Molecular liquids near the T_g may require minutes or hours to reorient for molecules less than 10 Å in diameter. Liquids require a rearrangement of the molecules to find the equilibrium specific volume, which results in a deviation of the experimentally measured value of the specific volume from the equilibrium value, as shown

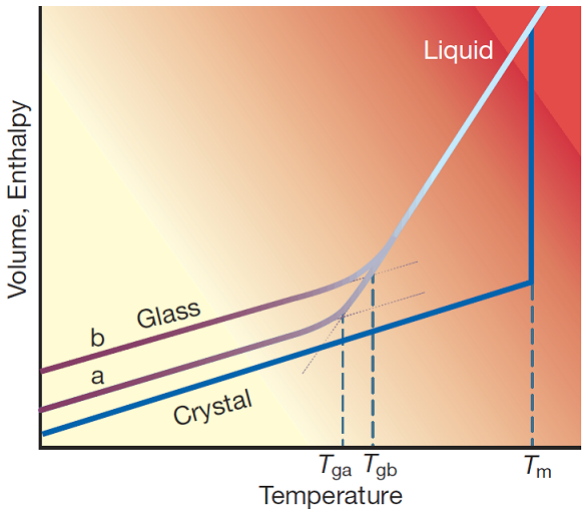

Figure 1.1: Thermodynamic properties of a typical liquid. Specific volume (or enthalpy) versus temperature at constant pressure is plotted. A slow cooling rate produces a glass transition at T_{ga}, whereas a fast cooling rate leads to a glass transition at T_{gb}. (Adapted from Ref. [32].)

in Fig. 1.1. At temperatures below the T_g, the time scale for molecular rearrangement exceeds the time scale of the experimental observation. Therefore, the structure of the liquid appears to be frozen for all practical purposes and is called a glass. It is important to emphasize that the glass transition is not a first-order phase transition different from crystallization. The glass transition is not a phase transition. The glass transition is a kinetic event with a time scale for molecular rearrangement that is longer than the experimental time scale. Glass is therefore not a crystal or liquid crystal but remains a liquid with a structure that is frozen on the time scale of experimental observation. Thermodynamically, the glass is considered to be out of equilibrium. In contrast to a supercooled liquid, a glass is continually relaxing toward a more stable state, i.e., a local free energy minimum, which is too slow to measure.

Figure 1.2 shows the temperature dependence of the viscosity η for various supercooled liquids. As the T approaches the T_g, the viscosity η increases dramatically. At temperatures near the T_g, η is extraordinarily sensitive to temperature T. In Fig. 1.2, T_g is defined as the temperature at which the viscosity η reaches 10^{13} poise. For SiO_2 and GeO_2, the temperature dependence of η is well described by the Arrhenius functionality:

$$\eta = A \exp\left(\frac{E}{k_B T}\right), \tag{1.1}$$

where A and E are temperature-independent, and k_B is the Boltzmann constant. η is reasonably

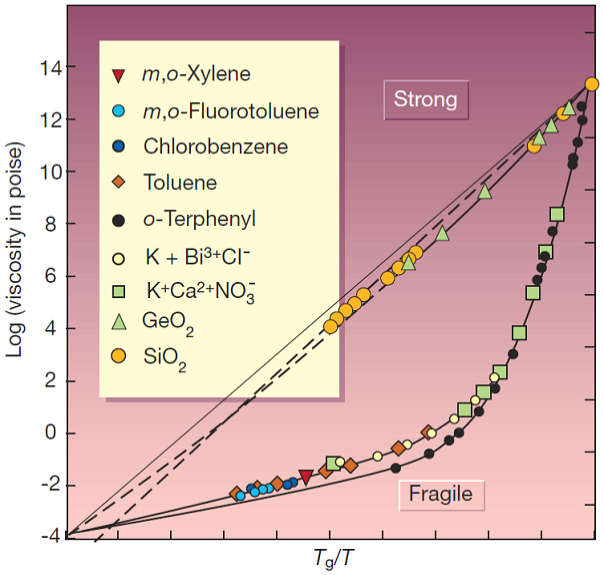

Figure 1.2: Dynamical properties of supercooled liquids. The logarithm of viscosity versus the inverse of temperature is plotted for various materials. Temperature T is scaled by glass transition temperature T_g. (Adapted from Ref. [32].)

well represented for other liquids using the Vogel-Tammann-Fulcher (VTF) equation:

$$\eta = A \exp\left(\frac{B}{T - T_0}\right), \tag{1.2}$$

where A, B, and T_0 are temperature-independent. When $T_0 = 0$, the VTF equation reduces to the Arrhenius functionality. On the basis of the temperature dependence of the viscosity η, supercooled liquids have been classified as strong or fragile [4; 5]. Strong liquids (e.g., SiO_2) show Arrhenius dependencies for the viscosities η and typically have a network structure of covalent bonds. In contrast, fragile liquids (e.g., *o*-terphenyl) show non-Arrhenius behavior and typically consist of molecules interacting through nondirectional and noncovalent interactions. In this dissertation, a fragile model liquid (soft-sphere liquid as described in Sec. 1.2.B) was used.

In addition to the equilibrium properties of the glass or the supercooled liquid, as described above, the properties that are far from equilibrium are also important and valuable. One way to make a glass or a supercooled liquid in the non-equilibrium state is to apply a steady shear flow [102; 131]. As the shear rate $\dot{\gamma}$ increases, the viscosity decreases dramatically. This non-Newtonian behavior is known as shear-thinning [17; 90; 131]. The examination of the properties of a liquid in the sheared non-equilibrium state is valuable because a broad understanding of the glass transition and the rheological behavior of dissipative system (e.g., granular materials and foams) is provided [85]. Figure 1.3 shows a schematic illustration of the phase diagram of glass

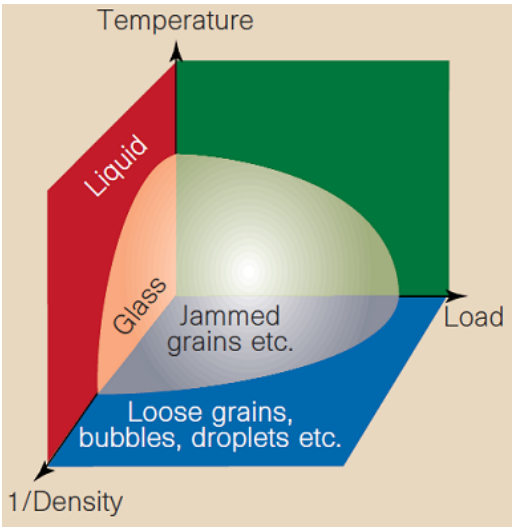

Figure 1.3: A schematic illustration of the phase diagram of glass and jamming transitions. The glass transition occurs in the inverse density and temperature plane. The jamming transition occurs in the inverse density and load plane. (Adapted from Ref. [85].)

and jamming transitions. Here, the load is also considered in addition to the temperature and the density. The load is, for example, the shear stress applied on the materials. The glass transition occurs in the (inverse) density and temperature plane. In contrast, in a dissipative system, the thermal fluctuations can be ignored, and the jamming transition occurs in the (inverse) density and load plane. Studies of a glass or supercooled liquid in the sheared non-equilibrium state can contribute to the understanding of both the glass and jamming transitions. Furthermore, studies of non-equilibrium properties can also contribute to the development of non-equilibrium statistical mechanics.

The glass transition phenomenon is well known. However, the fundamental mechanism of the glass transition is not fully understood, although a large number of theoretical, experimental, and numerical studies attempted to further our understanding [24; 32; 37]. To contribute to understanding the molecular process in the glass transition, the focus of this dissertation is the dynamical properties of a supercooled fragile liquid using molecular dynamics simulations. The quiescent equilibrium and sheared non-equilibrium states were considered to provide a broad understanding of supercooled liquids. It should be noted that in this dissertation, liquids near the T_g, i.e., the glass transition, were examined from the point of view of the liquid; however, the point of view of the solid, including the glassy state far below T_g, is also an important subject of research [6].

1.2 Simulation methods and models

1.2.A Molecular dynamics simulation

Computer simulations are very powerful tools that aid in the understanding of the properties of liquids, solids, and dense gases at the microscopic level. Simulations provide essentially the exact results for a given potential model. There are two classic approaches to computer modeling: the Monte Carlo simulation and the molecular dynamics simulation [3; 39]. The Monte Carlo simulation is designed to generate static configurations of the system, whereas the molecular dynamics simulation solves the classical equations of the motion of the particles. The Monte Carlo simulation is often more efficient for investigating the static properties of a glass, while the molecular dynamics simulation allows time-dependent phenomena to be studied. Molecular dynamics simulations were used extensively in this dissertation to examine the dynamical properties of a supercooled liquid. The dynamics of liquids become very slow in the supercooled state. Therefore, simulations were performed on the supercooled liquid over a long duration of time.

For the simulations, the system was first carefully equilibrated under canonical conditions. A duration of at least five times the structural relaxation time τ_α was used as the equilibration period to minimize the aging effects for various parameters, including the pressure and density correlation functions. Once equilibrium was established, the data were acquired under the microcanonical conditions in the quiescent equilibrium state. The following equations (Newton's equations of motion) were integrated:

$$\begin{aligned} \frac{d\boldsymbol{r}_i}{dt} &= \frac{\boldsymbol{p}_i}{m_i}, \\ \frac{d\boldsymbol{p}_i}{dt} &= \boldsymbol{F}_i, \end{aligned} \tag{1.3}$$

where $\boldsymbol{r}_i$ and $\boldsymbol{p}_i$ denote the position and the momentum of the ith particle, and $\boldsymbol{F}_i$ is the force acting on the ith particle. Figure 1.4 shows a schematic picture of the molecular dynamics simulation. In the sheared non-equilibrium state where a steady shear flow was applied, the Lees-Edwards boundary condition was used to maintain the shear flow on the supercooled liquid. The following so-called SLLOD equations of motion were also integrated:

$$\begin{aligned} \frac{d\boldsymbol{r}_i}{dt} &= \frac{\boldsymbol{p}'_i}{m_i} + \boldsymbol{r}_i \cdot \nabla \boldsymbol{u}, \\ \frac{d\boldsymbol{p}'_i}{dt} &= \boldsymbol{F}_i - \boldsymbol{p}'_i \cdot \nabla \boldsymbol{u}, \end{aligned} \tag{1.4}$$

where $\boldsymbol{u}$ is the streaming velocity, and $\boldsymbol{p}'_i = \boldsymbol{p}_i - m_i \boldsymbol{r}_i \cdot \nabla \boldsymbol{u}$ are the momentum deviations relative to the mean Couette flow of the ith particle. By using a Gaussian constraint thermostat, viscous

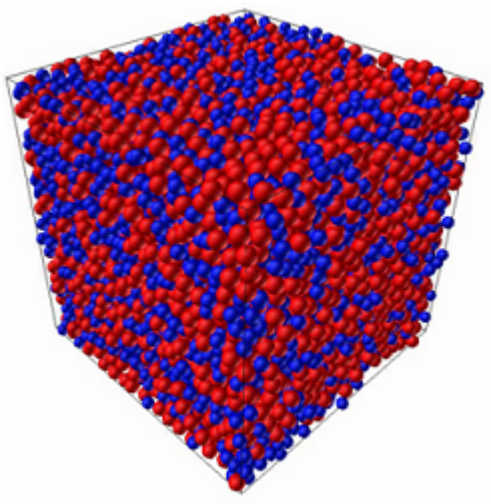

Figure 1.4: Illustration of the particle configuration in the molecular dynamics simulation. The red particles and the blue particles are the particle species 1 and 2, respectively.

heating effects were eliminated, and the temperature T was maintained, as defined in Eq. (1.5), at a desired value.

$$T = \frac{1}{3k_B N} \sum_{i=1}^{N} \frac{\boldsymbol{p}_i'}{m_i}. \tag{1.5}$$

The data were acquired and accumulated in the steady state, which can be realized after transient waiting periods. A detailed description of the molecular dynamics simulation method can be found in references [3; 39].

1.2.B Soft-sphere binary mixture

The liquid used in the simulation model was a three-dimensional soft-sphere binary mixture composed of two different atomic species, 1 and 2, with $N = N_1 + N_2$ particles. The particles interact via the following soft-sphere potential:

$$\begin{aligned} v_{ab} &= \epsilon \left(\frac{\sigma_{ab}}{r} \right)^{12}, \\ \sigma_{ab} &= \frac{\sigma_a + \sigma_b}{2}, \end{aligned} \tag{1.6}$$

where r is the distance between two particles, σ_a is the particle size, and $a, b \in 1, 2$. The interaction was truncated at $r = 3\sigma_{ab}$. Note that this model liquid is a fragile liquid. Many studies have performed molecular dynamics studies on the soft-sphere model liquids since early times [10; 11; 59; 60; 61; 65; 96; 103; 131]. The mass and size ratios were set to the following:

$$\begin{aligned} \frac{m_2}{m_1} &= 2.0, \\ \frac{\sigma_2}{\sigma_1} &= 1.2. \end{aligned} \tag{1.7}$$

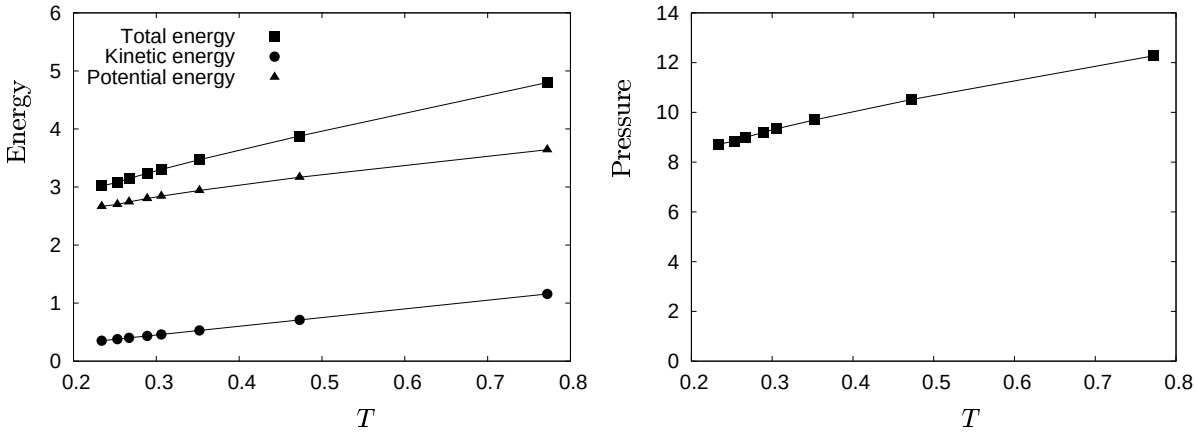

(a) Energy (b) Pressure

Figure 1.5: The T temperature dependence of (a) energy and (b) pressure in the equilibrium state.

The size ratio $\sigma_2/\sigma_1 = 1.2$ prevents crystallization and produces an amorphous state at low temperatures. The total number density ρ was fixed as follows:

$$\rho = \frac{0.8}{\sigma_1^3}. \tag{1.8}$$

The system was an equimolar mixture, i.e., $\rho_1 = \rho_2 = 0.5\rho$. The volume fraction ϕ of the particles was estimated to be the following:

$$\phi = \frac{4\pi}{3}(\sigma_1^3\rho_1 + \sigma_2^3\rho_2) = 0.57, \tag{1.9}$$

where the overlapped regions are doubly counted. The system was in a densely packed state as is visually demonstrated in Fig. 1.4. According to the Henderson and Leonard theory [10; 11; 53], a binary mixture may be fairly well mapped onto a one-component soft-sphere liquid with an effective radius defined by the following:

$$\sigma_{\text{eff}}^3 = \sum_{a,b=1,2} x_a x_b \sigma_{ab}^3, \tag{1.10}$$

where $x_1 = \rho_1/\rho = 0.5$ and $x_2 = \rho_2/\rho = 0.5$ are the compositions of the two components. As in the one-component case, the thermodynamic state is characterized by a single parameter (effective density) [10; 11; 59; 60; 61], as shown in the following equation:

$$\Gamma_{\text{eff}} = \rho \left(\frac{\epsilon}{k_B T} \right)^{1/4} \sigma_{\text{eff}}^3. \tag{1.11}$$

The freezing point of a one component system is approximately $T = 0.772$ ($\Gamma_{\text{eff}} = 1.15$) [89]. For the simulations in this dissertation, the temperature was set to be $T = 0.772 - 0.253$ ($\Gamma_{\text{eff}} = 1.15 - 1.52$). At the temperature $T = 0.253$ ($\Gamma_{\text{eff}} = 1.52$), the liquid was in the highly supercooled state.

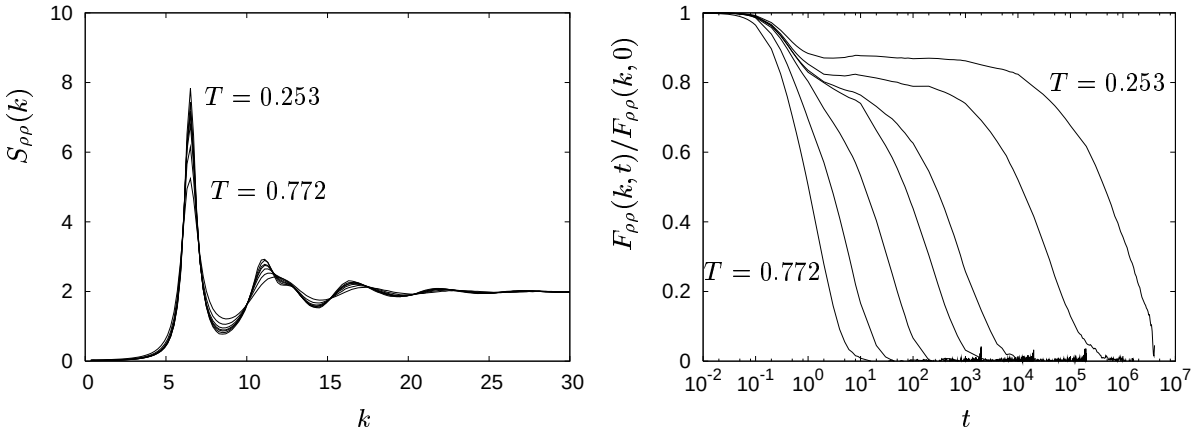

(a) Static structure factor

(b) Density time correlation function

Figure 1.6: Plots of (a) the static structure factor $S_{\rho\rho}(k)$ versus wavenumber k and (b) density time correlation function $F_{\rho\rho}(k,t)$ at $k = 2\pi$ versus time t. The temperature was $T = 0.772 - 0.253$.

Figure 1.5 shows plots of the macroscopic variables, energy and pressure. Distances, times, and temperature were measured with units of σ_1, $\tau_0 = (m_1\sigma_1^2/\epsilon)^{1/2}$, and ϵ/k_B, respectively. In this system, the potential energy is much larger than the kinetic energy, and the pressure is very high. In addition, figure 1.6 shows the static structure factor $S_{\rho\rho}(k)$ and the density correlation function $F_{\rho\rho}(k,t)$. The functions $S_{\rho\rho}(k)$ and $F_{\rho\rho}(k,t)$ are defined as the following:

$$\begin{aligned} S_{\rho\rho}(k) &= \frac{1}{N}\left\langle \rho_{\text{eff}}(k,0)\rho_{\text{eff}}(-k,0)\right\rangle, \\ F_{\rho\rho}(k,t) &= \left\langle \rho_{\text{eff}}(k,t)\rho_{\text{eff}}(-k,0)\right\rangle, \end{aligned} \tag{1.12}$$

where $\rho_{\text{eff}}(k,t)$ is a density variable representing the degree of particle packing [131] and is defined as the following:

$$\rho_{\text{eff}}(k,t) = \sigma_1^3 \sum_{j=1}^{N_1} \exp(-i\boldsymbol{k}\cdot\boldsymbol{r}_{1j}) + \sigma_2^3 \sum_{j=1}^{N_2} \exp(-i\boldsymbol{k}\cdot\boldsymbol{r}_{2j}). \tag{1.13}$$

The static structure factor $S_{\rho\rho}(k)$ has a first peak value at approximately the wavenumber $k = 2\pi$, as can be seen in Fig. 1.6(a). At small wavenumbers k, $S_{\rho\rho}(k)$ is much smaller. In this sense, the system is highly incompressible over long distances. In Fig. 1.6(b), the decay of $F_{\rho\rho}(k,t)$ is plotted at the wavenumber $k = 2\pi$ (the first-peak wavenumber of the static structure factor). The relaxation time of $F_{\rho\rho}(k,t)$ increases dramatically with decreasing temperature T, whereas the static structure factor does not significantly change with temperature. Thus, the calculations successfully simulated the dramatic decrease in molecular motion and glassy behavior.

1.3 Thesis objectives

In this dissertation, the following dynamical properties of a supercooled liquid were investigated:

- Dynamical heterogeneities
- Mechanical properties
- Acoustic properties

The quiescent equilibrium state and the sheared non-equilibrium state were considered to broadly understand the dynamical properties of a supercooled liquid. This dissertation is composed of six chapters, which are described below.

In **Chapter 2** and **3**, the dynamical heterogeneities in the equilibrium state (**Chapter 2**) and the sheared non-equilibrium state (**Chapter 3**) were examined. Dynamical heterogeneity can be characterized by three quantities: the correlation length ξ_4, the intensity χ_4, and the lifetime τ_{hetero}. All three quantities were successfully evaluated by using the correlation functions of the particle dynamics, i.e., the four-point correlation functions. In these works, the temperature dependencies of the three quantities as well as the shear rate dependencies of the three quantities were revealed. The validity of the mapping concept was also demonstrated: three quantities in the sheared state can be mapped onto those in the equilibrium state.

In **Chapter 4**, the mechanical properties in both the equilibrium and sheared non-equilibrium states were examined. The shear stress responses to the oscillating shear strains were investigated in detail. Using the simulation results, the constitutive equation describing the mechanical properties of the supercooled liquid was constructed. The relaxation behaviors of the correlation functions of the shear stress fluctuations were also examined. Furthermore, the obtained results of the shear stress responses and fluctuations allowed the fluctuation-dissipation relation in the non-equilibrium state to be discussed and the concept of an effective temperature to be tested, which the equilibrium form of the fluctuation-dissipation theorem holds when the temperature T is replaced by an effective temperature T_{eff}.

In **Chapter 5**, the acoustic properties of both the equilibrium and sheared non-equilibrium states were examined. The behavior of the transverse sound wave was investigated in detail. By using the transverse current spectrum, the quantification of the dispersion relation and the sound attenuation was possible. A physical explanation of the obtained simulation results was provided

using the continuum mechanics with the constitutive equation constructed in **Chapter 4** and related the acoustic properties and the mechanical properties.

In **Chapter 6**, the thesis is summarized.

Through these investigations of the dynamical properties mentioned above, the major interests were the following:

- Length and time scales in supercooled liquids
- Non-equilibrium properties of supercooled liquids

The first subject, length and time scales in supercooled liquids, was investigated in **Chapter 2** and **3**, whereas the non-equilibrium properties of supercooled liquids was explored in **Chapter 3**, **4**, and **5**.

Chapter 2

Dynamical heterogeneity in a supercooled liquid under quiescent condition

2.1 Introduction

As liquids are cooled toward the glass transition temperature T_g, a drastic slowing occurs for dynamical properties such as the structural relaxation time, the diffusion constant, and the viscosity, while only small changes are detected in static properties [32; 37]. Despite the extremely widespread use of glass in industry, the formation process and dynamic properties of this material are still poorly understood. The goal of theoretical investigations of the glass transition is to understand the universal mechanism that gives rise to the drastic slowing of dynamical properties. Numerous studies have attempted to explain the fundamental mechanisms of the slowing of the dynamics observed in fragile glass (i.e., the sharp increase in viscosity near the glass transition). However, the physical mechanisms behind this slowing have not been successfully identified.

Recently, "dynamical heterogeneities" in glass-forming liquids have attracted much attention. The dynamics of glass-forming liquids are not only drastically slow but also become progressively more heterogeneous upon approaching the glass transition. Dynamical heterogeneities have been detected and visualized through simulations of soft-sphere systems [65; 96; 104; 128; 131; 132], hard-sphere systems [34], and Lennard-Jones (LJ) systems [35], and through experiments performed on colloidal dispersions using particle-tracking techniques [71; 87; 127]. Insight into the mechanisms of dynamical heterogeneities will lead to a better understanding of the slowing of the dynamics near the glass transition.

The properties of dynamical heterogeneity can be characterized by the following three quantities: the correlation length, the intensity, and the lifetime. In a system displaying dynamical heterogeneity, the particles can be divided into "slow" and "fast" sub-sets. The slow and fast particles form cooperative correlated regions, and these slow and fast regions migrate in space over time. The three quantities (the correlation length, the intensity, and the lifetime) can describe the static and dynamic properties of the slow and fast regions. The intensity measures the average variance of the slow and fast regions, and the correlation length characterizes the spatial extent of

the slow and fast regions. The lifetime represents the time scale at which the slow and fast regions migrate in the space.

The correlation length, intensity, and lifetime can be investigated using the correlation functions of the particle dynamics. In fact, we can evaluate the correlation length ξ_4 and the intensity χ_4 by calculating the four-point correlation functions that correspond to the static structure factors of the particle dynamics. Several simulations [12; 25; 33; 41; 42; 49; 69; 70; 80; 104; 117; 119; 131], experiments [15; 28; 36; 97], and mode-coupling theories [20; 21; 118] have estimated ξ_4 and χ_4 using four-point correlation functions and have revealed that ξ_4 and χ_4 increase with decreasing temperature (or an increase in the volume fraction in the case of hard-sphere systems). Furthermore, we can quantify the lifetime $\tau_{\rm hetero}$ using the multiple-time extensions of the four-point correlation functions (i.e., the multi-time correlation functions) that correspond to the time correlation functions of the particle dynamics. Recent simulations have quantified $\tau_{\rm hetero}$ using multi-time correlation functions [40; 72; 73; 81; 132]. Various experiments, including photobleaching techniques and nuclear magnetic resonance, have also measured $\tau_{\rm hetero}$ [9; 36; 108; 110; 111; 125; 126]. It was reported that $\tau_{\rm hetero}$ increases dramatically with decreasing temperature or an increase in the volume fraction and can exceed the α-relaxation time near the glass transition.

As mentioned above, there have been many studies on the correlation length, the intensity, and the lifetime of dynamical heterogeneity near the glass transition. However, knowledge of and measurements relating to the lifetime are still limited. Moreover, individual studies have been restricted to only the correlation length and the intensity or only the lifetime, and the relationship between the length and time scales of dynamical heterogeneity remains controversial despite its importance [72; 73].

The aim of the present study is to examine all the three quantities (the correlation length, the intensity, and the lifetime of dynamical heterogeneity) consistently from a single order parameter. We performed molecular-dynamics (MD) simulations and investigated dynamical heterogeneity using the correlation functions of the particle dynamics. We quantified the correlation length $\xi_4(t)$, the intensity $\chi_4(t)$, and the lifetime $\tau_{\rm hetero}(t)$ in two different time intervals: the α-relaxation time τ_α and the time $\tau_{\rm ngp}$ at which the non-Gaussian parameter of the Van Hove self-correlation function is maximized. Furthermore, we examined the time-interval dependence of the lifetime $\tau_{\rm hetero}(t)$ to understand the lifetime and the dynamic properties of dynamical heterogeneity in more detail.

The chapter is organized as follows. In Sec. 2.2, we explain the correlation functions of the

particle dynamics. We show that dynamical heterogeneity can be systematically examined using the correlation functions of the particle dynamics. In Sec. 2.3, we briefly review our MD simulation and present some results from conventional density correlation functions. In Secs. 2.4 and 2.5, the results for dynamical heterogeneity are presented. In Sec. 2.4, we first show three quantities, the correlation length, the intensity, and the lifetime, which are consistently calculated from a single order parameter. In Sec. 2.5, we next present the time-interval dependence of the lifetime $\tau_{\rm hetero}(t)$. In Sec. 2.6, we summarize our results.

2.2 Correlation functions of particle dynamics

As we mentioned, dynamical heterogeneity can be characterized by three quantities: the correlation length, the intensity, and the lifetime. In this section, we introduce the correlation functions of the particle dynamics and demonstrate that these three quantities can be systematically evaluated in terms of the correlation functions of the particle dynamics.

The conventional two-point correlation function $F(k,t)$ represents the correlation of local fluctuations $\delta n(\boldsymbol{k},t)$ with some order parameter, such as particle density. The expression $\delta n(\boldsymbol{k},t)$ is the Fourier component $\boldsymbol{k}$ of the fluctuations at time t, and $F(k,t) = \langle \delta n(\boldsymbol{k},t)\delta n(-\boldsymbol{k},0)\rangle$, where $k = |\boldsymbol{k}|$. When $t = 0$, $S(k) \equiv F(k,t=0)$ is the spatial correlation of $\delta n(\boldsymbol{k},0)$ (i.e., the static structure factor), and we can examine the static structure of the order parameter by the wavenumber dependence of $S(k)$. When $t > 0$, $F(k,t)$ describes the particle dynamics in the time interval $[0,t]$, averaged over the initial time and space. As the time interval t increases, $F(k,t)$ decays in the stretched exponential form,

$$\frac{F(k,t)}{F(k,0)} \sim \exp\left(-\left(\frac{t}{\tau(k)}\right)^{\beta}\right), \tag{2.1}$$

where $\tau(k)$ is the relaxation time of the two-point correlation function that represents the characteristic time scale of the average particle dynamics.

To examine the structure and motion of spatially heterogeneous dynamics, we must calculate the correlation of the local fluctuations, $\delta Q_k(\boldsymbol{q},t_0,t)$, in the particle dynamics. The expression $\delta Q_k(\boldsymbol{q},t_0,t)$ is the Fourier component $\boldsymbol{q}$ of the fluctuations in the particle dynamics that are associated with a microscopic wavenumber k in the time interval $[t_0, t_0+t]$. $F(k,t)$ is equal to $Q_k(\boldsymbol{q},t_0,t)$ averaged over the initial time t_0 and space, i.e., $F(k,t) \sim \langle Q_k(\boldsymbol{q},t_0,t)\rangle$. The correlation function defined by

$$S_{4,k}(q,t) = \langle \delta Q_k(\boldsymbol{q},0,t)\delta Q_k(-\boldsymbol{q},0,t)\rangle, \tag{2.2}$$

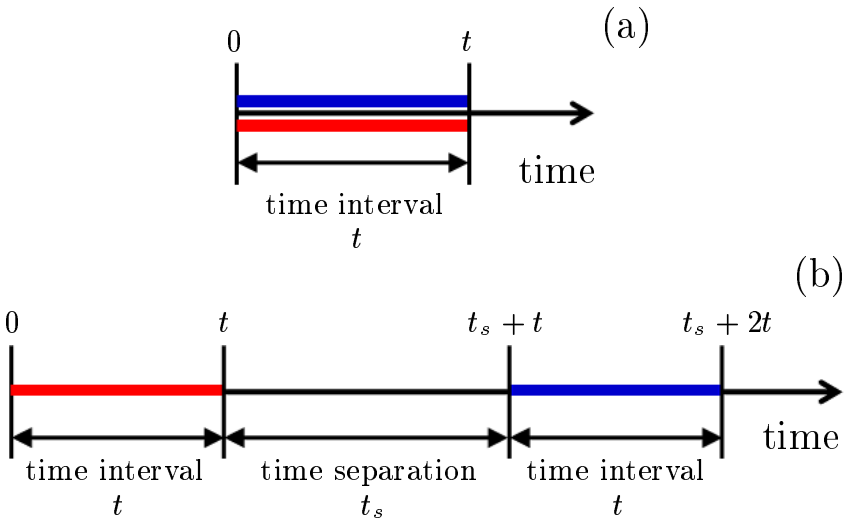

Figure 2.1: Schematic illustration of the time configuration of the correlation functions of the particle dynamics: (a) the spatial correlation function of the particle dynamics in the time interval $[0, t]$ and (b) the time correlation function of the particle dynamics between the two time intervals $[0, t]$ and $[t_s + t, t_s + 2t]$.

represents the spatial correlation of the particle dynamics in the time interval $[0, t]$. The time configuration of $S_{4,k}(q, t)$ is schematically illustrated in Fig. 2.1(a). $S_{4,k}(q, t)$ is the four-point correlation function. We can examine the structure of the particle dynamics by the wavenumber dependence of $S_{4,k}(q, t)$. At small wavenumbers of q, $S_{4,k}(q, t)$ can be approximated by the simple Ornstein-Zernike (OZ) form [80; 131],

$$S_{4,k}(q, t) = \frac{\chi_{4,k}(t)}{1 + q^2 \xi_{4,k}(t)^2}, \tag{2.3}$$

where $\xi_{4,k}(t)$ is the correlation length of the heterogeneous dynamics and $\chi_{4,k}(t)$ is the intensity of the heterogeneous dynamics, which is the long-wavelength limit of $S_{4,k}(q, t)$, i.e., $\chi_{4,k}(t) = \lim_{q \to 0} S_{4,k}(q, t)$. Note that $\chi_{4,k}(t)$ is termed the four-point dynamical susceptibility. According to previous studies [41; 42; 69; 70], to quantify $\xi_{4,k}(t)$ and $\chi_{4,k}(t)$ accurately, we need to use a large system or determine $\chi_{4,k}(t)$ through other means (not OZ fitting). In their work [41; 42], E. Flenner et al. claimed that accurate determinations of $\xi_{4,k}(t)$ and $\chi_{4,k}(t)$ can be made by fitting $S_{4,k}(q, t)$ to the OZ form in the range of $q\xi_{4,k}(t) < 1.5$. They used a large system composed of 8×10^4 particles to obtain accurate fits for the OZ form. In the present study, we used a large system with 10^5 particles to fit $S_{4,k}(q, t)$ to the OZ form accurately and obtain the values of $\xi_{4,k}(t)$ and $\chi_{4,k}(t)$.

Furthermore, the time correlation function defined by

$$F_{4,k}(q,t_s,t) = \langle \delta Q_k(\boldsymbol{q},t_s+t,t)\delta Q_k(-\boldsymbol{q},0,t)\rangle, \tag{2.4}$$

represents the correlation of the particle dynamics between the two time intervals $[0,t]$ and $[t_s+t,t_s+2t]$. The value t_s is the time separation between the two time intervals $[0,t]$ and $[t_s+t,t_s+2t]$. The time configuration of $F_{4,k}(q,t_s,t)$ is schematically illustrated in Fig. 2.1(b). $F_{4,k}(q,t_s,t)$ is the multiple-time extension of the four-point correlation function [72; 73]. As the time separation t_s increases, $F_{4,k}(q,t_s,t)$ with fixed t decays in the stretched exponential form,

$$\frac{F_{4,k}(q,t_s,t)}{F_{4,k}(q,0,t)} \sim \exp\left(-\left(\frac{t_s}{\tau_{4,k}(q,t)}\right)^c\right), \tag{2.5}$$

where $\tau_{4,k}(q,t)$ is the relaxation time of the correlation of the particle dynamics. We determined the lifetime $\tau_{\rm hetero}(t)$ of the heterogeneous dynamics as $\tau_{4,k}(q,t)$ at $q = 0.38$. We need longer trajectories of the simulations to quantify $\tau_{\rm hetero}(t)$ than to quantify $\xi_{4,k}(t)$ and $\chi_{4,k}(t)$. In the present study, we used a smaller system with 10^4 particles to calculate $\tau_{\rm hetero}(t)$. As explained above, we can systematically evaluate the correlation length, the intensity, and the lifetime of dynamical heterogeneity by calculating the correlation functions of the particle dynamics.

2.3 Simulation model and results from density correlation functions

2.3.A Simulation model

We performed MD simulations in three dimensions on binary mixtures of two different atomic species, 1 and 2, with a cube of constant volume V as the basic cell, surrounded by periodic boundary image cells. The particles interacted via their soft-sphere potentials, $v_{ab}(r) = \epsilon(\sigma_{ab}/r)^{12}$; where r is the distance between two particles, $\sigma_{ab} = (\sigma_a+\sigma_b)/2$, and $a,b \in 1,2$. The interaction was truncated at $r = 3\sigma_{ab}$. The mass ratio was $m_2/m_1 = 2$, and the diameter ratio was $\sigma_2/\sigma_1 = 1.2$. This diameter ratio avoided system crystallization and ensured that an amorphous supercooled state formed at low temperatures [89]. As mentioned in Sec. 2.2, we used two systems: a small system with $N_1 = N_2 = 5\times10^3$ ($N = N_1+N_2 = 10^4$) particles and a large system with $N_1 = N_2 = 5\times10^4$ ($N = N_1+N_2 = 10^5$) particles. The large system was used to quantify the correlation length $\xi_{4,k}(t)$ and the intensity $\chi_{4,k}(t)$, and the small system was used to quantify the lifetime $\tau_{\rm hetero}(t)$. In the present study, the following dimensionless units are used: length, σ_1; temperature, ϵ/k_B; and time, $\tau_0 = (m_1\sigma_1^2/\epsilon)^{1/2}$. The particle density was fixed at the high value of $\rho = N/V = 0.8$. The system

lengths were $L = V^{1/3} = 23.2$ and 50.0 for the small and large systems, respectively. Simulations were performed at $T = 0.772,\ 0.473,\ 0.352,\ 0.306,\ 0.289,\ 0.267$, and 0.253. Note that the freezing point of the corresponding one-component model is approximately $T = 0.772$ ($\Gamma_{\rm eff} = 1.15$) [89]. Here, $\Gamma_{\rm eff}$ is the effective density, which is a single parameter characterizing this model. At $T = 0.253$ ($\Gamma_{\rm eff} = 1.52$), the system is in a highly supercooled state. We used the leapfrog algorithm with time steps of 0.005 when integrating the Newtonian equation of motion. At each temperature, the system was carefully equilibrated under the canonical condition so that no appreciable aging effect was detected for various quantities, including the pressure and the density correlation function. Once equilibrium was established, data were taken under the microcanonical condition. The length of the data collection runs was at least 100 times the α-relaxation time, τ_α, for the small system and 10 times τ_α for the large system. Information regarding this model, such as the static structure factor, the intermediate scattering function, and the mean square displacement, can be found in previous works [75; 131].

2.3.B Single-particle and collective-particle diffusive motion

Before showing the results for dynamical heterogeneity in supercooled liquids, we present some results from an investigation of the average particle dynamics using conventional density correlation functions. Let us consider the density correlation functions $F_{sa}(k,t)$ and $F_a(k,t)$ ($a \in 1, 2$), defined by

$$\begin{aligned} F_{sa}(k,t) &= \left\langle \frac{1}{N_a} \sum_{j=1}^{N_a} \delta n_{aj}(\boldsymbol{k},t) \delta n_{aj}(-\boldsymbol{k},0) \right\rangle, \\ F_a(k,t) &= \langle \delta n_a(\boldsymbol{k},t) \delta n_a(-\boldsymbol{k},0) \rangle, \end{aligned} \tag{2.6}$$

where $\delta n_{aj}(\boldsymbol{k},t) = \exp[-i\boldsymbol{k} \cdot \boldsymbol{r}_{aj}(t)]$ is the Fourier component $\boldsymbol{k}$ of the tagged particle density fluctuations of particle species a, and $\delta n_a(\boldsymbol{k},t) = \sum_{j=1}^{N_a} \exp[-i\boldsymbol{k} \cdot \boldsymbol{r}_{aj}(t)]$ is the Fourier component $\boldsymbol{k}$ of the density fluctuations of particle species a. The terms $F_{sa}(k,t)$ and $F_a(k,t)$ describe the single-particle and collective-particle motion, respectively [53]. We calculated $F_{sa}(k,t)$ and $F_a(k,t)$ for a wide range of wavenumbers, $k = 0.35 - 40$. As seen in Eq. (2.1), $F_{sa}(k,t)$ and $F_a(k,t)$ decay in the stretched exponential form,

$$\begin{aligned} \frac{F_{sa}(k,t)}{F_{sa}(k,0)} &= \exp\left(-\left(\frac{t}{\tau_{sa}(k)} \right)^{\beta_s} \right), \\ \frac{F_a(k,t)}{F_a(k,0)} &= \exp\left(-\left(\frac{t}{\tau_{ca}(k)} \right)^{\beta_c} \right), \end{aligned} \tag{2.7}$$

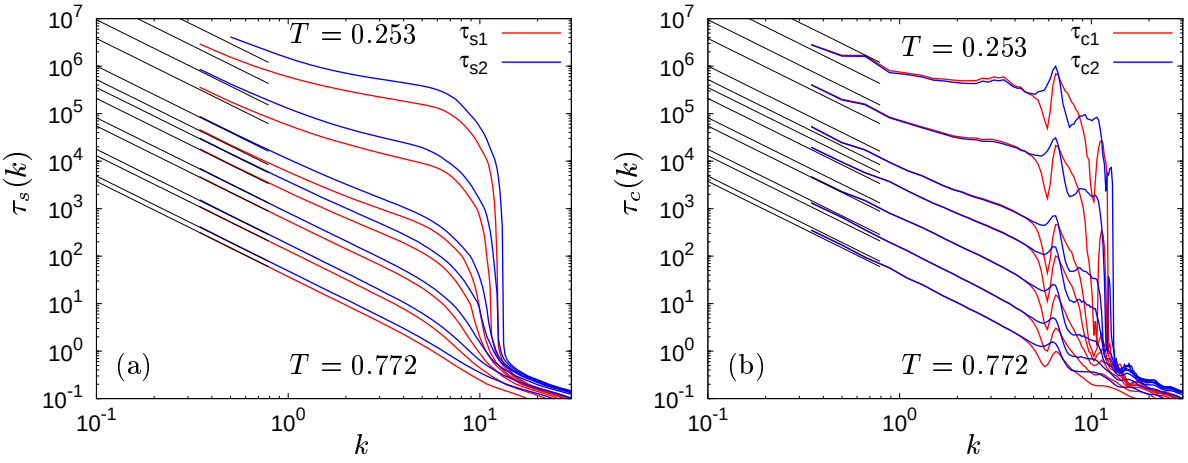

Figure 2.2: The wavenumber dependence of (a) $\tau_{sa}(k)$ and (b) $\tau_{ca}(k)$ for particle species $a = 1$ and 2. Temperatures are $0.772 - 0.253$ from the lowest curve to the highest. The black line is $\tau_{sa}(k) = D_{sa}^{-1}k^{-2}$, where D_{sa} is the diffusion constant of the single-particle motion calculated from the mean square displacement.

where $\tau_{sa}(k)$ and $\tau_{ca}(k)$ are the wavenumber-dependent relaxation times of $F_{sa}(k,t)$ and $F_a(k,t)$, respectively.

In Fig. 2.2, $\tau_{sa}(k)$ and $\tau_{ca}(k)$ are plotted for particle species 1 and 2 as functions of the wavenumber k. In Fig. 2.2(a), $\tau_{sa}(k)$ approaches $\tau_{sa}(k) = D_{sa}^{-1}k^{-2}$ at small wavenumbers k, where D_{sa} is the diffusion constant of the single-particle motion of particle species a. The term D_{sa} is calculated by $D_{sa} = \lim_{t\to\infty}\langle[\Delta \boldsymbol{r}_a(t)]^2\rangle/6t$; where $\langle[\Delta \boldsymbol{r}_a(t)]^2\rangle$ is the mean square displacement of particle species a; $\langle[\Delta \boldsymbol{r}_a(t)]^2\rangle = \langle\sum_{j=1}^{N_a}[\Delta \boldsymbol{r}_{aj}(t)]^2/N_a\rangle$; $\Delta \boldsymbol{r}_{aj}(t) = \boldsymbol{r}_{aj}(t) - \boldsymbol{r}_{aj}(0)$. The diffusion constant of particle species 1 is larger than that of particle species 2 at every temperature. However, $\tau_{ca}(k)$ also approaches $\tau_{ca}(k) \sim k^{-2}$ at small k in Fig. 2.2(b). This behavior indicates that the collective-particle motion is also diffusive at large length scales, and we can define the diffusion constant of the collective-particle motion D_a as

$$D_a = \lim_{k\to 0} \tau_{ca}^{-1}(k)k^{-2}. \tag{2.8}$$

We can see that D_1 and D_2 are almost identical between D_{s1} and D_{s2} in Fig. 2.2(b).

2.3.C Correlation between static structure factor and relaxation time

Next, we consider a density variable defined by

$$\rho_{\rm eff}(\boldsymbol{k},t) = \sigma_1^3 n_1(\boldsymbol{k},t) + \sigma_2^3 n_2(\boldsymbol{k},t), \tag{2.9}$$

that represents the degree of particle packing and is the effective one-component density of our binary mixture [131]. We calculated the static structure factor $S_{\rho\rho}(k)$ and the time correlation

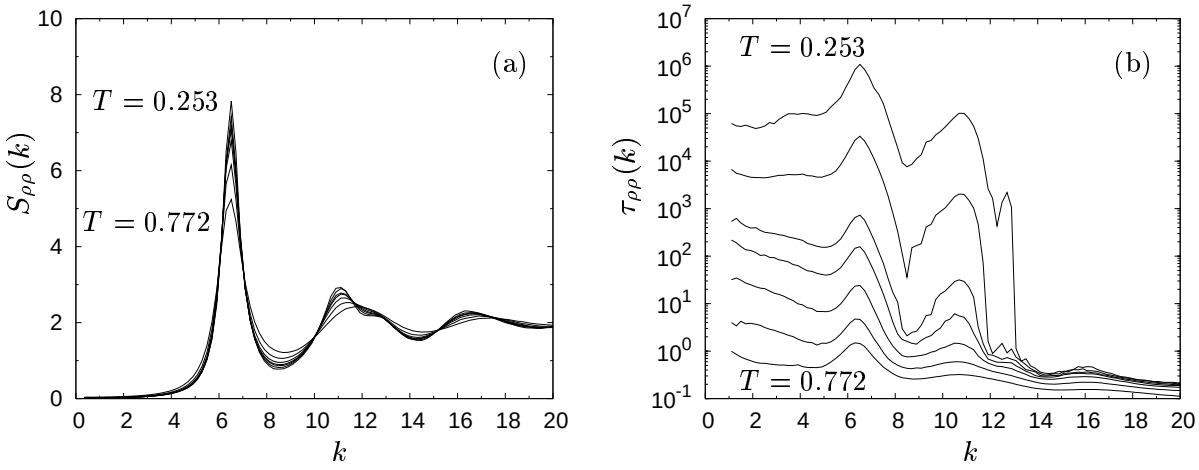

Figure 2.3: The wavenumber dependence of (a) $S_{\rho\rho}(k)$ and (b) $\tau_{\rho\rho}(k)$. The temperatures are $0.772 - 0.253$ from the lowest curve to the highest.

function $F_{\rho\rho}(k,t)$, defined by

$$\begin{aligned} S_{\rho\rho}(k) &= \frac{1}{N}\langle \delta\rho_{\rm eff}(\boldsymbol{k},0)\delta\rho_{\rm eff}(-\boldsymbol{k},0)\rangle, \\ F_{\rho\rho}(k,t) &= \langle \delta\rho_{\rm eff}(\boldsymbol{k},t)\delta\rho_{\rm eff}(-\boldsymbol{k},0)\rangle. \end{aligned} \tag{2.10}$$

The terms $S_{\rho\rho}(k)$ and $F_{\rho\rho}(k,t)$ represent the static structure and the average particle dynamics of the effective one-component fluids, respectively. Note that $F_{\rho\rho}(k,t)$ decays in the stretched exponential form with the relaxation time $\tau_{\rho\rho}(k)$, as in Eq. (2.1).

Figure 2.3 shows the wavenumber dependence of $S_{\rho\rho}(k)$ in (a) and $\tau_{\rho\rho}(k)$ in (b). We can see that $S_{\rho\rho}(k)$ and $\tau_{\rho\rho}(k)$ are maximized and minimized at almost the same wavenumbers k. For example, both $S_{\rho\rho}(k)$ and $\tau_{\rho\rho}(k)$ have first-peak values around $k = 2\pi$. Thus, there is a correlation between $S_{\rho\rho}(k)$ and $\tau_{\rho\rho}(k)$, i.e., between the static structure and the particle dynamics. A similar correlation was found in the Lennard-Jones (LJ) model [79], water [113], and the polymer model [27]. According to Ref. [27], $\tau_{\rho\rho}(k)$ is modulated by $S_{\rho\rho}(k)$, and this modulation can be understood as a consequence of "de Gennes narrowing" [31].

2.4 Results I: Correlation length, intensity, and lifetime

In this section, we present the results of three quantities: the correlation length $\xi_4(t)$, the intensity $\chi_4(t)$, and the lifetime $\tau_{\rm hetero}(t)$. To define the local dynamics, we consider the two time intervals, τ_α and $\tau_{\rm ngp}$. The value τ_α is the α-relaxation time defined by $F_{s1}(k_m,\tau_\alpha) = e^{-1}$, where $F_{s1}(k,t)$ is the self-part of the density time correlation function for particle species 1 as defined in Eq. (2.6) and $k_m = 2\pi$ is the first-peak wavenumber of the static structure factor. The value $\tau_{\rm ngp}$ is the

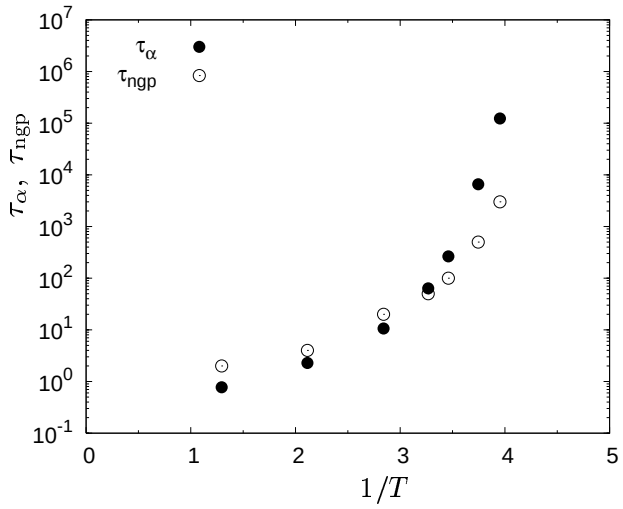

Figure 2.4: Time intervals τ_α and $\tau_{\rm ngp}$ versus the inverse temperature $1/T$. We use these two time intervals to define the local dynamics.

time at which the non-Gaussian parameter $\alpha_2(t)$ [107] of the Van Hove self-correlation function defined as $\alpha_2(t) = 3\langle[\Delta \boldsymbol{r}_1(t)]^4\rangle/5\langle[\Delta \boldsymbol{r}_1(t)]^2\rangle^2 - 1$ is maximized. In Fig. 2.4, we show τ_α and $\tau_{\rm ngp}$ as functions of the inverse temperature $1/T$. At $T = 0.306$, $\tau_\alpha \simeq \tau_{\rm ngp}$, and τ_α grows exponentially larger than $\tau_{\rm ngp}$ with decreasing temperature at $T < 0.306$. This trend agrees with other simulation results for LJ systems [76; 77].

2.4.A Structure of heterogeneous dynamics

We first examined the structure of the heterogeneous dynamics. We calculated the displacement of each particle of species 1 in the time interval $[t_0, t_0 + t]$; $\Delta \boldsymbol{r}_{1j}(t_0, t) = \boldsymbol{r}_{1j}(t_0 + t) - \boldsymbol{r}_{1j}(t_0)$ $(j = 1, 2, ..., N_1)$, and the particle mobility $a^2_{1j}(t_0, t)$ of each particle was defined as

$$a^2_{1j}(t_0, t) = \frac{[\Delta \boldsymbol{r}_{1j}(t_0, t)]^2}{\langle[\Delta \boldsymbol{r}_{1j}(t_0, t)]^2\rangle}. \tag{2.11}$$

In Fig. 2.5, we show the spatial distribution of the particle mobility at $T = 0.772$, 0.306, and 0.253. In the figure, the particles are drawn as spheres with radii $a^2_{1j}(t_0, t)$ located at

$$\boldsymbol{R}_{1j}(t_0, t) = \frac{1}{2}[\boldsymbol{r}_{1j}(t_0) + \boldsymbol{r}_{1j}(t_0 + t)]. \tag{2.12}$$

Notice that $a^2_{1j}(t_0, t) \geq 1$ $(a^2_{1j}(t_0, t) < 1)$ means that the particle j moves more (less) than the mean value of the single-particle displacement, i.e., particle j is mobile (immobile). In Fig. 2.5, the red (blue) spheres represent $a^2_j(t_0, t) \geq 1$ $(a^2_j(t_0, t) < 1)$. We can see that the heterogeneities of both τ_α and $\tau_{\rm ngp}$ increase with decreasing temperature and are significant at $T = 0.253$, the lowest temperature in our simulations. At $T = 0.253$, the two heterogeneities structures in τ_α and $\tau_{\rm ngp}$

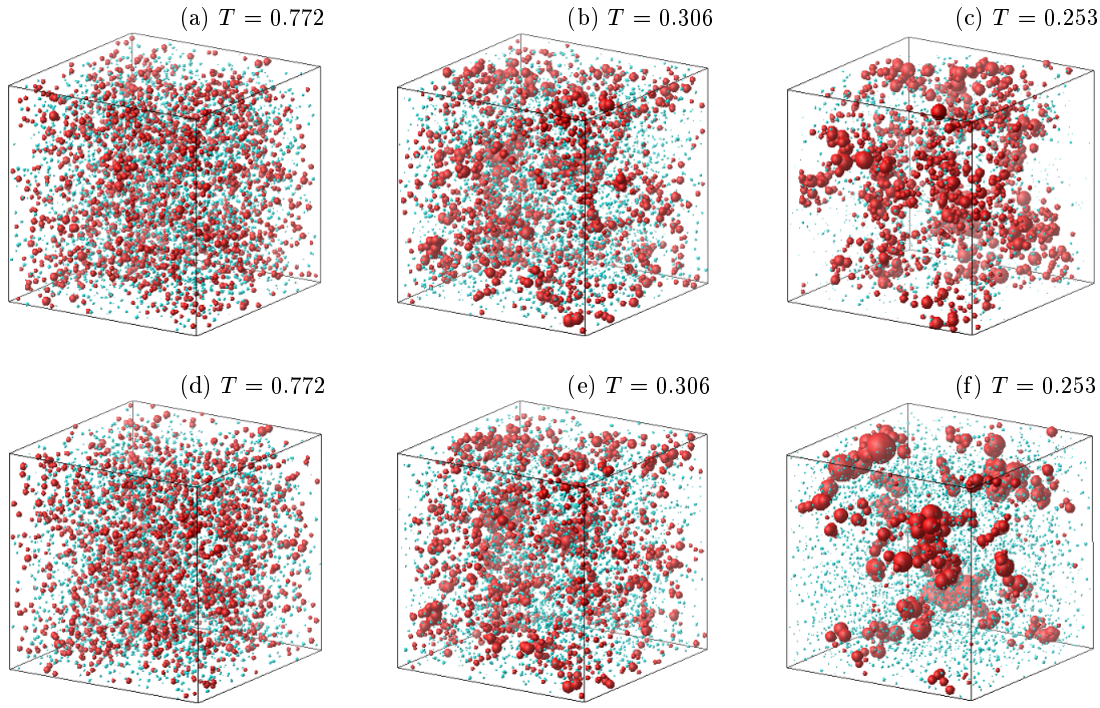

Figure 2.5: The distribution of the particle mobility $a_{1j}^2(t_0, t)$ for particle species 1. The temperatures are 0.772 in (a) and (d), 0.306 in (b) and (e), and 0.253 in (c) and (f). The time intervals are $[t_0, t_0 + \tau_\alpha]$ in (a), (b), and (c), $[t_0, t_0 + \tau_{\rm ngp}]$ in (d), (e), and (f). The radii of the spheres are $[\Delta \boldsymbol{r}_{1j}(t_0, t)]^2 / \langle [\Delta \boldsymbol{r}_{1j}(t_0, t)]^2 \rangle$, and the centers are at $\frac{1}{2}[\boldsymbol{r}_{1j}(t_0) + \boldsymbol{r}_{1j}(t_0 + t)]$. The red and blue spheres represent $[\Delta \boldsymbol{r}_{1j}(t_0, t)]^2 / \langle [\Delta \boldsymbol{r}_{1j}(t_0, t)]^2 \rangle \geq 1$ (mobile particles) and $[\Delta \boldsymbol{r}_{1j}(t_0, t)]^2 / \langle [\Delta \boldsymbol{r}_{1j}(t_0, t)]^2 \rangle < 1$ (immobile particles), respectively.

are both significant but differ considerably. There are many more red spheres in 2.5(c) than in 2.5(f), but there are much larger red spheres in 2.5(f) than in 2.5(c). This pattern means that many mobile particles contribute to the heterogeneity in the time interval τ_α, but in the time interval $\tau_{\rm ngp}$, relatively few particles are mobile and contribute to the heterogeneity.

We also calculated the spatial correlation function of the particle dynamics expressed in Eq. (2.2). We considered the local fluctuations in the particle mobility of particle species 1 defined by

$$\delta \hat{\mathcal{D}}_1(\boldsymbol{r}, t_0, t) = \sum_{j=1}^{N_1} \delta a_{1j}^2(t_0, t) \delta(\boldsymbol{r} - \boldsymbol{R}_{1j}(t_0, t)), \tag{2.13}$$

or the Fourier component $\boldsymbol{q}$ of $\delta \hat{\mathcal{D}}_1(\boldsymbol{r}, t_0, t)$,

$$\delta \mathcal{D}_1(\boldsymbol{q}, t_0, t) = \sum_{j=1}^{N_1} \delta a_{1j}^2(t_0, t) \exp[-i \boldsymbol{q} \cdot \boldsymbol{R}_{1j}(t_0, t)], \tag{2.14}$$

where $\delta a_{1j}^2(t_0, t) = a_{1j}^2(t_0, t) - 1$ is the fluctuation of the particle mobility of the particle j. The order parameter $\delta \mathcal{D}_1(\boldsymbol{q}, t_0, t)$ represents the local fluctuations in the particle dynamics in the time interval $[t_0, t_0 + t]$. We used $\delta \mathcal{D}_1(\boldsymbol{q}, t_0, t)$ as $\delta Q_k(\boldsymbol{q}, t_0, t)$ in Eq. (2.2), and the correlation function

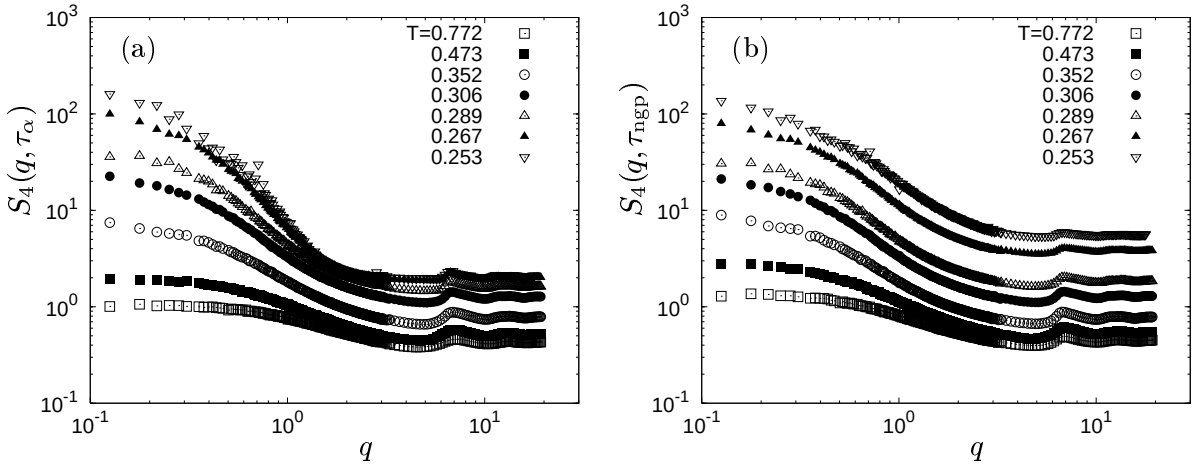

Figure 2.6: The wavenumber dependence of $S_4(q,t)$ for particle species 1 at $T = 0.772 - 0.253$. The time interval t is τ_α in (a) and $\tau_{\rm ngp}$ in (b). Note that $S_4(q,t)$ was calculated with a larger system, $N = 10^5$.

defined by

$$S_4(q,t) = \frac{1}{N_1}\langle \delta\mathcal{D}_1(\boldsymbol{q},0,t)\delta\mathcal{D}_1(-\boldsymbol{q},0,t)\rangle, \tag{2.15}$$

corresponds to $S_{4,k}(q,t)$. The term $S_4(q,t)$ represents the spatial correlation of the particle dynamics in the time interval $[0,t]$. The time configuration of $S_4(q,t)$ is schematically illustrated in Fig. 2.1(a). We were able to examine the structure of the heterogeneous dynamics using the wavenumber dependence of $S_4(q,t)$.

Figure 2.6 shows the wavenumber dependence of $S_4(q,t)$ of particle species 1 for $t = \tau_\alpha$ and $\tau_{\rm ngp}$. We calculated $S_4(q,t)$ using a larger system with $N = 10^5$ to quantify the correlation length and the intensity accurately. At small wavenumbers of q (long-distance scales), the correlations in τ_α and $\tau_{\rm ngp}$ both become large with decreasing temperature in a similar manner. However, at large wavenumbers of q (short-distance scales), $S_4(q,\tau_{\rm ngp})$ grows larger than $S_4(q,\tau_\alpha)$ at low temperatures, which reflects that more highly mobile particles exist in the time interval $\tau_{\rm ngp}$, as can be seen in the visualization shown in Fig. 2.5.

2.4.B Correlation length and intensity of heterogeneous dynamics

We next quantified the correlation length and the intensity of the heterogeneous dynamics in τ_α and $\tau_{\rm ngp}$. As mentioned for Eq. (2.3), at small wavenumbers of q, $S_4(q,t)$ can be approximated by the simple OZ form,

$$S_4(q,t) = \frac{\chi_4(t)}{1 + q^2\xi_4(t)^2}, \tag{2.16}$$

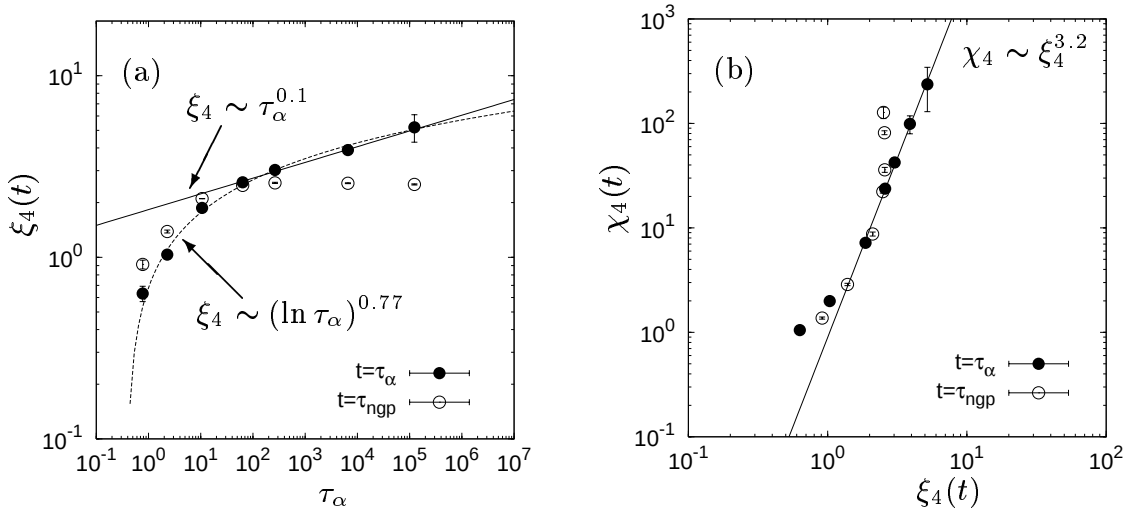

Figure 2.7: (a) The correlation length $\xi_4(t)$ versus τ_α. (b) The intensity $\chi_4(t)$ versus the correlation length $\xi_4(t)$. The time intervals are $t = \tau_\alpha$ and $\tau_{\rm ngp}$. The straight lines are power law fits: $\xi_4(\tau_\alpha) \sim \tau_\alpha^{0.1\pm0.01}$ and $\chi_4(\tau_\alpha) \sim \xi_4(\tau_\alpha)^{3.2\pm0.1}$. The dashed curve is a fit to $\xi_4(\tau_\alpha) \sim (\ln \tau_\alpha)^{0.77\pm0.12}$.

where $\xi_4(t)$ is the correlation length and $\chi_4(t)$ is the intensity. The values $\xi_4(t)$ and $\chi_4(t)$ correspond to $\xi_{4,k}(t)$ and $\chi_{4,k}(t)$ in Eq. (2.3), respectively. To obtain accurate values of $\xi_4(t)$ and $\chi_4(t)$, $S_4(q,t)$ was carefully fitted to the OZ form in the range of $q\xi_4(t) < 1.5$ [41; 42].

Figure 2.7 shows $\xi_4(t)$ versus τ_α in 2.7(a) and $\chi_4(t)$ versus $\xi_4(t)$ in 2.7(b) for $t = \tau_\alpha$ and $\tau_{\rm ngp}$. For the time interval $t = \tau_\alpha$, we examined the scaling relationships between τ_α, $\xi_4(\tau_\alpha)$, and $\chi_4(\tau_\alpha)$. As in Fig. 2.7(a), we obtained a power law fit $\xi_4(\tau_\alpha) \sim \tau_\alpha^{1/z}$ with $1/z = 0.1$. The scaling exponent 0.1 is very small. We also found that a fit to $\xi_4(\tau_\alpha) \sim (\ln \tau_\alpha)^{1/\theta}$ with $1/\theta = 0.77$ provides a better description of the data over a larger range of τ_α, so there is a slower-than-power law increase of $\xi_4(\tau_\alpha)$ with τ_α. Therefore, $\xi_4(\tau_\alpha)$ increases much more slowly compared to τ_α as the temperature decreases. This result is consistent with the most recent results [41; 42]. Furthermore, we obtained the scaling relationship $\chi_4(\tau_\alpha) \sim \xi_4(\tau_\alpha)^{2-\eta}$ with $2 - \eta = 3.2$ in Fig. 2.7(b). Our scaling exponent 3.2 agrees well with Ref. [41; 42].

On the other hand, when the time interval t is $\tau_{\rm ngp}$, $\xi_4(\tau_{\rm ngp})$ reaches a value near $\tau_\alpha \simeq 250$ and then plateaus as τ_α increases in Fig. 2.7(a), while $\chi_4(\tau_{\rm ngp})$ monotonically gets large in Fig. 2.7(b). Here, we remark that even in the range where $\xi_4(\tau_{\rm ngp})$ plateaus, $\chi_4(\tau_{\rm ngp})$ continues to increase with τ_α. This behavior of $\xi_4(\tau_{\rm ngp})$ and $\chi_4(\tau_{\rm ngp})$ may be due to the choice of the order parameter $\delta\hat{\mathcal{D}}_1(\boldsymbol{r}, t_0, t)$. $\delta\hat{\mathcal{D}}_1(\boldsymbol{r}, t_0, t)$ represents the distribution of the square particle displacements, so the mobile particles with large displacements contribute to the structure factor $S_4(q,t)$ much more than the immobile particles. At $t = \tau_{\rm ngp}$ and at low temperatures, our simulation data show that only

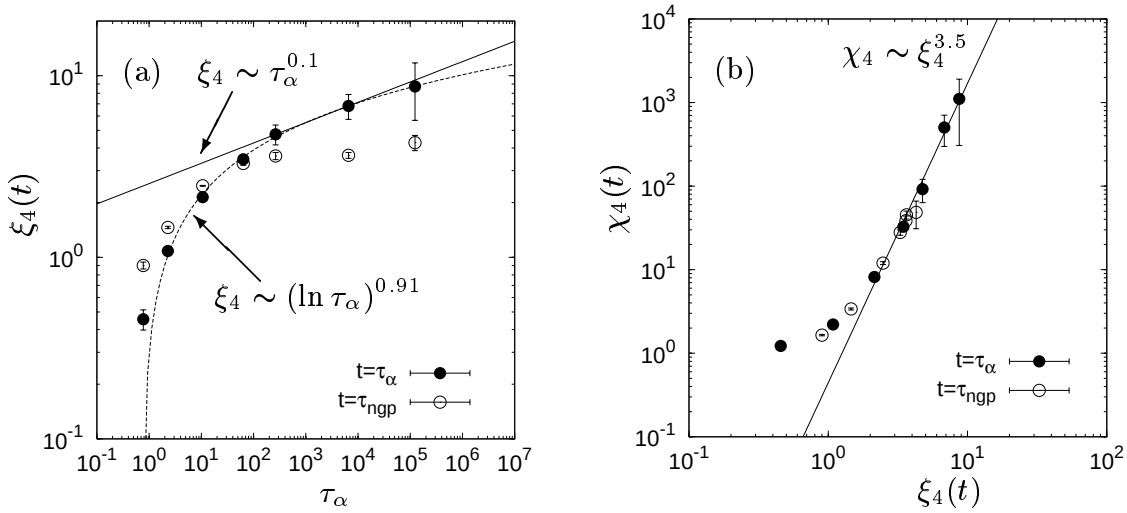

Figure 2.8: The correlation length $\xi_4(t)$ and the intensity $\chi_4(t)$ calculated by using $\delta\hat{\mathcal{D}}_{\log 1}(\boldsymbol{r}, t_0, t)$, i.e., the distribution of the logarithm of the square particle displacements. (a) $\xi_4(t)$ versus τ_α. (b) $\chi_4(t)$ versus $\xi_4(t)$. The time intervals are $t = \tau_\alpha$ and $\tau_{\rm ngp}$. The straight lines are power law fits: $\xi_4(\tau_\alpha) \sim \tau_\alpha^{0.1\pm0.01}$ and $\chi_4(\tau_\alpha) \sim \xi_4(\tau_\alpha)^{3.5\pm0.2}$. The dashed curve is a fit to $\xi_4(\tau_\alpha) \sim (\ln \tau_\alpha)^{0.91\pm0.12}$.

a small number of particles tend to have very large displacements compared to the other mostly immobile particles, which can be also seen in Fig. 2.5. In this situation, the intensity $\chi_4(\tau_{\rm ngp})$ can increase from the contribution of particles with very large displacements, whereas the correlation length $\xi_4(\tau_{\rm ngp})$ cannot increase because the number of mobile particles involved in the correlated regions decreases.

So, we used an another order parameter $\delta\hat{\mathcal{D}}_{\log 1}(\boldsymbol{r}, t_0, t)$ defined as

$$\delta\hat{\mathcal{D}}_{\log 1}(\boldsymbol{r}, t_0, t) = \sum_{j=1}^{N_1} \ln a_{1j}^2(t_0, t)\delta(\boldsymbol{r} - \boldsymbol{R}_{1j}(t_0, t)). \tag{2.17}$$

The order parameter $\delta\hat{\mathcal{D}}_{\log 1}(\boldsymbol{r}, t_0, t)$ represents the distribution of the logarithm of the square particle displacements. We quantified $\xi_4(t)$ and $\chi_4(t)$ in terms of the structure factor of $\delta\hat{\mathcal{D}}_{\log 1}(\boldsymbol{r}, t_0, t)$. Notice that in this case, the immobile particles with small displacements contribute to the structure factor to the same extent as the mobile particles because of the logarithm operation. Figure 2.8 shows $\xi_4(t)$ and $\chi_4(t)$ calculated by $\delta\hat{\mathcal{D}}_{\log 1}(\boldsymbol{r}, t_0, t)$. At the time interval $t = \tau_\alpha$, the scaling relationships between τ_α, $\xi_4(\tau_\alpha)$ and $\chi_4(\tau_\alpha)$ are almost same as those examined by $\delta\hat{\mathcal{D}}_1(\boldsymbol{r}, t_0, t)$. On the other hand, at the time interval $t = \tau_{\rm ngp}$, both $\xi_4(\tau_{\rm ngp})$ and $\chi_4(\tau_{\rm ngp})$ reach values near $\tau_\alpha \simeq 250$ and then plateau as τ_α increases, i.e., both $\xi_4(\tau_{\rm ngp})$ and $\chi_4(\tau_{\rm ngp})$ show the plateau of the heterogeneity. This result indicates that the behavior that $\chi_4(\tau_{\rm ngp})$ continues to increase in Fig. 2.7(a) is due to the choice of the order parameter $\delta\hat{\mathcal{D}}_1(\boldsymbol{r}, t_0, t)$.

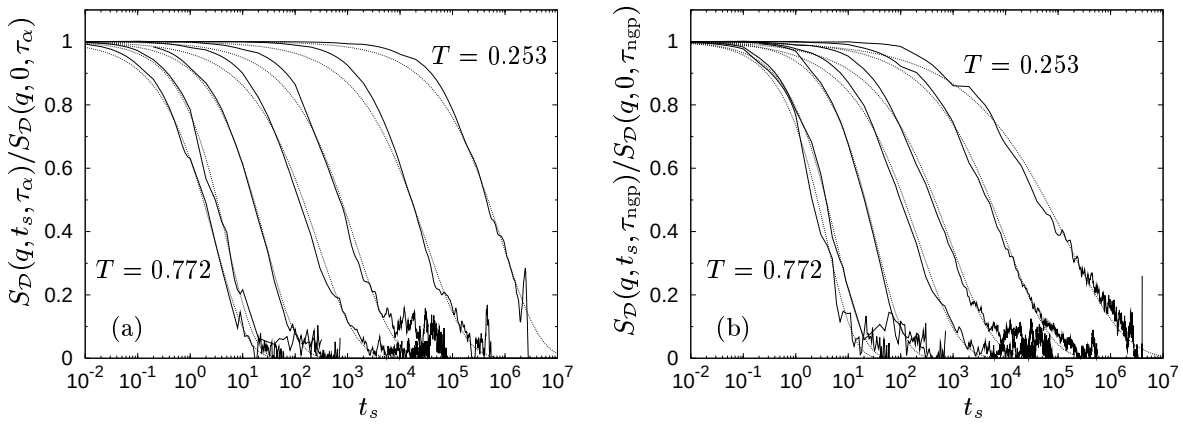

Figure 2.9: The time decay of $S_{\mathcal{D}}(q,t_s,t)$ of particle species 1 at $q = 0.38$ for $T = 0.772 - 0.253$. The time interval t is τ_α in (a) and $\tau_{\rm ngp}$ in (b). The temperature decreases going right. The dotted lines are the stretched exponential functions fitted for $S_{\mathcal{D}}(q,t_s,t)$.

2.4.C Motion of heterogeneous dynamics

Next, we investigated the motion of the heterogeneous dynamics at the time intervals $t = \tau_\alpha$ and $\tau_{\rm ngp}$ by the time correlation function of the particle dynamics expressed in Eq. (2.4). We used $\delta\mathcal{D}_1(\boldsymbol{q},t_0,t)$ as $\delta Q_k(\boldsymbol{q},t_0,t)$ in Eq. (2.4), and the correlation function $S_{\mathcal{D}}(q,t_s,t)$,

$$S_{\mathcal{D}}(q,t_s,t) = \langle \delta\mathcal{D}_1(\boldsymbol{q},t_s+t,t)\delta\mathcal{D}_1(-\boldsymbol{q},0,t)\rangle, \tag{2.18}$$

corresponds to $F_{4,k}(q,t_s,t)$ and represents the correlation of the particle dynamics between two time intervals $[0,t]$ and $[t_s+t,t_s+2t]$. The time configuration of $S_{\mathcal{D}}(q,t_s,t)$ is schematically illustrated in Fig. 2.1(b). As mentioned for Eq. (2.5), when the time separation t_s increases, $S_{\mathcal{D}}(q,t_s,t)$ with fixed t decays in the stretched exponential form,

$$\frac{S_{\mathcal{D}}(q,t_s,t)}{S_{\mathcal{D}}(q,0,t)} \sim \exp\left(-\left(\frac{t_s}{\tau_h(q,t)}\right)^c\right), \tag{2.19}$$

where $\tau_h(q,t)$ is the wavenumber-dependent relaxation time of $S_{\mathcal{D}}(q,t_s,t)$ and represents the time scale at which the heterogeneous dynamics move in the space. The expression $\tau_h(q,t)$ corresponds to $\tau_{4,k}(q,t)$ in Eq. (2.5). We were able to examine the motion of the heterogeneous dynamics using the wavenumber dependence of $\tau_h(q,t)$.

Figure 2.9 shows the time decay of $S_{\mathcal{D}}(q,t_s,t)$ of particle species 1 for $t = \tau_\alpha$ and $\tau_{\rm ngp}$ at $q = 0.38$. We can see that $S_{\mathcal{D}}(q,t_s,t)$ decays in the stretched exponential form. In Fig. 2.10, we show the wavenumber dependence of $\tau_h(q,t)$ for $t = \tau_\alpha$ and $\tau_{\rm ngp}$. Both $\tau_h(q,\tau_\alpha)$ and $\tau_h(q,\tau_{\rm ngp})$ dramatically increase with decreasing temperature in a wide region of wave numbers, $q = 0.38 - 19$.

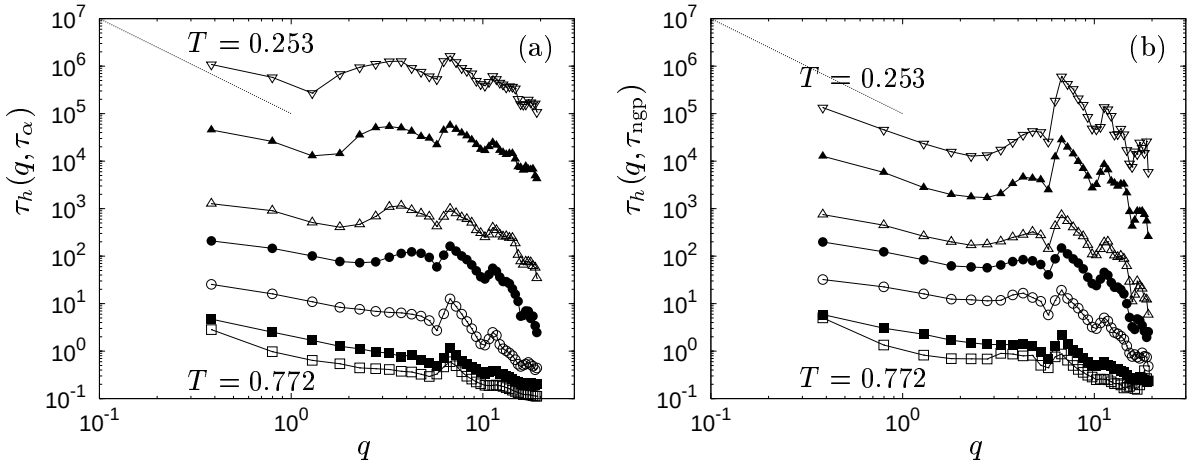

Figure 2.10: The wavenumber dependence of $\tau_h(q,t)$ for $T = 0.772 - 0.253$. The time interval t is τ_α in (a) and $\tau_{\rm ngp}$ in (b). The temperature decreases going up. The dotted line is $\tau_h(q,t) \sim q^{-2}$.

Comparing Fig. 2.10 with Fig. 2.2, $\tau_h(q,t)$ depends on q more weakly than the wavenumber-dependent relaxation time of the two-point density correlation functions and dramatically increases with decreasing temperature in a wide region of q ($q = 0.38 - 19$). Furthermore, it can be seen that $\tau_h(q,t)$ approaches $\tau_h(q,\tau_\alpha) \sim q^{-a} (0 < a \leq 2)$ at small q. This suggests that the heterogeneous dynamics may migrate in space with a diffusion-like mechanism.

2.4.D Lifetime of heterogeneous dynamics

We determined the lifetime $\tau_{\rm hetero}(t)$ of the heterogeneous dynamics as $\tau_h(q,t)$ at $q = 0.38$, which is the time separation t_s at which $S_{\mathcal{D}}(q,t_s,t)/S_{\mathcal{D}}(q,0,t)$ at $q = 0.38$ equals e^{-1} in Fig.2.9. The value $\tau_{\rm hetero}(t)$ increases dramatically with decreasing temperature. We plot $\tau_{\rm hetero}(t)$ versus τ_α in Fig.2.11, which shows that $\tau_{\rm hetero}(\tau_\alpha) \sim \tau_\alpha^{1.08\pm0.02}$ and $\tau_{\rm hetero}(\tau_{\rm ngp}) \sim \tau_\alpha^{0.91\pm0.03}$. The difference between $\tau_{\rm hetero}(\tau_\alpha)$ and $\tau_{\rm hetero}(\tau_{\rm ngp})$ increases with decreasing temperature. At $T = 0.253$, $\tau_{\rm hetero}(\tau_\alpha) \simeq 7.8\tau_\alpha$, and $\tau_{\rm hetero}(\tau_{\rm ngp}) \simeq 1.4\tau_\alpha$. Therefore, $\tau_{\rm hetero}(\tau_\alpha)$ is considerably larger than τ_α, while $\tau_{\rm hetero}(\tau_{\rm ngp})$ is comparable to τ_α. The existence of a slower timescale in the heterogeneous dynamics is consistent with Refs. [72] [73]. In Sec. 2.4.B, we used the order parameter $\delta\hat{\mathcal{D}}_{\log 1}(\boldsymbol{r},t_0,t)$. So, for the confirmation purpose, we also calculated the lifetime $\tau_{\rm hetero}(t)$ by using $\delta\hat{\mathcal{D}}_{\log 1}(\boldsymbol{r},t_0,t)$ and checked that the lifetimes of both $\delta\hat{\mathcal{D}}_1(\boldsymbol{r},t_0,t)$ and $\delta\hat{\mathcal{D}}_{\log 1}(\boldsymbol{r},t_0,t)$ have almost same values and behave in the same manner with decreasing temperature.

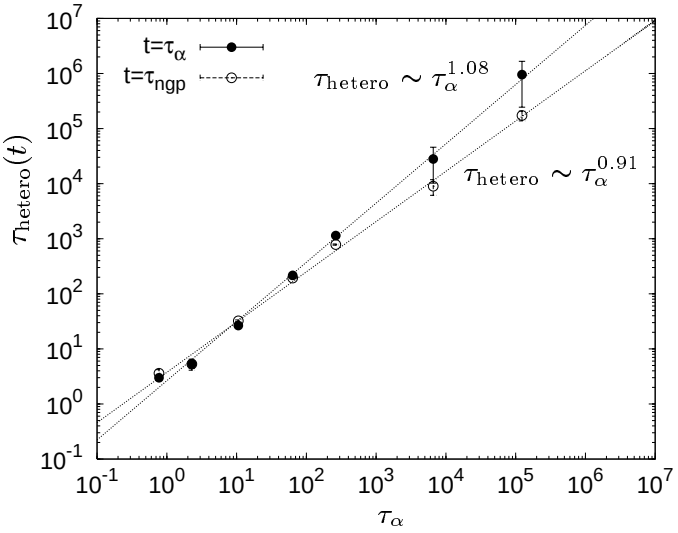

Figure 2.11: The lifetime $\tau_{\rm hetero}(t)$ for $t = \tau_\alpha$, $\tau_{\rm ngp}$ versus τ_α. The error bars represent the standard deviations of averaging data over initial times. The line $\tau_{\rm hetero} \sim \tau_\alpha^{1.08\pm0.02}$ is fitted for $t = \tau_\alpha$, while the line $\tau_{\rm hetero} \sim \tau_\alpha^{0.91\pm0.03}$ is fitted for $t = \tau_{\rm ngp}$.

2.4.E Scaling relationships between correlation length, intensity, and lifetime

Finally, we determined the scaling relationships between the correlation length, the intensity, and the lifetime. At the time interval $t = \tau_\alpha$, the following scaling relationship between the correlation length and the lifetime holds:

$$\tau_{\rm hetero}(\tau_\alpha) \sim \xi_4(\tau_\alpha)^{10.8}, \tag{2.20}$$

or

$$\tau_{\rm hetero}(\tau_\alpha) \sim \exp(k\xi_4(\tau_\alpha)^{1.3}). \tag{2.21}$$

The scaling exponent 10.8 of the power law scaling is very large, and there is an exponential growth of $\tau_{\rm hetero}(\tau_\alpha)$ with $\xi_4(\tau_\alpha)$. Furthermore, at the time interval $t = \tau_{\rm ngp}$, although the correlation length $\xi_4(\tau_{\rm ngp})$ plateaus, the lifetime $\tau_{\rm hetero}(\tau_{\rm ngp})$ continues to increase dramatically with decreasing temperature. Thus, we can conclude that the lifetime $\tau_{\rm hetero}$ gets large dramatically with decreasing temperature, whereas the correlation length ξ_4 and the intensity χ_4 increase slowly compared to $\tau_{\rm hetero}$ or plateau, i.e., the time scale of dynamical heterogeneity grows faster than the length scale and the intensity of dynamical heterogeneity.

2.5 Results II: Time-interval dependence of lifetime

In this section, we present the results for the time-interval dependence of the lifetime $\tau_{\rm hetero}(t)$. To examine the lifetime in more detail, we evaluated the lifetime $\tau_{\rm hetero}(t)$ for various time intervals t

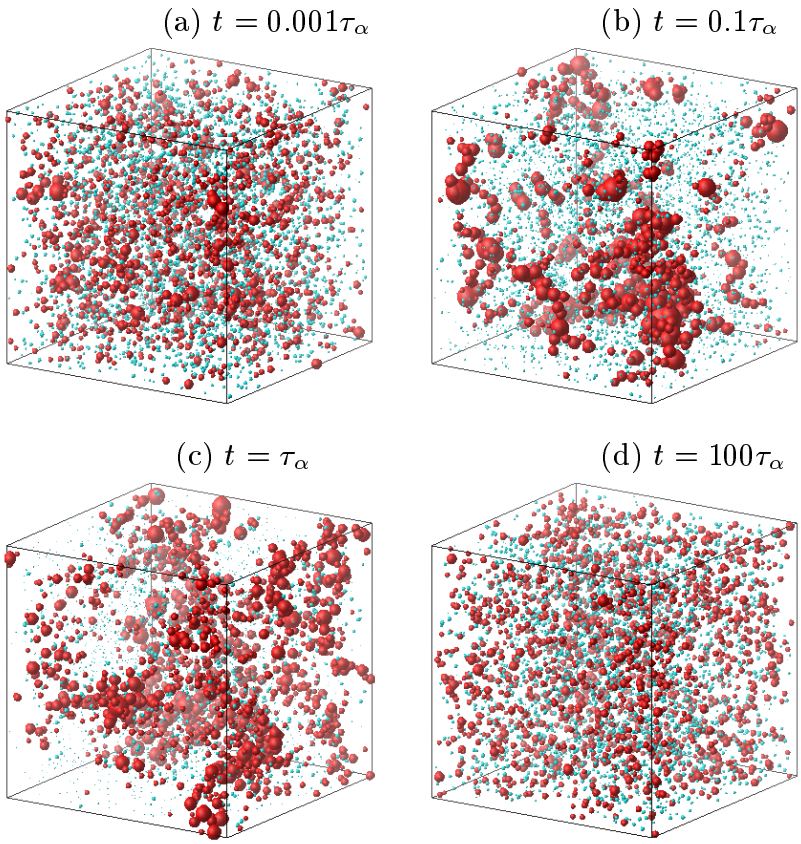

Figure 2.12: The time-interval dependence of the distribution of the particle mobility $a_{1j}^2(t_0, t)$ for particle species 1. The time intervals are (a) $t = 0.001\tau_\alpha$, (b) $t = 0.1\tau_\alpha$, (c) $t = \tau_\alpha$, and (d) $t = 100\tau_\alpha$. The temperature is 0.267. The radii of the spheres are $a_{1j}^2(t_0, t)$, and the centers are at $\boldsymbol{R}_{1j}(t_0, t)$. See also the caption for Fig. 2.5.

and determine how the lifetime $\tau_{\text{hetero}}(t)$ depends on the time interval.

2.5.A Structure of heterogeneous dynamics

First, we examined the time-interval dependence of the structure of the heterogeneous dynamics. The spatial distribution of the particle mobility $a_{1j}^2(t_0, t)$ for particle species 1 is shown in Fig. 2.12, in which the time interval increases from $t = 0.001\tau_\alpha$ to $100\tau_\alpha$. The temperature is 0.267. We can recognize that the heterogeneity is much weaker at the short time interval $t = 0.001\tau_\alpha$ in 2.12(a). As the time interval t increases, the heterogeneity increases and is maximized between $t = 0.1\tau_\alpha$ in 2.12(b) and $t = \tau_\alpha$ in 2.12(c). As the time interval t increases further, the heterogeneity decreases and is weakened at $t = 100\tau_\alpha$ in 2.12(d).

We also calculated the spatial correlation function $S_4(q, t)$ defined in Eq. (2.15). Figure 2.13 shows the wavenumber dependence of $S_4(q, t)$ for various time intervals t. We can see that as the time interval t gets large, $S_4(q, t)$ increases, is maximized, and then decreases in the region of q.

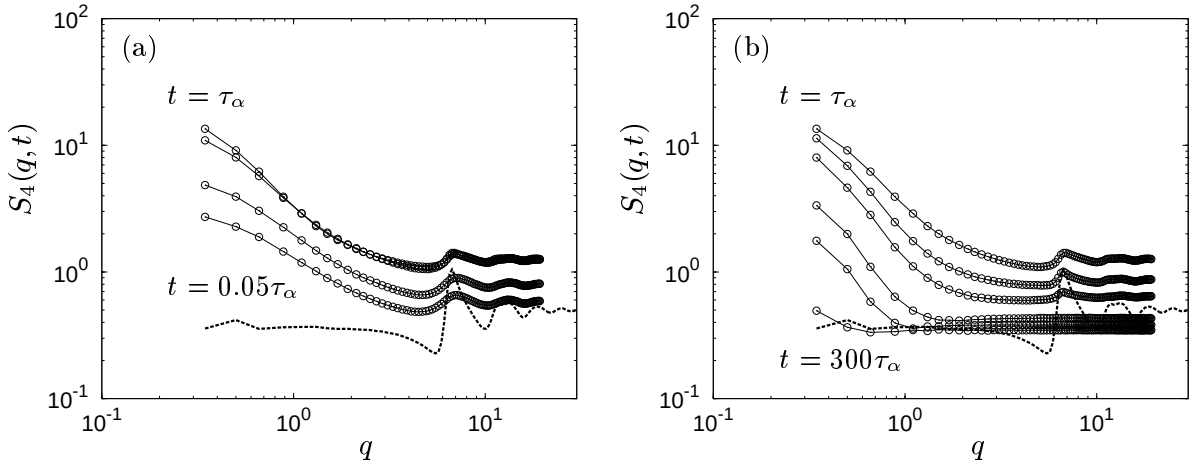

Figure 2.13: The wavenumber dependence of $S_4(q,t)$ at $T = 0.306$. The time intervals are (a) $0.05\tau_\alpha$, $0.1\tau_\alpha$, $0.5\tau_\alpha$, and τ_α from the lowest curve to the highest, and (b) τ_α, $5\tau_\alpha$, $10\tau_\alpha$, $50\tau_\alpha$, $100\tau_\alpha$, and $300\tau_\alpha$ from the highest curve to the lowest. $S_4(q,t)$ is maximized at $t = \tau_\alpha$. The dashed curve represents the static structure factor $S_{11}(q)$.

This behavior agrees with the visualization of the heterogeneity structure shown in Fig. 2.12. It is also seen that at large time intervals, $S_4(q,t)$ maintains a constant value, independent of the wavenumber q. This result indicates that at large time intervals, particle mobilities are uniformly distributed throughout space, i.e., the structure of the particle dynamics is spatially homogeneous. Note that the static structure factor $S_{11}(q)$ also becomes constant at small q (long-distance scale).

2.5.B Motion of heterogeneous dynamics

Next, the motion of heterogeneous dynamics was investigated in detail. In Sec. 2.4.C, we investigated the motion of the heterogeneous dynamics at the time intervals $t = \tau_\alpha$ and $\tau_{\rm ngp}$. Our results suggested that the heterogeneous dynamics might migrate in space with a diffusion-like mechanism. In this section, we examined the motion of the heterogeneous dynamics at various time intervals t. As in Sec. 2.4.C, we calculated the time correlation function $S_{\mathcal{D}}(q,t_s,t)$ defined in Eq. (2.18) and the wavenumber-dependent relaxation time $\tau_h(q,t)$.

In Fig. 2.14, we show the wavenumber dependence of $\tau_h(q,t)$ for various time intervals t. As the time interval t increases, at small wavenumbers q, $\tau_h(q,t)$ increases monotonically and approaches the relaxation time $\tau_{c1}(q)$ of the two-point density correlation function shown in Fig. 2.2. This result indicates that the heterogeneous dynamics at large time intervals behave like the particle density, the motion of which is diffusive at a long distance scale. Notice that $\tau_h(q,t)$ at large t and small q is proportional to q^{-2}, which indicates this diffusion mechanism. We also checked that

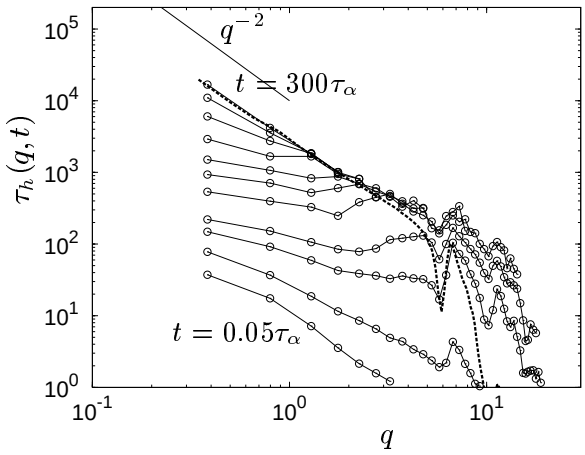

Figure 2.14: The wavenumber dependence of $\tau_h(q,t)$ at $T = 0.306$. The time intervals are $0.05\tau_\alpha$, $0.1\tau_\alpha$, $0.5\tau_\alpha$, τ_α, $5\tau_\alpha$, $10\tau_\alpha$, $30\tau_\alpha$, $50\tau_\alpha$, $70\tau_\alpha$, $100\tau_\alpha$, and $300\tau_\alpha$ from the lowest curve to the highest. The dashed curve is the relaxation time $\tau_{c1}(q)$ of the two-point density correlation function.

$S_{\mathcal{D}}(q,t_s,t)$ decays in the exponential form at large t and small q, as does the two-point density correlation function.

Furthermore, we calculated the self-part of $S_{\mathcal{D}}(q,t_s,t)$, defined by:

$$S_{\mathcal{D}s}(q,t_s,t) = \left\langle \frac{1}{N_1}\sum_{j=1}^{N_1} \delta\mathcal{D}_{1j}(\boldsymbol{q},t_s+t,t)\delta\mathcal{D}_{1j}(\boldsymbol{q},0,t) \right\rangle, \tag{2.22}$$

where

$$\delta\mathcal{D}_{1j}(\boldsymbol{q},t_0,t) = \delta a_{1j}^2(t_0,t)\exp[-i\boldsymbol{q}\cdot\boldsymbol{R}_{1j}(t_0,t)]. \tag{2.23}$$

The correlation function $S_{\mathcal{D}s}(q,t_s,t)$ represents the correlation of the individual particle dynamics between two time intervals $[0,t]$ and $[t_s+t, t_s+2t]$. Like $S_{\mathcal{D}}(q,t_s,t)$, as the time separation t_s increases, $S_{\mathcal{D}s}(q,t_s,t)$ decays in the stretched exponential form with the relaxation time $\tau_{hs}(q,t)$. The value of $\tau_{hs}(q,t)$ is the time scale at which the individual heterogeneous dynamics move in space. Figure 2.15 shows the wavenumber dependence of $\tau_{hs}(q,t)$ for various time intervals t. As the time interval t increases, $\tau_{hs}(q,t)$ increases monotonically at small q and approaches the relaxation time $\tau_{s1}(q)$ of the self-part of the two-point density correlation function shown in Fig. 2.2. Like $\tau_h(q,t)$, $\tau_{hs}(q,t)$ is also proportional to q^{-2} at large t and small q. Thus, both the collective-particle behavior and the single-particle behavior of the heterogeneous dynamics at large time intervals are diffusive, like the motion of particle density at long-distance scales.

That $\tau_h(q,t)$ and $\tau_{hs}(q,t)$ approach the relaxation times $\tau_{c1}(q)$ and $\tau_{s1}(q)$ of the two-point density correlation functions can possibly be interpreted as follows. The correlation function $S_{\mathcal{D}}(q,t_s,t)$

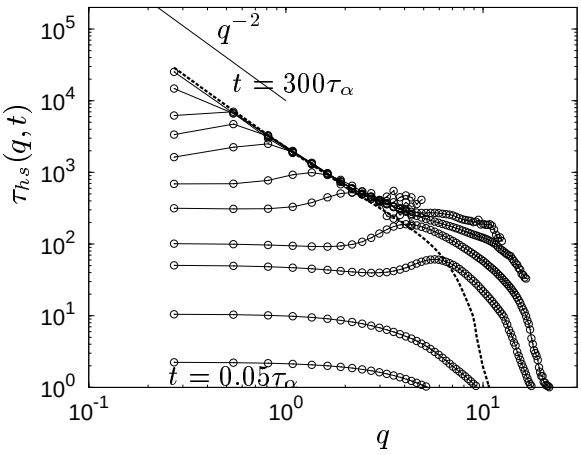

Figure 2.15: The wavenumber dependence of $\tau_{hs}(q,t)$ at $T = 0.306$. The time intervals are $0.05\tau_\alpha$, $0.1\tau_\alpha$, $0.5\tau_\alpha$, τ_α, $5\tau_\alpha$, $10\tau_\alpha$, $30\tau_\alpha$, $50\tau_\alpha$, $70\tau_\alpha$, $100\tau_\alpha$, and $300\tau_\alpha$ from the lowest curve to the highest. The dashed curve is the relaxation time $\tau_{s1}(q)$ of the self-part of the two-point density correlation function.

can be written as

$$S_{\mathcal{D}}(q,t_s,t) = \left\langle \sum_{j=1}^{N_1}\sum_{k=1}^{N_1} \delta a_{1j}^2(t_s+t,t)\delta a_{1k}^2(0,t) \exp[-i\boldsymbol{q}\cdot(\boldsymbol{R}_{1j}(t_s+t,t) - \boldsymbol{R}_{1k}(0,t))] \right\rangle. \tag{2.24}$$

From this expression, there can be two types of relaxation of $S_{\mathcal{D}}(q,t_s,t)$ with increasing time of separation t_s. One is the relaxation due to fluctuations in the particle mobility, i.e., due to the term "$\delta a_{1j}^2(t_s+t,t)\delta a_{1k}^2(0,t)$". The other is the relaxation due to particle motion, i.e., due to the term "$\exp[-i\boldsymbol{q}\cdot(\boldsymbol{R}_{1j}(t_s+t,t) - \boldsymbol{R}_{1k}(0,t))]$", which is the same as the relaxation of the density correlation functions. So, the total relaxation time $\tau_h(q,t)$ of $S_{\mathcal{D}}(q,t_s,t)$ is determined by the two times $\tau_{\delta a}(t)$ and $\tau_{c1}(q)$, where $\tau_{\delta a}(t)$ is the time scale at which particle mobility fluctuates, and $\tau_{c1}(q)$ is the time scale of particle motion and is the relaxation time of the density correlation function. Here, for simplicity, we assume that $S_{\mathcal{D}}(q,t_s,t)$ relaxes with these two times $\tau_{\delta a}(t)$ and $\tau_{c1}(q)$ in the form

$$\frac{S_{\mathcal{D}}(q,t_s,t)}{S_{\mathcal{D}}(q,0,t)} \sim \exp\left(-\left(\frac{t_s}{\tau_{\delta a}(t)}\right)^c\right) \times \exp\left(-\left(\frac{t_s}{\tau_{c1}(q)}\right)^c\right). \tag{2.25}$$

The relaxation time $\tau_h(q,t)$ is then mainly determined by the smaller time scale of $\tau_{\delta a}(t)$ and $\tau_{c1}(q)$. When the time interval t is small, particle mobilities fluctuate faster than the particles move, which means that $\tau_{\delta a}(t)$ is smaller than $\tau_{c1}(q)$. In this case, $\tau_h(q,t)$ is determined by the time $\tau_{\delta a}(t)$. As the time interval t increases, then the fluctuations in particle mobilities becomes slower, and the lifetime $\tau_h(q,t)$ increases accordingly. As the time interval t increases further, particle mobilities fluctuate more slowly than the particles move, which means that $\tau_{\delta a}(t)$ becomes larger than $\tau_{c1}(q)$. In this case, $\tau_h(q,t)$ is determined by the time $\tau_{c1}(q)$ instead of $\tau_{\delta a}(t)$. Thus, at large time intervals,

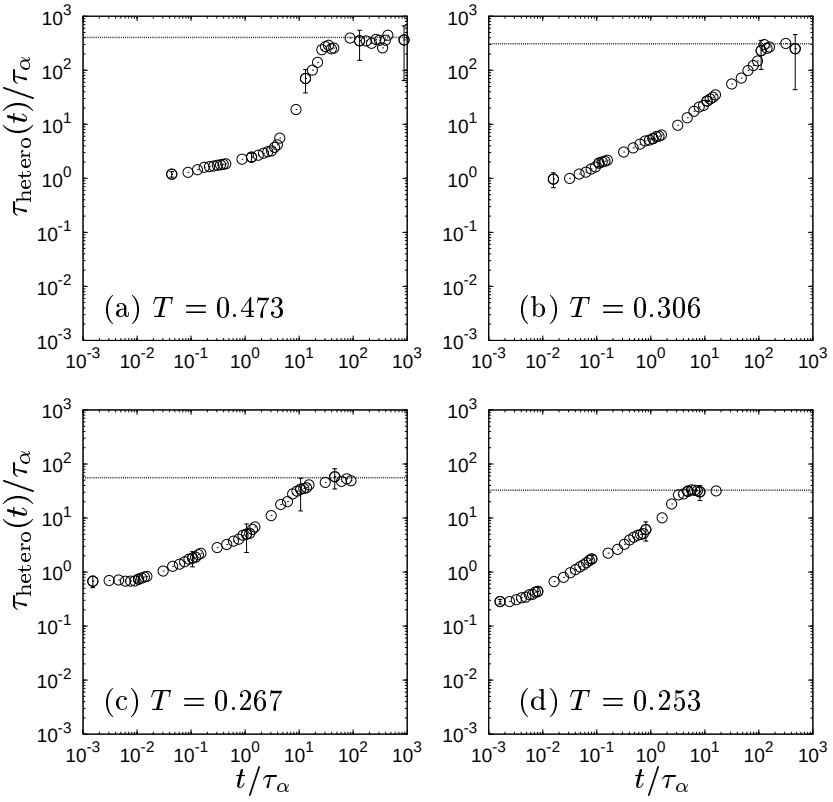

Figure 2.16: The time-interval dependence of $\tau_{\rm hetero}(t)$. Temperatures are 0.473 in (a), 0.306 in (b), 0.267 in (c), and 0.253 in (d). The time interval t and the lifetime $\tau_{\rm hetero}(t)$ are normalized by τ_α. The dotted line indicates the value of $\tau_{c1}(q)$ at $q = 0.38$, where $\tau_{c1}(q)$ is the relaxation time of the two-point density correlation function.

because particle mobilities fluctuate very slowly, the relaxation time $\tau_h(q,t)$ can be determined by the time scale of particle motions, which is the relaxation time of the density correlation function.

2.5.C Lifetime of heterogeneous dynamics

Finally, we determined the lifetime $\tau_{\rm hetero}(t)$ of the heterogeneous dynamics as $\tau_h(q,t)$ at $q = 0.38$. We show the time-interval dependence of the lifetime $\tau_{\rm hetero}(t)$ for various temperatures in Fig. 2.16. As the time interval t increases, $\tau_{\rm hetero}(t)$ increases monotonically, and at large time intervals, $\tau_{\rm hetero}(t)$ approaches and is limited to the relaxation time $\tau_{c1}(q = 0.38)$ of the two-point density correlation function. At large time intervals for which $\tau_{\rm hetero}(t)$ plateaus, the heterogeneous dynamics migrate in space with a diffusion mechanism like that of particle density, as we showed in Figs. (2.14) and (2.15).

2.6 Conclusion

In this study, we have investigated three quantities that characterize dynamical heterogeneity: the correlation length $\xi_4(t)$, the intensity $\chi_4(t)$, and the lifetime $\tau_{\rm hetero}(t)$. The intensity $\chi_4(t)$ measures the average variance of the slow and fast regions, and the correlation length $\xi_4(t)$ characterizes the spatial extent of the slow and fast regions. The lifetime $\tau_{\rm hetero}(t)$ represents the time scale at which the slow and fast regions migrate in space. We evaluated all three quantities using a single order parameter representing the particle dynamics and its correlation functions. To define the particle dynamics, we used two time intervals, $t = \tau_\alpha$ and $\tau_{\rm ngp}$. We found that at low temperatures, the lifetime $\tau_{\rm hetero}(t)$ increases dramatically with decreasing temperature. In contrast, the correlation length $\xi_4(t)$ and the intensity $\chi_4(t)$ increase slowly compared to the lifetime or plateau. At the time interval $t = \tau_\alpha$, we obtained the scaling relationships between $\xi_4(t)$, $\chi_4(t)$, and $\tau_{\rm hetero}(\tau_\alpha)$: $\chi_4(\tau_\alpha) \sim \xi_4(\tau_\alpha)^{3.2}$ and $\tau_{\rm hetero}(\tau_\alpha) \sim \xi_4(\tau_\alpha)^{10.8}$ or $\tau_{\rm hetero}(\tau_\alpha) \sim \exp(k\xi_4(\tau_\alpha)^{1.3})$. The scaling exponent 10.8 of $\tau_{\rm hetero}(\tau_\alpha) \sim \xi_4(\tau_\alpha)^{10.8}$ is very large, and there is an exponential growth of $\tau_{\rm hetero}(\tau_\alpha)$ with $\xi_4(\tau_\alpha)$. Furthermore, at the time interval $t = \tau_{\rm ngp}$, although the correlation length $\xi_4(\tau_{\rm ngp})$ plateaus as the temperature decreases, the lifetime $\tau_{\rm hetero}(\tau_{\rm ngp})$ continues to increase dramatically. Thus, we can conclude that the lifetime $\tau_{\rm hetero}$ gets large dramatically with decreasing temperature, whereas the correlation length ξ_4 and the intensity χ_4 increase slowly compared to $\tau_{\rm hetero}$ or plateau, i.e., the time scale of dynamical heterogeneity grows faster than the length scale and the intensity of dynamical heterogeneity.

Furthermore, we investigated the time-interval dependence of the lifetime $\tau_{\rm hetero}(t)$. As the time interval t increases, $\tau_{\rm hetero}(t)$ increases monotonically. At large time intervals, the lifetime $\tau_{\rm hetero}(t)$ approaches and is limited to the relaxation time of the two-point density correlation function. At those large time intervals, the wavenumber-dependent lifetimes $\tau_h(q,t)$ at small wavenumbers q (long-distance scales) almost coincide with the relaxation time $\tau_{c1}(q)$ of the two-point density correlation function and are proportional to q^{-2}. Therefore, the heterogeneous dynamics migrate in space with a diffusion mechanism like that of particle density. Note that at large time intervals, particle mobilities $a_{1j}^2(t_0,t)$ are uniformly distributed in space, and the heterogeneity structure is much weaker.

Chapter 3

Dynamical heterogeneity in a supercooled liquid under sheared condition

3.1 Introduction

When liquids are cooled toward the glass transition temperature T_g, the dynamics not only drastically slow down, but also become progressively more heterogeneous [34; 35; 65; 71; 87; 96; 104; 127; 128]. "Dynamical heterogeneity" has attracted much attention because it may lead to a better understanding of slow dynamics [16; 36]. Dynamical heterogeneity is characterized by three quantities: the correlation length ξ_4, the intensity χ_4, and the lifetime τ_{hetero} [12; 25; 33; 40; 41; 42; 49; 69; 72; 73; 80; 81; 91; 92; 117; 119]. The correlation length ξ_4 and the intensity χ_4 characterize the static properties of the dynamical heterogeneity and can be quantified by means of the static structure factor of the particle dynamics, i.e., the so-called four-point correlation function [12; 25; 33; 41; 42; 49; 69; 80; 117; 119]. The lifetime τ_{hetero} measures the dynamical properties of the dynamical heterogeneity, and we can evaluate the lifetime by the time decay of the correlation function of the particle dynamics [40; 72; 73; 81]. In our previous studies [91; 92] (Chapter 2), we have consistently quantified these three quantities (correlation length, intensity, and lifetime) from a single order parameter and its correlation functions. The length scale and the time scale of the dynamical heterogeneity tend to diverge as the temperature approaches the glass transition point.

Dynamical heterogeneity has also been investigated for a sheared situation [57; 58; 98; 120; 131]. When applying a steady shear flow to supercooled liquids, marked shear-thinning can be observed [17; 90; 122]. In the sheared situation, the dynamics become not only much faster but also more homogeneous; therefore, the shear flow suppresses the dynamical heterogeneity. Refs. [58; 98; 120] found that the intensity χ_4 of the dynamical heterogeneity decreases with an increasing shear rate $\dot{\gamma}$ as $\chi_4 \sim \dot{\gamma}^{-\mu}$ with $\mu = 0.3$ [98; 120] or $\mu = 0.4 - 0.6$ [58]. To the best of our knowledge, the lifetime τ_{hetero} of the dynamical heterogeneity has not yet been examined for the sheared situation. Dynamical heterogeneity may play an important role in the drastic change of the dynamics due to not only the decreasing temperature but also the increasing shear rate. However, the role of dynamical heterogeneity remains unclear and is an important question.

Even in a strongly sheared state, supercooled liquids exhibit an almost isotropic structure and dynamics that can be captured via two-point correlation functions [17; 90; 131]. This is in marked contrast to common complex fluids, such as polymer solutions and colloidal suspensions, which exhibit anisotropic dynamics or structural changes that are induced by the shear flow [82; 101; 102]. The isotropic feature of supercooled liquids strongly supports the possibility of the "mapping concept", that is, that the sheared non-equilibrium state can be mapped onto the quiescent equilibrium state. In fact, previous studies [131; 132] have demonstrated that the shear viscosity η and the diffusion constant D in the sheared state can be mapped onto those in the equilibrium state through the α-relaxation time τ_α. The research by Ref. [56] also reported that the shear stress and the inherent structure energy can be mapped through the effective temperature $T_{\rm eff}$, which is measured from the relation between the static linear response and the variance of the pressure. More interestingly, there are some results regarding the mapping of the dynamical heterogeneity. An earlier study [131] examined the heterogeneous structure of the bond breakages under the sheared situation and found that the correlation length of the bond breakages is described as a function of only the α-relaxation time. Furthermore, recent research [98] has found that the number n^* of particles in correlated region (equivalent to the intensity χ_4) can be scaled as $n^* \sim (\dot{\gamma}\Delta\phi^4)^{-0.3}$, where $\dot{\gamma}$ is the shear rate of the shear flow, and $\Delta\phi$ is the distance from the random close-packing volume fraction. This result means that the intensity can be mapped through a single parameter $\dot{\gamma}\Delta\phi^4$.

In the present study, we examined the dynamical heterogeneity in the sheared non-equilibrium situation using molecular-dynamics (MD) simulations. Three quantities (correlation length, intensity, and lifetime) characterizing the dynamical heterogeneity were quantified by means of the four-point correlation functions. We found the behaviors of decreasing of not only the correlation length ξ_4 and the intensity χ_4 but also the lifetime $\tau_{\rm hetero}$ with increasing the shear rate $\dot{\gamma}$. Furthermore, we also examined the validity of the mapping concept for all three quantities of the dynamical heterogeneity.

The mapping concept can lead to the concept of an effective temperature, which is also interesting and important for glassy systems. For glassy systems, it has been suggested that when considering the long time scale, the equilibrium form of the FDT holds well with the temperature T, which is replaced by a different value denoted as $T_{\rm eff}$, i.e., the effective temperature [13; 14; 78; 86; 88; 99; 100; 106; 135]. If the concept of an effective temperature is valid, then

the effective temperature plays a role as the temperature in the non-equilibrium situation, and the sheared non-equilibrium state can correspond to the equilibrium state with the effective temperature $T_{\rm eff}$. However, there are difficulties regarding the mapping concept and the effective temperature. A recent numerical simulation [46] found out the anisotropic dynamics in a sheared supercooled liquid by the four-point correlation function. This finding indicates that the sheared state cannot completely be mapped onto the equilibrium state. Furthermore, the validity of the value $T_{\rm eff}$, which is calculated from the relation between the response function and its associated correlation function, remains uncertain. Although several different observables yield a common value of $T_{\rm eff}$ [13; 86; 100; 106], some observables do not provide consistent values of $T_{\rm eff}$ [99; 135]. Therefore, only one value of $T_{\rm eff}$ may not completely describe the non-equilibrium state. Despite these difficulties, the mapping concept and the effective temperature are very attractive and interesting.

This chapter is organized as follows. In Sec. 3.2, we briefly review our MD simulation and the correlation functions of the particle dynamics. In this section, we extend the correlation functions to the present sheared condition. In Sec. 3.3, we present our results. First, we show the shear rate dependences of the correlation length, the intensity, and the lifetime, and then we demonstrate whether the mapping concept is valid for these three quantities. In Sec. 3.4, we summarize our results.

3.2 Simulation model and correlation functions of particle dynamics

3.2.A Simulation model

We performed MD simulations in three dimensions. Our simulation model is a mixture of two different size atomic species, 1 and 2. The particles interact via the soft-sphere potential $v_{ab}(r) = \epsilon(\sigma_{ab}/r)^{12}$ with $\sigma_{ab} = (\sigma_a + \sigma_b)/2$, where r is the distance between two particles, σ_a is the particle size, and $a, b \in 1, 2$. The interaction was truncated at $r = 3\sigma_{ab}$. We took the mass ratio to be $m_2/m_1 = 2$ and the size ratio to be $\sigma_2/\sigma_1 = 1.2$. This diameter ratio avoided system crystallization and ensured that an amorphous supercooled state occurred at low temperatures [89]. As in our previous study [91] (Chapter 2), we used two systems: a small system with $N_1 = N_2 = 5 \times 10^3$ ($N = N_1 + N_2 = 10^4$) particles and a large system with $N_1 = N_2 = 5 \times 10^4$ ($N = N_1 + N_2 = 10^5$) particles. We quantified the correlation length $\xi_4(t)$ and the intensity $\chi_4(t)$ with the large system, and we quantified the lifetime $\tau_{\rm hetero}(t)$ with the small system. In the following, space,

time, and temperature were measured by σ_1, $\tau_0 = (m_1\sigma_1^2/\epsilon)^{1/2}$, and ϵ/k_B, respectively. The particle density was fixed at a value of $\rho = (N_1 + N_2)/V = 0.8$, and the system length was $L = V^{1/3} = 23.2$ and 50.0 for the small and large systems, respectively. The temperature was set as $T = 0.772,\ 0.473,\ 0.352,\ 0.306,\ 0.267$, and 0.253. Note that the freezing point of the corresponding one-component model is approximately $T = 0.772$ [89]. At $T = 0.253$, the system is in a highly supercooled state. We applied a steady shear flow on our system with the Lees-Edwards periodic boundary condition [39]. We integrated the so-called SLLOD equations of motion with the Lees-Edwards periodic boundary condition, and the temperature was maintained at a desired value using a Gaussian constraint thermostat. Here, we set the x axis and the y axis along the flow direction and the velocity gradient direction of the steady shear flow, respectively. The mean velocity profile is $\langle \boldsymbol{v} \rangle = \dot{\gamma} y \boldsymbol{e}_x$, where $\boldsymbol{e}_x$ is the unit vector in the x direction. The details of this simulation model can be found in previous studies [90; 131].

3.2.B Correlation functions of particle dynamics

In our previous studies [91; 92] (Chapter 2), we investigated dynamical heterogeneity in the unsheared equilibrium state. With the correlation functions of the particle dynamics, we quantified the correlation length $\xi_4(t)$, the intensity $\chi_4(t)$, and the lifetime $\tau_{\text{hetero}}(t)$, three of which characterize the static and dynamic properties of dynamical heterogeneity. In those studies [91; 92], we defined an order parameter $\delta\hat{\mathcal{D}}_1(\boldsymbol{r}, t_0, t)$ and its Fourier component $\delta\mathcal{D}_1(\boldsymbol{q}, t_0, t)$ as the local fluctuations in the particle mobility. In the present study, we extended $\delta\hat{\mathcal{D}}_1(\boldsymbol{r}, t_0, t)$ and $\delta\mathcal{D}_1(\boldsymbol{q}, t_0, t)$ to the sheared condition as follows [46]. A position $\boldsymbol{r}(t_0) = (x(t_0), y(t_0))$ on the reference frame at a time t_0 moves to $\boldsymbol{r}(t_0) + \dot{\gamma} t y(t_0) \boldsymbol{e}_x$ at a time $t_0 + t$ by the mean shear flow. Therefore, we must define the mobility $a_{1j}^2(t_0, t)$ of the particle j by

$$a_{1j}^2(t_0, t) = \frac{[\boldsymbol{r}_{1j}(t_0 + t) - \boldsymbol{r}_{1j}(t_0) - \dot{\gamma} t y_{1j}(t_0) \boldsymbol{e}_x]^2}{\langle [\boldsymbol{r}_{1j}(t_0 + t) - \boldsymbol{r}_{1j}(t_0) - \dot{\gamma} t y_{1j}(t_0) \boldsymbol{e}_x]^2 \rangle}. \tag{3.1}$$

Note that when $a_{1j}^2(t_0, t) \geq 1$ ($a_{1j}^2(t_0, t) < 1$), the particle j moves more (less) than the mean value of the single-particle displacement, i.e., the particle j is mobile (immobile). Using this definition of particle mobility, we extended $\delta\hat{\mathcal{D}}_1(\boldsymbol{r}, t_0, t)$ and $\delta\mathcal{D}_1(\boldsymbol{q}, t_0, t)$ to the sheared condition as

$$\begin{aligned} \delta\hat{\mathcal{D}}_1(\boldsymbol{r}, t_0, t) &= \sum_{j=1}^{N_1} [a_{1j}^2(t_0, t) - 1] \delta(\boldsymbol{r} - \boldsymbol{R}_{1j}(t_0, t)), \\ \delta\mathcal{D}_1(\boldsymbol{q}, t_0, t) &= \sum_{j=1}^{N_1} [a_{1j}^2(t_0, t) - 1] \exp[-i\boldsymbol{q} \cdot \boldsymbol{R}_{1j}(t_0, t)], \end{aligned} \tag{3.2}$$

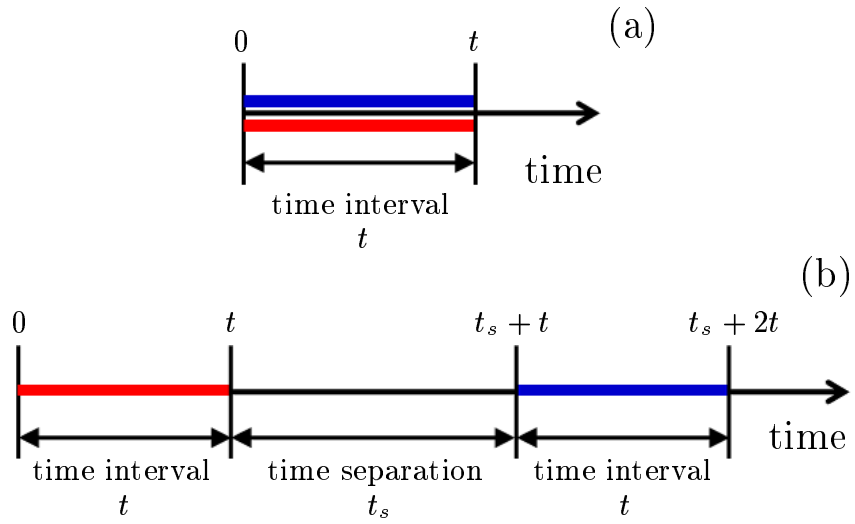

Figure 3.1: Schematic illustration of the time configuration of the correlation functions of the particle dynamics: (a) $S_4(q,t)$ (b) $S_{\mathcal{D}}(q,t_s,t)$.

where $\boldsymbol{R}_{1j}(t_0,t) = (\boldsymbol{r}_{1j}(t_0) + \boldsymbol{r}_{1j}(t_0+t))/2$.

Using the order parameter $\delta\mathcal{D}_1(\boldsymbol{q},t_0,t)$, we define the spatial correlation function $S_4(q,t)$ of the particle dynamics as

$$S_4(q,t) = \frac{1}{N_1}\langle \delta\mathcal{D}_1(\boldsymbol{q},0,t)\delta\mathcal{D}_1(-\boldsymbol{q},0,t)\rangle, \tag{3.3}$$

where the $\langle\cdots\rangle$ represents the ensemble average over time 0 and the angular components of the wave vector $\boldsymbol{q}$. The function $S_4(q,t)$ represents the spatial correlation of the particle dynamics in the time interval $[0,t]$. The time configuration of $S_4(q,t)$ is schematically illustrated in Fig. 3.1(a). We are able to quantify the correlation length $\xi_4(t)$ and the intensity $\chi_4(t)$ by fitting $S_4(q,t)$ to the Ornstein-Zernike (OZ) form at small wavenumbers q [80; 131],

$$S_4(q,t) = \frac{\chi_4(t)}{1+q^2\xi_4(t)^2}. \tag{3.4}$$

Note that to obtain accurate values of $\xi_4(t)$ and $\chi_4(t)$, $S_4(q,t)$ must be fitted to the OZ form in the range of $q\xi_4(t) < 1.5$ [41; 42]. We used a large system with 10^5 particles and carefully fitted $S_4(q,t)$ to the OZ form.

In addition, we also define the time correlation function $S_{\mathcal{D}}(q,t_s,t)$ of the particle dynamics as

$$S_{\mathcal{D}}(q,t_s,t) = \langle \delta\mathcal{D}_1(\boldsymbol{q},t_s+t,t)\delta\mathcal{D}_1(-\boldsymbol{q},0,t)\rangle, \tag{3.5}$$

where the $\langle\cdots\rangle$ represents the ensemble average over the initial time 0 and the angular components of the wave vector $\boldsymbol{q}$. The function $S_{\mathcal{D}}(q,t_s,t)$ represents the correlation of the particle dynamics between two time intervals $[0,t]$ and $[t_s+t,t_s+2t]$, where the value t_s is the time separation. The

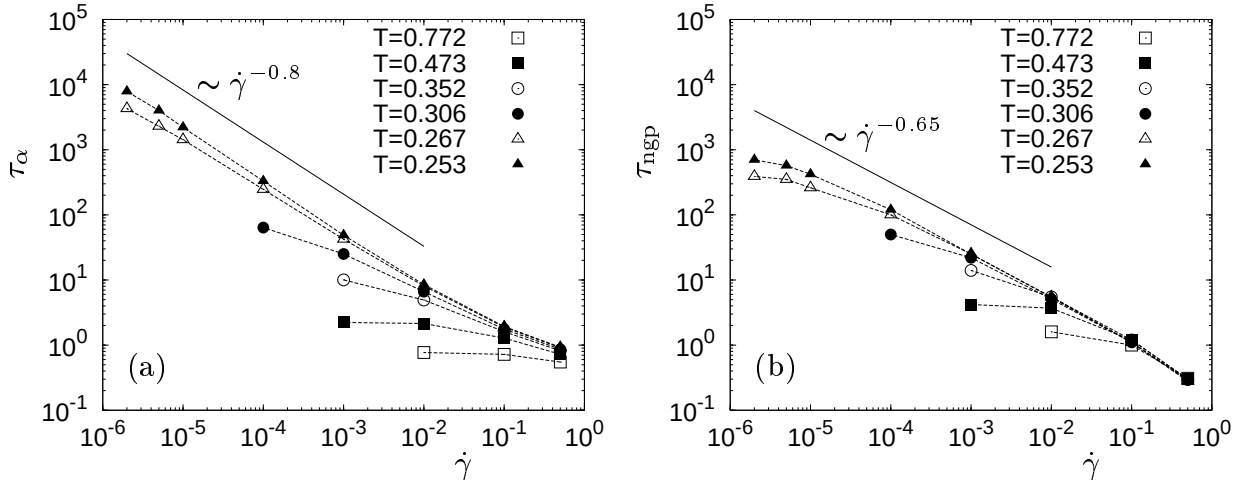

Figure 3.2: The shear-rate dependence of (a) τ_α and (b) $\tau_{\rm ngp}$ for various temperatures. We used these two time intervals to define the particle dynamics.

time configuration of $S_{\mathcal{D}}(q, t_s, t)$ is schematically illustrated in Fig. 3.1(b). Here, when calculating the ensemble average over the wave vector $\boldsymbol{q}$, we took only $\boldsymbol{q}$ perpendicular to x direction, i.e., $\boldsymbol{q}$ perpendicular to the shear flow direction, to eliminate the time decay due to the shear flow. As the time separation t_s increases, $S_{\mathcal{D}}(q, t_s, t)$ decays in the stretched exponential form,

$$\frac{S_{\mathcal{D}}(q, t_s, t)}{S_{\mathcal{D}}(q, 0, t)} \sim \exp\left(-\left(\frac{t_s}{\tau_h(q,t)}\right)^c\right), \tag{3.6}$$

where $\tau_h(q,t)$ is the wavenumber-dependent relaxation time of $S_{\mathcal{D}}(q, t_s, t)$. The lifetime $\tau_{\rm hetero}(t)$ was determined as $\tau_{\rm hetero}(t) = \tau_h(q,t)$ at $q = 0.38$. We used a small system with 10^4 particles to obtain the lifetime $\tau_{\rm hetero}(t)$.

As we mentioned previously, recent research [46] has indicated that the correlation functions of the particle dynamics (the four-point correlation functions) depend on the direction of the wave vector $\boldsymbol{q}$ in the sheared situation, although the two point correlation functions hardly exhibit any anisotropy. Therefore, three quantities ($\xi_4(t)$, $\chi_4(t)$, and $\tau_{\rm hetero}(t)$) also depend on the direction of $\boldsymbol{q}$. In the present study, we did not examine the directional dependence of the dynamical heterogeneity, even though it is interesting and important. Rather, we examined the dynamical heterogeneity and its three quantities averaged over the direction of the wave vector $\boldsymbol{q}$.

3.3 Results

To define the particle dynamics, we used two time intervals as in our previous studies [91; 92]. One is the α-relaxation time τ_α defined by $F_s(k_m, \tau_\alpha) = e^{-1}$. Here, $F_s(k,t)$ is the self-part of the density

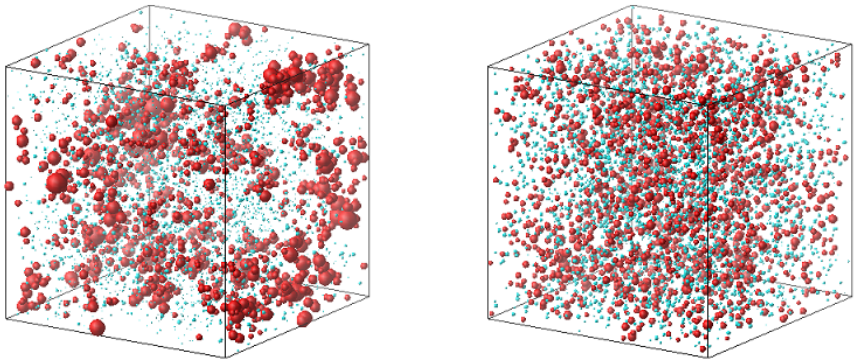

(a) $t = \tau_\alpha$ and $\dot{\gamma} = 10^{-5}$

(b) $t = \tau_\alpha$ and $\dot{\gamma} = 10^{-1}$

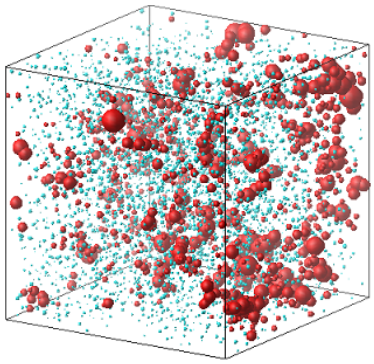

(c) $t = \tau_{\rm ngp}$ and $\dot{\gamma} = 10^{-5}$

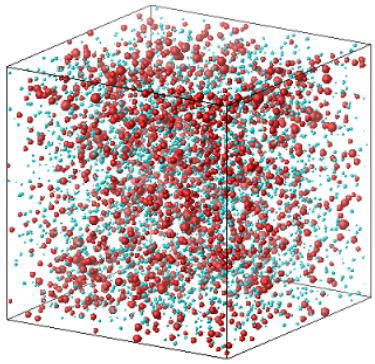

(d) $t = \tau_{\rm ngp}$ and $\dot{\gamma} = 10^{-1}$

Figure 3.3: The visualization of the heterogeneous dynamics for Particle Species 1. The temperature is 0.267. The time interval is $[t_0, t_0 + \tau_\alpha](t = \tau_\alpha)$ in (a) and (b) and $[t_0, t_0 + \tau_{\rm ngp}](t = \tau_{\rm ngp})$ in (c) and (d). The shear rates are 10^{-5} in (a) and (c) and 10^{-1} in (b) and (d). The radii of the spheres are $a_{1j}^2(t_0, t)$, and the centers are at $\boldsymbol{R}_{1j}(t_0, t)$. The red and blue spheres represent $a_{1j}^2(t_0, t) \geq 1$ (mobile particles) and $a_{1j}^2(t_0, t) < 1$ (immobile particles), respectively.

correlation function for Particle Species 1, which is defined as $F_s(k,t) = 1/N_1 \left\langle \sum_{j=1}^{N_1} e^{-i\boldsymbol{k}\cdot[\boldsymbol{r}_{1j}(t) - \boldsymbol{r}_{1j}(0) - \dot{\gamma} t y_{1j}(t) \boldsymbol{e}_x]} \right\rangle$, and $k_m = 2\pi$ is the first peak wave number of the static structure factor. We note that, as already shown in Refs. [17; 90; 131], any angular dependence in $F_s(\boldsymbol{k}, t)$ is barely notable despite the presence of the shear flow in the x direction. Figure 3.2(a) shows τ_α as a function of the shear rate $\dot{\gamma}$. The value τ_α monotonically decreases with increasing $\dot{\gamma}$ as $\tau_\alpha \sim \dot{\gamma}^{-\nu}$ with $\nu \simeq 0.8$ [17; 90; 131]. Note that the marked shear thinning occurs in the region of the shear rate that we considered.

The other time interval is the time $\tau_{\rm ngp}$ at which non-Gaussian parameter $\alpha_2(t)$ of the Van Hove self-correlation function is maximized. Here, we introduce a displacement $\Delta \boldsymbol{r}'_{1j}(t)$ of the particle j, which is defined as $\Delta \boldsymbol{r}'_{1j}(t) = \boldsymbol{r}_{1j}(t) - \boldsymbol{r}_{1j}(0) - \dot{\gamma} \int_0^t ds y_{1j}(s) \boldsymbol{e}_x$, in which the contribution from the convective transport by the average shear flow is subtracted [131]. By using this displacement,

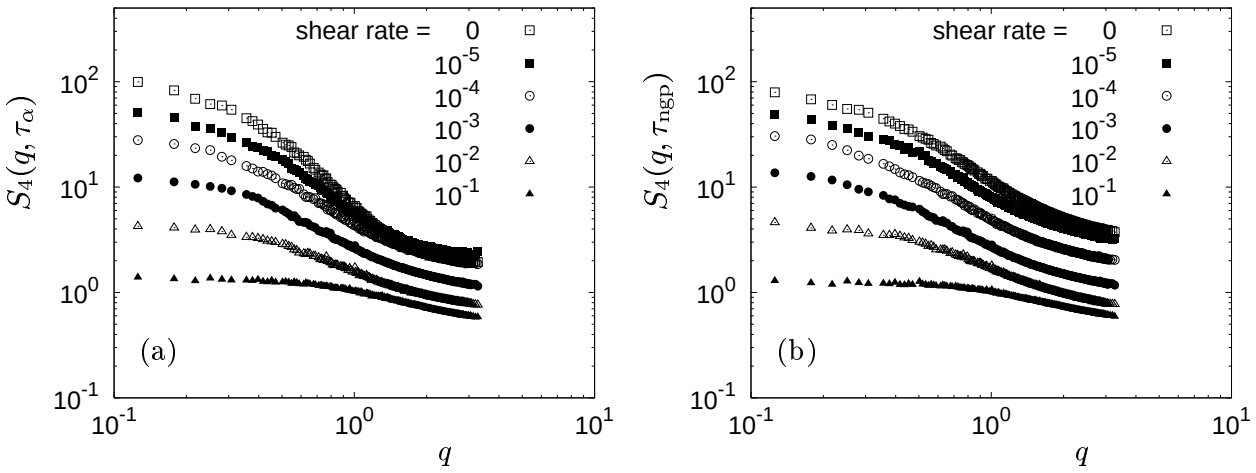

Figure 3.4: The spatial correlation function $S_4(q,t)$ for Particle Species 1. The temperature is $T = 0.267$. The time interval t is τ_α in (a) and $\tau_{\rm ngp}$ in (b). The shear rate $\dot\gamma$ is 0, 10^{-5}, 10^{-4}, 10^{-3}, 10^{-2} and 10^{-1} from the highest curve to the lowest. Note that $S_4(q,t)$ was calculated with a larger system $N = 10^5$.

we define $\alpha_2(t) = 3\langle[\Delta \boldsymbol{r}'_1(t)]^4\rangle/5\langle[\Delta \boldsymbol{r}'_1(t)]^2\rangle^2 - 1$. In Fig. 3.2(b), we plot $\tau_{\rm ngp}$ as a function of $\dot\gamma$. Similar to τ_α, $\tau_{\rm ngp}$ also decreases with increasing $\dot\gamma$ as $\tau_{\rm ngp} \sim \dot\gamma^{-0.65}$. This behavior of $\tau_{\rm ngp}$ was also experimentally observed in Ref. [17].

3.3.A Heterogeneous dynamics under shear flow

First, we visualized the heterogeneous dynamics under a steady shear flow. We show the spatial distribution of the particle mobility $a_{1j}^2(t_0,t)$ for Particle Species 1 in Fig. 3.3, where the particles are drawn as spheres with radii $a_j^2(t_0,t)$ located at $\boldsymbol{R}_j(t_0,t)$. The time interval is $t = \tau_\alpha$ and $t = \tau_{\rm ngp}$, and the temperature is $T = 0.267$. We demonstrate that the heterogeneity is significant at $\dot\gamma = 10^{-5}$ but greatly weakened at $\dot\gamma = 10^{-1}$ for both time intervals $t = \tau_\alpha$ and $\tau_{\rm ngp}$. Therefore, the strong shear flow suppresses the heterogeneous structure. The same observation has also been observed in the heterogeneity of the bond breakage [131] and of the "overlapping" function [46; 57; 58; 98; 120].

3.3.B Correlation length and intensity of dynamical heterogeneity

Next, we quantified the correlation length $\xi_4(t)$ and the intensity $\chi_4(t)$ of the dynamical heterogeneity. We calculated the spatial correlation function $S_4(q,t)$ defined in Eq. (3.3). Note that we used a large system with 10^5 particles for the calculation of $S_4(q,t)$. Figure 3.4 shows the wave number q dependence of $S_4(q,t)$ for various shear rates $\dot\gamma$. The temperature is $T = 0.267$. It can be observed that $S_4(q,t)$ at small wave numbers q (long-distance scales) for $t = \tau_\alpha$ and $\tau_{\rm ngp}$ decreases as the shear rate $\dot\gamma$ increases. Therefore, the heterogeneous structure is weakened due to the steady

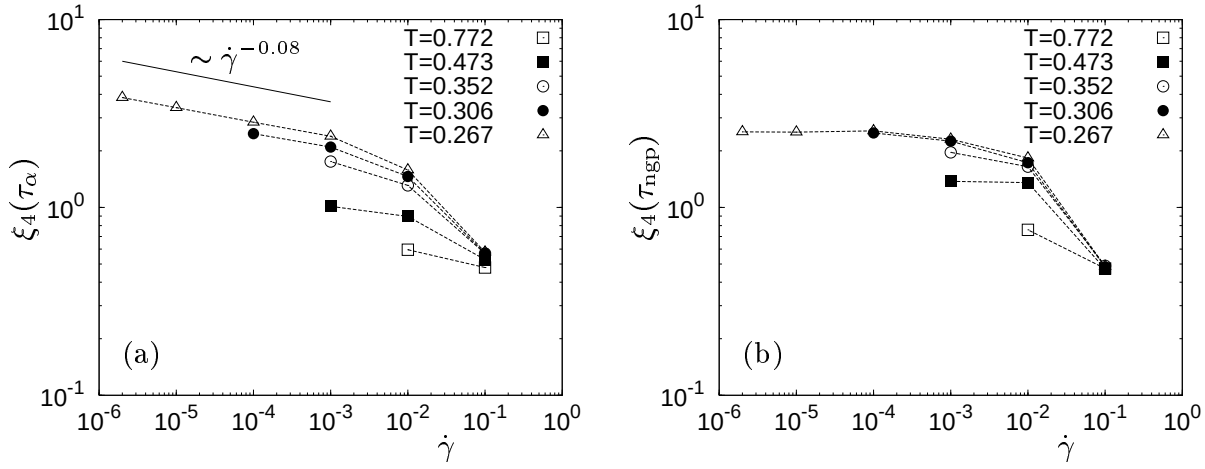

Figure 3.5: The shear rate dependence of the correlation length $\xi_4(t)$ for various temperatures. The time interval t is (a) τ_α and (b) $\tau_{\rm ngp}$.

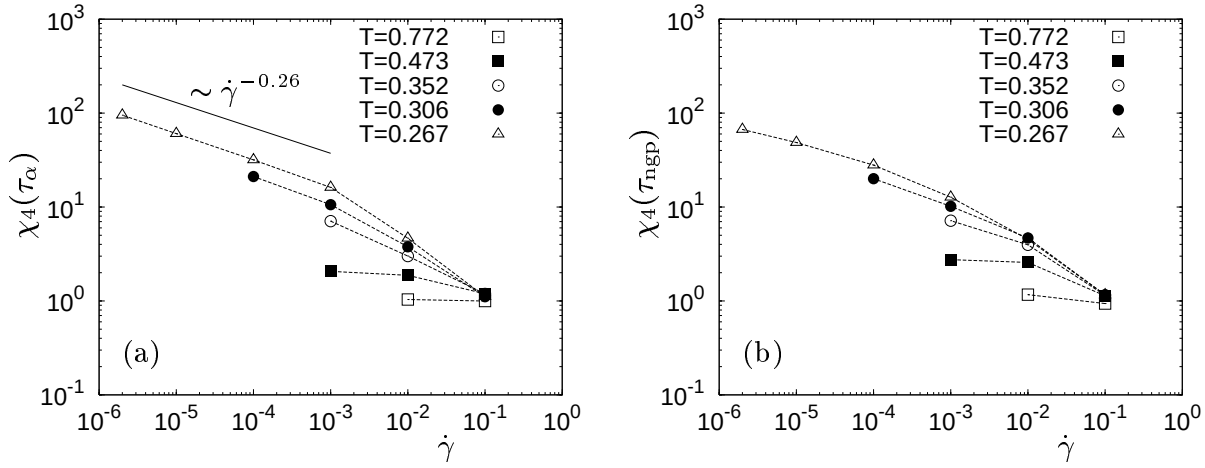

Figure 3.6: The shear-rate dependence of the intensity $\chi_4(t)$ for various temperatures. The time interval t is (a) τ_α and (b) $\tau_{\rm ngp}$.

shear flow as is also shown in Fig. 3.3.

We quantified the correlation length $\xi_4(t)$ and the intensity $\chi_4(t)$ by fitting the function $S_4(q,t)$ to the OZ form in Eq. (3.4). Note that $S_4(q,t)$ was carefully fitted to the OZ form in the range of $q\xi_4(t) < 1.5$ to obtain accurate values of $\xi_4(t)$ and $\chi_4(t)$ [41; 42]. In Figs. 3.5 and 3.6, we show the shear rate $\dot{\gamma}$ dependences of the correlation length $\xi_4(t)$ and the intensity $\chi_4(t)$ for various temperatures. It is clear that both $\xi_4(t)$ and $\chi_4(t)$ decrease as $\dot{\gamma}$ increases for the time intervals $t = \tau_\alpha$ and $\tau_{\rm ngp}$. For the time interval $t = \tau_\alpha$, $\xi_4(\tau_\alpha)$ and $\chi_4(\tau_\alpha)$ can be scaled as $\xi_4(\tau_\alpha) \sim \dot{\gamma}^{-0.08}$ and $\chi_4(\tau_\alpha) \sim \dot{\gamma}^{-0.26}$ in Figs. 3.5(a) and 3.6(a), respectively. The scaling component 2.6 of $\chi_4(\tau_\alpha) \sim \dot{\gamma}^{-0.26}$ agrees well with 0.3 in Refs. [98; 120] but disagrees with $0.4 - 0.6$ in Ref. [58].

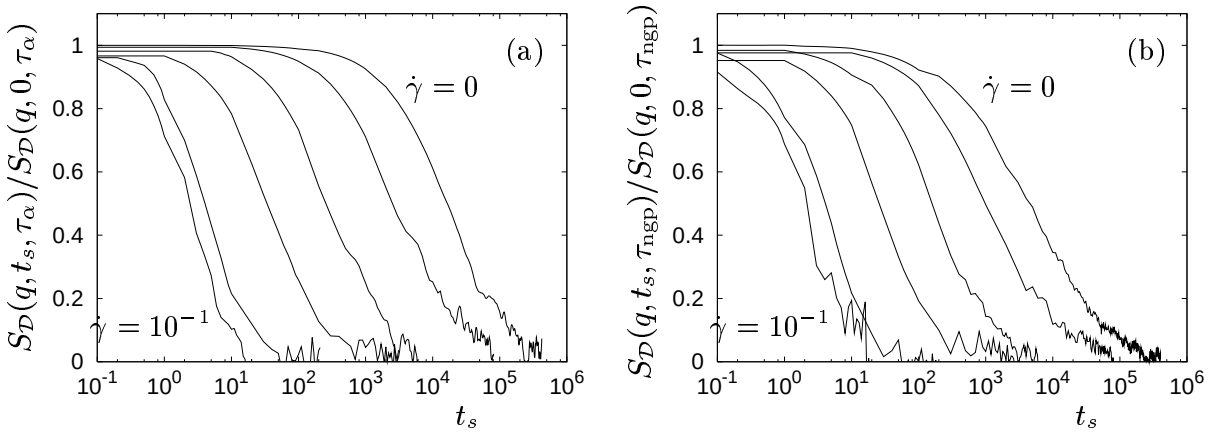

Figure 3.7: The time decay of $S_{\mathcal{D}}(q, t_s, t)$ for particle species 1 at $q = 0.38$. The time interval t is τ_α in (a) and $\tau_{\rm ngp}$ in (b). Temperature is 0.267. The shear rates $\dot{\gamma}$ are 0, 10^{-5}, 10^{-4}, 10^{-3}, 10^{-2} and 10^{-1} from right to left.

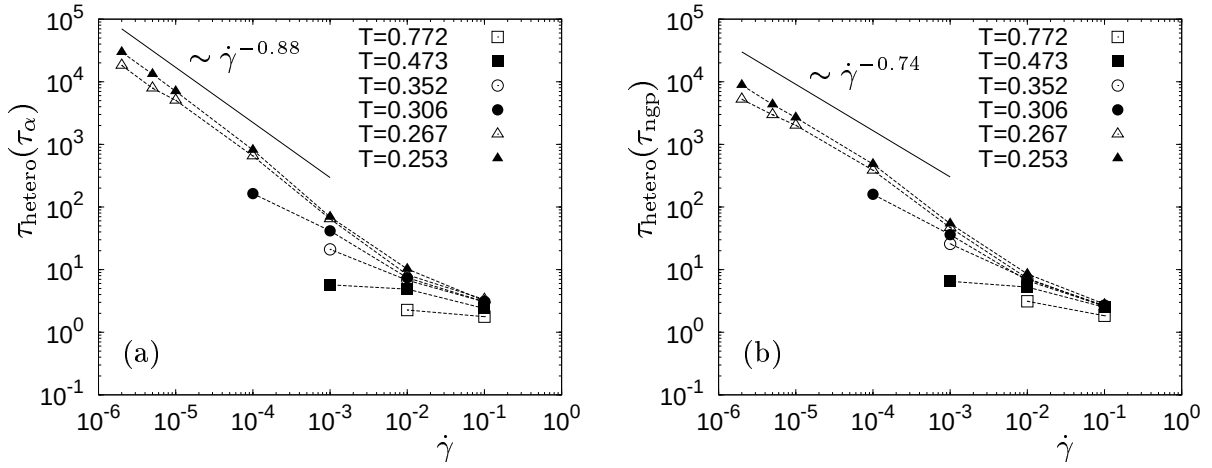

Figure 3.8: The shear-rate dependence of the lifetime $\tau_{\rm hetero}(t)$ for various temperatures. The time interval t is (a) τ_α and (b) $\tau_{\rm ngp}$.

3.3.C Lifetime of heterogeneous dynamics

Next, we quantified the lifetime $\tau_{\rm hetero}(t)$ of the dynamical heterogeneity in terms of the correlation function $S_{\mathcal{D}}(q, t_s, t)$ defined in Eq. (3.5). We calculated $S_{\mathcal{D}}(q, t_s, t)$ for the time intervals $t = \tau_\alpha$ and $\tau_{\rm ngp}$. Figure 3.7 shows the time decay of $S_{\mathcal{D}}(q, t_s, t)$ at $q = 0.38$ for various shear rates $\dot{\gamma}$. Note that $q = 0.38$ is the smallest waver number (the longest distance scale) that we used in calculating $S_{\mathcal{D}}(q, t_s, t)$. $S_{\mathcal{D}}(q, t_s, t)$ decays in the stretched exponential form with increasing the time separation t_s. As shown in Fig. 3.7, as the shear rate $\dot{\gamma}$ increases, $S_{\mathcal{D}}(q, t_s, t)$ for both $t = \tau_\alpha$ and $\tau_{\rm ngp}$ decays faster.

We quantified the lifetime $\tau_{\rm hetero}(t)$ using the relaxation time of $S_{\mathcal{D}}(q, t_s, t)$ as in Eq. (3.6).

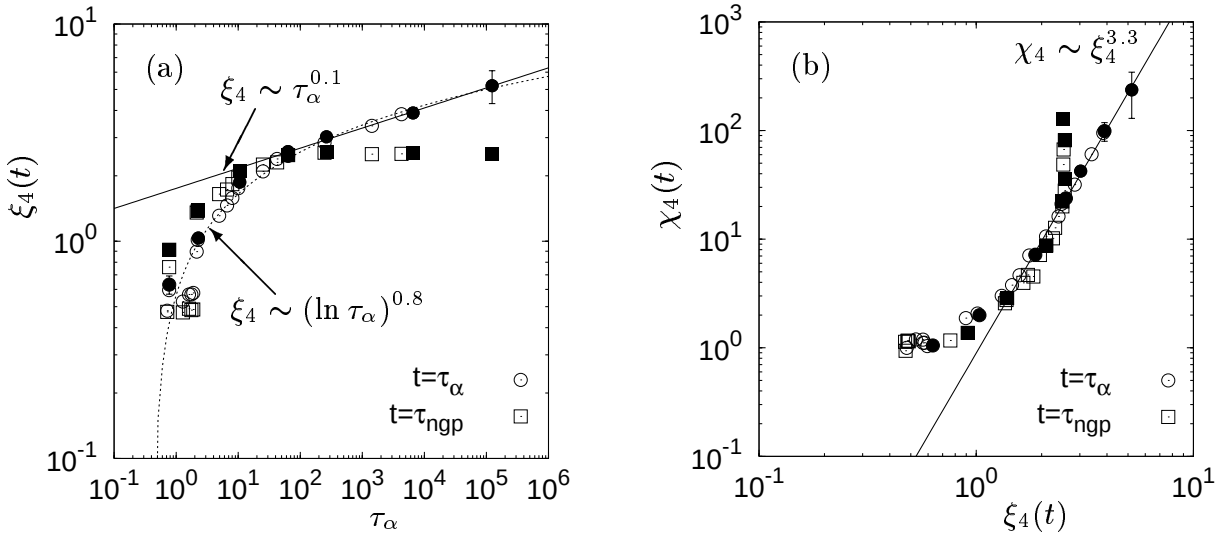

Figure 3.9: (a) The correlation length $\xi_4(t)$ versus the α-relaxation time τ_α. (b) The intensity $\chi_4(t)$ versus the correlation length $\xi_4(t)$. The time intervals are $t = \tau_\alpha$ and $\tau_{\rm ngp}$. The white symbols are the values of $\xi_4(t)$ and $\chi_4(t)$ under shear flows. The black symbols are the values in the equilibrium states from Ref. [92]. The straight lines are power law fits: $\xi_4(\tau_\alpha) \sim \tau_\alpha^{0.1\pm0.01}$ in (a) and $\chi_4(\tau_\alpha) \sim \xi_4(\tau_\alpha)^{3.3\pm0.1}$ in (b). The dashed curve is fit to $\xi_4(\tau_\alpha) \sim (\ln \tau_\alpha)^{0.8\pm0.05}$.

Figure 3.8 shows $\tau_{\rm hetero}(t)$ for $t = \tau_\alpha$ and $\tau_{\rm ngp}$ as a function of $\dot\gamma$. Similar to τ_α and $\tau_{\rm ngp}$, $\tau_{\rm hetero}(t)$ also becomes small as $\dot\gamma$ becomes large. Here, the scalings $\tau_{\rm hetero}(\tau_\alpha) \sim \dot\gamma^{-0.88}$ and $\tau_{\rm hetero}(\tau_{\rm ngp}) \sim \dot\gamma^{-0.74}$ are observed. The steady shear flow decreases the lifetime of the dynamical heterogeneity as well as the correlation length and the intensity. By comparing three scalings $\xi_4 \sim \dot\gamma^{-0.08}$, $\chi_4 \sim \dot\gamma^{-0.26}$, and $\tau_{\rm hetero} \sim \dot\gamma^{-0.88}$ for the time interval $t = \tau_\alpha$, we note that the lifetime is much more sensitive to the shear rate $\dot\gamma$ than the correlation length and the intensity. Thus, the dynamical properties of the dynamical heterogeneity are altered much more by the shear flow than the static properties of the dynamical heterogeneity.

3.3.D Mapping concept for correlation length, intensity, and lifetime of dynamical heterogeneity

Finally, we demonstrated that three quantities, the correlation length $\xi_4(t)$, the intensity $\chi_4(t)$, and the lifetime $\tau_{\rm hetero}(t)$, can be mapped onto those in the equilibrium state. In Fig. 3.9(a), we plot $\xi_4(t)$ versus τ_α for both time intervals $t = \tau_\alpha$ and $\tau_{\rm ngp}$. In the same figure, we also plot the values in the equilibrium state. It can be observed that the values $\xi_4(t)$ for $t = \tau_\alpha$ and $\tau_{\rm ngp}$ collapse onto a single curve as a function of τ_α. This result means that the correlation length $\xi_4(t)$ in the sheared state can be mapped onto that in the equilibrium state through the α-relaxation time τ_α. For the time interval $t = \tau_\alpha$, we obtained the scaling relationships between $\xi_4(\tau_\alpha)$ and τ_α: $\xi_4(\tau_\alpha) \sim \tau_\alpha^{0.1}$

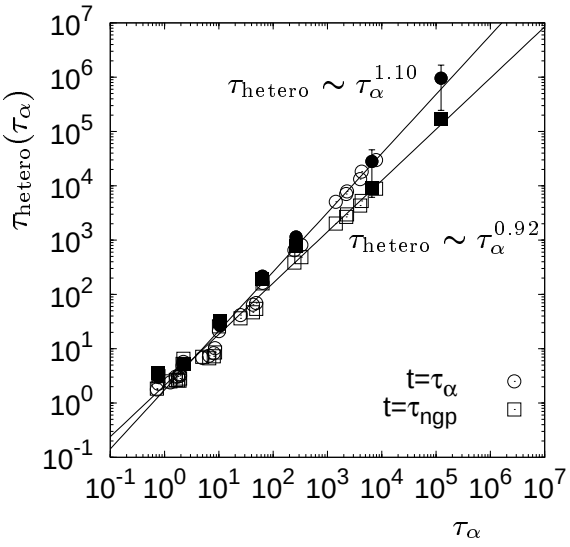

Figure 3.10: The lifetime $\tau_{\rm hetero}(t)$ versus the α-relaxation time τ_α. The time intervals are $t = \tau_\alpha$ and $\tau_{\rm ngp}$. The white symbols are the values of $\tau_{\rm hetero}(t)$ under shear flows. The black symbols are the values in the equilibrium states from Ref. [91]. The straight lines are power law fits: $\tau_{\rm hetero}(\tau_\alpha) \sim \tau_\alpha^{1.10\pm0.02}$ and $\tau_{\rm hetero}(\tau_{\rm ngp}) \sim \tau_\alpha^{0.92\pm0.02}$.

(a power law fit) or $\xi_4(\tau_\alpha) \sim (\ln \tau_\alpha)^{0.80}$ (a slower-than-power law fit). These fits are exactly the same as the equilibrium fits within the numerical errors [92]. In addition, in Fig. 3.9(b), we show $\chi_4(t)$ versus $\xi_4(t)$ for $t = \tau_\alpha$ and $\tau_{\rm ngp}$. From Fig. 3.9(b), similarly to $\xi_4(t)$, $\chi_4(t)$ also collapses onto a single curve as function of $\xi_4(t)$. Therefore, the values $\chi_4(t)$ in the sheared state can also be mapped onto those in the equilibrium state. For the time interval $t = \tau_\alpha$, we obtained the scaling relationship between $\chi_4(\tau_\alpha)$ and $\xi_4(\tau_\alpha)$. It is a power law fit $\chi_4(\tau_\alpha) \sim \xi_4(\tau_\alpha)^{3.3}$, which is same as the equilibrium fit within the numerical errors [92]. It should be noted that τ_α decreases with increasing $\dot\gamma$ as $\tau_\alpha \sim \dot\gamma^{-0.8}$, which leads to $\xi_4(\tau_\alpha) \sim \tau_\alpha^{0.1} \sim \dot\gamma^{-0.08}$ and $\chi_4(\tau_\alpha) \sim \xi_4(\tau_\alpha)^{3.3} \sim \dot\gamma^{-0.26}$. These scaling relations coincide with the observations in Figs. 3.5(a) and 3.6(a), respectively.

Furthermore, figure 3.10 shows the lifetime $\tau_{\rm hetero}(t)$ versus τ_α for $t = \tau_\alpha$ and $\tau_{\rm ngp}$. This figure shows that $\tau_{\rm hetero}(\tau_\alpha)$ and $\tau_{\rm hetero}(\tau_{\rm ngp})$ fall into the lines $\tau_{\rm hetero}(\tau_\alpha) \sim \tau_\alpha^{1.10}$ and $\tau_{\rm hetero}(\tau_{\rm ngp}) \sim \tau_\alpha^{0.92}$, similarly to $\xi_4(t)$ and $\chi_4(t)$. These lines are exactly same as the equilibrium ones within the numerical errors [91]. We note that $\tau_{\rm hetero}(\tau_\alpha) \sim \tau_\alpha^{1.10} \sim \dot\gamma^{-0.88}$ and $\tau_{\rm hetero}(\tau_{\rm ngp}) \sim \tau_\alpha^{0.92} \sim \dot\gamma^{-0.74}$ coincide with the observation in Fig. 3.8. Therefore, not only the correlation length and the intensity but also the lifetime can be mapped onto those in the equilibrium state through the α-relaxation time. As we mentioned, previous studies [56; 131; 132] have found that the material properties, such as the shear viscosity η and the diffusion constant D, under steady shear flow can be a single function of the α-relaxation time τ_α or the effective temperature $T_{\rm eff}$. Our results

demonstrated that the mapping concept is valid for the material properties (the shear viscosity and the diffusion constant) as well as the properties of dynamical heterogeneity (the correlation length, the intensity, and the lifetime).

3.4 Conclusion

In conclusion, we examined the dynamical heterogeneity in a supercooled liquid under sheared conditions. Dynamical heterogeneity can be characterized by three quantities: the correlation length $\xi_4(t)$, the intensity $\chi_4(t)$, and the lifetime $\tau_{\rm hetero}(t)$. Using the correlation functions of the particle dynamics, we quantified all three quantities for two time intervals $t = \tau_\alpha$ and $\tau_{\rm ngp}$. Our results demonstrated that not only the correlation length and the intensity but also the lifetime decrease as the shear rate $\dot{\gamma}$ increases. Therefore, the steady shear flow suppresses the length scale as well as the time scale of the dynamical heterogeneity. For the time interval $t = \tau_\alpha$, three quantities can be scaled as $\xi_4 \sim \dot{\gamma}^{-0.08}$, $\chi_4 \sim \dot{\gamma}^{-0.26}$, and $\tau_{\rm hetero} \sim \dot{\gamma}^{-0.88}$, which indicates that, due to the steady shear flow, the lifetime decreases much more than the correlation length and the intensity.

Furthermore, we numerically demonstrated that the values of $\xi_4(t)$, $\chi_4(t)$, and $\tau_{\rm hetero}(t)$ collapse onto a single curve as function of the α-relaxation τ_α similarly to the material properties such as the viscosity η and the diffusion constant D. For the time interval $t = \tau_\alpha$, we obtained exactly the same scaling relations between the three quantities as the equilibrium ones, i.e., $\xi_4 \sim \tau_\alpha^{0.1}$ (or $\xi_4 \sim (\ln \tau_\alpha)^{0.80}$), $\chi_4 \sim \xi_4^{3.3}$, and $\tau_{\rm hetero} \sim \tau_\alpha^{1.10}$. Our results indicate that three quantities of the dynamical heterogeneity can be mapped onto those in the equilibrium state, i.e., the mapping concept for three quantities is valid.

In the present study, we did not acknowledge the anisotropy of the dynamical heterogeneity, and the values of $\xi_4(t)$, $\chi_4(t)$, and $\tau_{\rm hetero}(t)$ were averaged over the direction of the wave vector $\boldsymbol{q}$. However, as we mentioned, the dynamical heterogeneity becomes anisotropic in the sheared situation, and the anisotropic dynamics can be related to shear-thinning [46]. How the dynamical heterogeneity and its three quantities depend on the direction of the wave vector $\boldsymbol{q}$ is interesting and important subject.

Chapter 4

Mechanical properties of a supercooled liquid

4.1 Introduction

A comprehensive theory of systems driven into non-equilibrium states is still very much under construction, in contrast to the well-established descriptions of equilibrium systems. Non-equilibrium states are generally characterized by violations of the fluctuation-dissipation theorem (FDT). The FDT relates the response functions to the associated correlation functions and holds in equilibrium states but is generally violated in non-equilibrium states. Much work has been devoted to understanding the relation between response functions and correlation functions in non-equilibrium situations, but this relation remains elusive and unclear (e.g., see refs. [7; 8; 26; 54; 116; 121] for recent works).

It has been reported that supercooled liquids exhibit simple natures even in non-equilibrium states. A strong shear flow can drive supercooled liquids into a highly non-equilibrium state. Even in such a highly non-equilibrium state, the structure and relaxation dynamics captured via the two-point correlation functions exhibit very little anisotropy [17; 90; 131]. This observation is in marked contrast to observations of other complex fluids such as polymer solutions and colloidal suspensions, in which structural changes or anisotropic dynamics are induced by a driving shear flow [82; 102]. Furthermore, in glassy systems, including supercooled liquids, it has been suggested that the equilibrium form of the FDT holds at long times with the temperature T replaced by an effective temperature $T_{\rm eff}$ [14], which indicates that $T_{\rm eff}$ can play a role like the temperature in the non-equilibrium situation and can provide a relation between the response and correlation functions. Several numerical and theoretical works have examined the validity and the role of the effective temperature [13; 56; 78; 100; 135].

Motivated by the above reports regarding the simple non-equilibrium properties of supercooled liquids, we investigated the shear stress responses and fluctuations of a supercooled liquid in a non-equilibrium state. We first drove the supercooled liquid into a non-equilibrium state using a steady shear flow, and we then examined the shear stress responses to oscillating shear strains in the non-equilibrium state. We also examined the correlation functions of the shear stress fluctuations

and tested the validity of the concept of an effective temperature. Shear stress responses and fluctuations are often useful for investigating non-equilibrium statistical mechanics [121]. The aim of this study was to reveal the behaviors of the shear stress responses and fluctuations of supercooled liquids in a non-equilibrium state.

It is worth mentioning some theoretical works on the mechanical responses of glassy systems: the soft glassy rheology model [114], the shear-transformation-zone theory [22], and the mode-coupling theory [23]. Furthermore, in the field of complex fluid rheology, some experimental works have examined the mechanical properties of polymer solutions under a steady shear flow [84; 115; 123] and have proposed the constitutive equations describing their results. Constitutive equations, which give the relations between the stress tensor and the strain tensor, play an important role in the field of fluid dynamics or transport phenomena [18; 19; 82]. In this study, we attempted to construct a constitutive equation for supercooled liquids from our simulation results.

The chapter is organized as follows. In Sec. 4.2, we briefly review our MD simulation and show three ways to apply an oscillating shear strain under a steady shear flow. In Sec. 4.3, the results are presented. We first show our MD simulation results of mechanical responses in the sheared states and construct a constitutive equation describing simulation results. Then, we present the results of the correlation functions of the shear stress fluctuations. Finally, we show a violation of FDT and the validity of the concept of an effective temperature. In Sec. 4.4, we summarize our results.

4.2 Simulation model and method

4.2.A Simulation model

In this work, we performed molecular dynamics (MD) simulations in three dimensions. Our model liquid is a mixture of two atomic species, 1 and 2, with $N_1 = N_2 = 5,000$. The particles interact via a soft-core potential $\phi(r) = \epsilon(\sigma_{ab}/r)^{12}$ with $\sigma_{ab} = (\sigma_a + \sigma_b)/2$, where r is the distance between two particles, σ_a is the particle size, and $a, b \in 1, 2$. The interaction was truncated at $r = 3\sigma_{ab}$. We set the mass and size ratios to be $m_2/m_1 = 2$ and $\sigma_2/\sigma_1 = 1.2$, respectively. This diameter ratio avoided system crystallization and ensured that an amorphous supercooled state formed at low temperatures [89]. The particle density was fixed at a value of $\rho = (N_1 + N_2)/V = 0.8/\sigma_1^3$, where the system length was $L = V^{1/3} = 23.2\sigma_1$. The temperature was fixed at a value of $T = 0.306\epsilon/k_B$. Note that the liquid was in the supercooled state at $\rho = 0.8/\sigma_1^3$ and $T = 0.306\epsilon/k_B$. In this study,

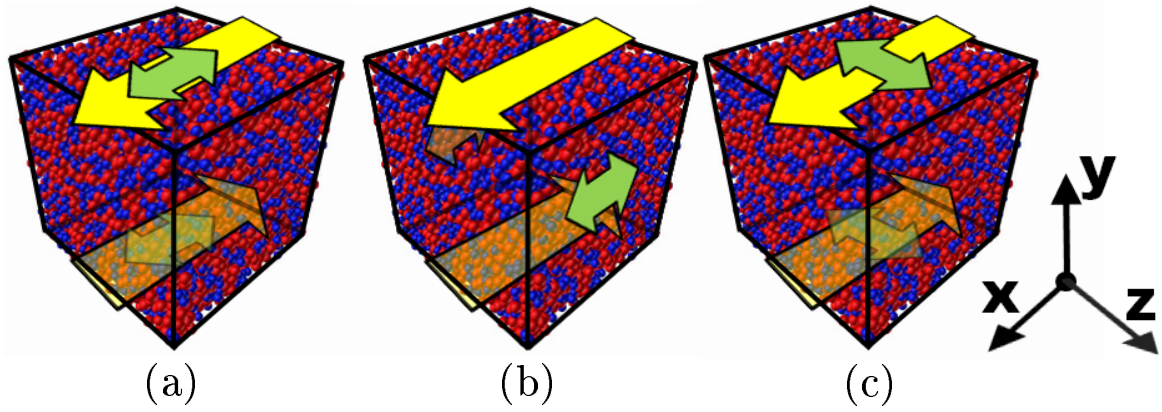

Figure 4.1: Schematic illustration of an applied steady shear flow (yellow arrow) and an oscillating shear strain (green arrow). The steady shear flow is applied as the xy component of the strain tensor $\boldsymbol{\gamma}$. The oscillating shear strain is applied as the xy, xz, and yz components of $\boldsymbol{\gamma}$ in (a), (b), and (c), respectively.

distances, times, and temperatures were measured in units of σ_1, $\tau_0 = (m_1\sigma_1^2/\epsilon)^{1/2}$, and ϵ/k_B, respectively. Shear flows were implemented by means of the Lees-Edwards boundary condition. We integrated the so-called SLLOD equations of motion with the Lees-Edwards boundary condition, and the temperature of the system was maintained by the Gaussian constraint thermostat [39].

4.2.B Way to apply steady shear flow and oscillating shear strain

We first applied a steady shear flow to drive the supercooled liquid into a non-equilibrium state [17; 90; 131]. We orient the x and y axes along the flow direction and the velocity gradient direction of the steady shear flow, respectively, as shown in Fig. 4.1. Figure 4.2 shows the shear-rate $\dot{\gamma}_s$ dependencies of the shear viscosity η and the α relaxation time τ_α at various temperatures T. The values of η and τ_α decrease with increasing $\dot{\gamma}_s$ as $\eta \propto \tau_\alpha \sim \dot{\gamma}_s^{-\nu}$ with $\nu = 0.7 \sim 0.8$, as shown by previous works [17; 90; 131]. In the present study, we focused on two non-equilibrium states, as indicated by the black circles in Fig. 4.2. First state is at $T = 0.306$ and $\dot{\gamma}_s = 10^{-4}$, where the supercooled liquid is in the weakly sheared state. Second state is at $T = 0.306$ and $\dot{\gamma}_s = 10^{-2}$, where the supercooled liquid is in the strongly sheared state. Notice that the marked shear thinning occurs in the strongly sheared state ($\dot{\gamma}_s = 10^{-2}$), as we can see from Fig. 4.2.

As is shown in Fig. 4.1, we next applied an oscillating shear strain $\delta\gamma^{ij}$ and examined the shear stress response $\delta\sigma^{ij}$ to $\delta\gamma^{ij}$, where γ^{ij} and σ^{ij} are the ij components of the strain tensor $\boldsymbol{\gamma} = \nabla\boldsymbol{u} + {}^t(\nabla\boldsymbol{u})$ and the stress tensor $\boldsymbol{\sigma}$, respectively, and $ij = xy$, xz, and yz. δ denotes the difference in a quantity from its value in the absence of an oscillating strain. It should be noted that

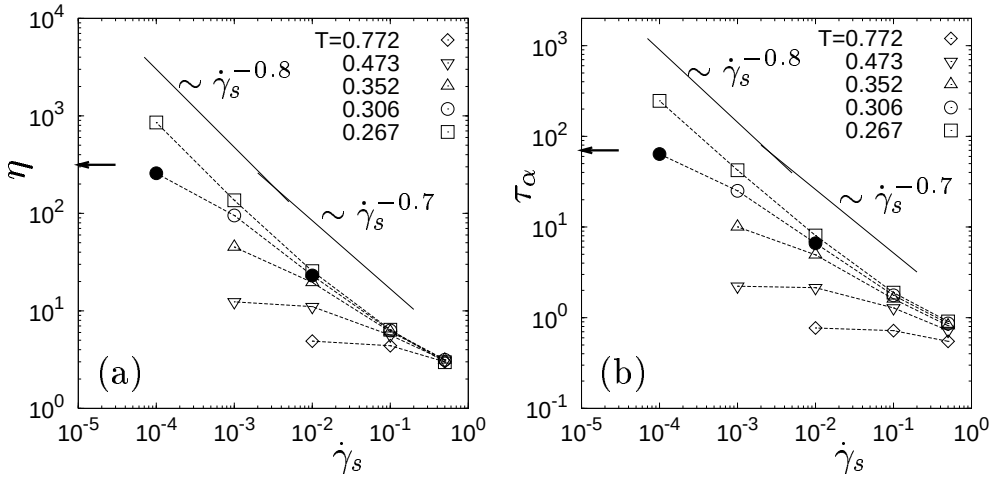

Figure 4.2: (a) The shear viscosity η and (b) the α-relaxation time τ_α versus $\dot{\gamma}_s$ for various temperatures. The arrows mean the values of η and τ_α at $T = 0.306$ and $\dot{\gamma}_s = 0$ (equilibrium state). In this study, we focused on two non-equilibrium states at $T = 0.306$ and $\dot{\gamma}_s = 10^{-4}$ (weakly sheared state) and $T = 0.306$ and $\dot{\gamma}_s = 10^{-2}$ (strongly sheared state), as indicated by the black circles. At $T = 0.306$ and $\dot{\gamma}_s = 10^{-2}$, the marked shear-thinning is observed.

even in the absence of an oscillating strain, σ^{xy} has a value $\sigma_s = \eta(\dot{\gamma}_s)\dot{\gamma}_s$ due to the steady shear flow, and therefore, we should calculate $\delta\sigma^{xy}$ as $\delta\sigma^{xy} = \sigma^{xy} - \sigma_s$. $\delta\sigma^{xz}$ and $\delta\sigma^{yz}$ are calculated as $\delta\sigma^{xz} = \sigma^{xz}$ and $\delta\sigma^{yz} = \sigma^{yz}$. We stress that there are three ways to apply an oscillating strain, as is well demonstrated in Fig. 4.1(a), (b), and (c). The strain tensor, $\boldsymbol{\gamma} = \nabla\boldsymbol{u} + {}^t(\nabla\boldsymbol{u})$, is described as follows.

$$\boldsymbol{\gamma} = \begin{pmatrix} 0 & \dot{\gamma}_s t + \delta\gamma^{xy} & 0 \\ \dot{\gamma}_s t + \delta\gamma^{xy} & 0 & 0 \\ 0 & 0 & 0 \end{pmatrix} \qquad \text{in Fig. 4.1(a)}, \tag{4.1}$$

$$\boldsymbol{\gamma} = \begin{pmatrix} 0 & \dot{\gamma}_s t & \delta\gamma^{xz} \\ \dot{\gamma}_s t & 0 & 0 \\ \delta\gamma^{xz} & 0 & 0 \end{pmatrix} \qquad \text{in Fig. 4.1(b)}, \tag{4.2}$$

$$\boldsymbol{\gamma} = \begin{pmatrix} 0 & \dot{\gamma}_s t & 0 \\ \dot{\gamma}_s t & 0 & \delta\gamma^{yz} \\ 0 & \delta\gamma^{yz} & 0 \end{pmatrix} \qquad \text{in Fig. 4.1(c)}. \tag{4.3}$$

We examined the three stress responses: $\delta\sigma^{xy}$ to $\delta\gamma^{xy}$ in Fig. 4.1(a), $\delta\sigma^{xz}$ to $\delta\gamma^{xz}$ in Fig. 4.1(b), and $\delta\sigma^{yz}$ to $\delta\gamma^{yz}$ in Fig. 4.1(c). In the present situation in which a steady shear flow is applied, these three stress responses ($\delta\sigma^{xy}$ to $\delta\gamma^{xy}$, $\delta\sigma^{xz}$ to $\delta\gamma^{xz}$, and $\delta\sigma^{yz}$ to $\delta\gamma^{yz}$) are generally different, whereas these three stress responses are exactly the same in the equilibrium state. The oscillating shear strain was expressed in a sinusoidal form: $\delta\gamma^{ij} = \gamma_0 \sin\omega t$, where γ_0 and ω are the amplitude and the frequency of the oscillating strain, respectively. In this study, we considered two amplitudes: $\gamma_0 = 10^{-2}$ and 10^{-1}. We should note that the amplitude $\gamma_0 = 10^{-2}$ is small enough that $\delta\sigma^{ij}$ is

linear with respect to $\delta\gamma^{ij}$. On the other hand, the amplitude $\gamma_0 = 10^{-1}$ is large so that $\delta\sigma^{ij}$ is non-linear with respect to $\delta\gamma^{ij}$.

It is useful to utilize the shear moduli $G'^{ij}_{\dot{\gamma}_s}(\omega)$ and $G''^{ij}_{\dot{\gamma}_s}(\omega)$ instead of the full time history $\delta\sigma^{ij}(t)$, where the subscript "$\dot{\gamma}_s$" denotes a value in the non-equilibrium state. The shear moduli $G'^{ij}_{\dot{\gamma}_s}(\omega)$ and $G''^{ij}_{\dot{\gamma}_s}(\omega)$ are respectively the storage modulus for the elasticity and the loss modulus for the viscosity and are often used to measure the viscoelastic properties of the materials [23; 67; 129; 133]. $G'^{ij}_{\dot{\gamma}_s}(\omega)$ and $G''^{ij}_{\dot{\gamma}_s}(\omega)$ are the Fourier transformations of $\delta\sigma^{ij}(t)$, defined in Eq. (4.4), and $\delta\sigma^{ij}(t)$ can be expressed as $\delta\sigma^{ij}(t) = G'^{ij}_{\dot{\gamma}_s}(\omega)\gamma_0 \sin(\omega t) + G''^{ij}_{\dot{\gamma}_s}(\omega)\gamma_0 \cos(\omega t)$.

$$
\begin{aligned}
G'^{ij}_{\dot{\gamma}_s}(\omega) &= \frac{\omega}{\pi}\int_{-\pi/\omega}^{\pi/\omega} \frac{\delta\sigma^{ij}(t)}{\gamma_0}\sin(\omega t)dt, \\
G''^{ij}_{\dot{\gamma}_s}(\omega) &= \frac{\omega}{\pi}\int_{-\pi/\omega}^{\pi/\omega} \frac{\delta\sigma^{ij}(t)}{\gamma_0}\cos(\omega t)dt.
\end{aligned}
\tag{4.4}
$$

We note that $G'^{ij}_{\dot{\gamma}_s}(\omega)$ and $G''^{ij}_{\dot{\gamma}_s}(\omega)$ depend on the three quantities: ω, γ_0, and $\dot{\gamma}_s$. If the amplitude γ_0 of the oscillating strain is small, and the steady shear flow γ_s is absent, i.e., $\gamma_0 \ll 1$ and $\dot{\gamma}_s = 0$, then $G'^{ij}_{\dot{\gamma}_s}(\omega)$ and $G''^{ij}_{\dot{\gamma}_s}(\omega)$ reduce to the linear shear moduli and depend on only the frequency ω of the oscillating strain. On the other hand, when the amplitude γ_0 gets large, or the steady shear flow $\dot{\gamma}_s$ is present, then the non-linearity arises, so $G'^{ij}_{\dot{\gamma}_s}(\omega)$ and $G''^{ij}_{\dot{\gamma}_s}(\omega)$ becomes the non-linear shear moduli, which depend on not only the frequency ω but also the amplitude γ_0 or the steady shear rate $\dot{\gamma}_s$. In the following sections, we present the results of the shear moduli $G'^{ij}_{\dot{\gamma}_s}(\omega)$ and $G''^{ij}_{\dot{\gamma}_s}(\omega)$.

4.3 Results

4.3.A Mechanical responses in sheared states

We first present the results of mechanical responses in the weakly and strongly sheared states obtained from MD simulations. Figures 4.3 and 4.4 show the results of the shear moduli $G'^{ij}_{\dot{\gamma}_s}$ and $G''^{ij}_{\dot{\gamma}_s}$ at $\dot{\gamma}_s = 10^{-4}$ (weakly sheared state), and figures 4.5 and 4.6 show the results at $\dot{\gamma}_s = 10^{-2}$ (strongly sheared state). The amplitudes γ_0 of the oscillating strain are $\gamma_0 = 0.01$ in Figs. 4.3 and 4.5 and $\gamma_0 = 0.1$ in Figs. 4.4 and 4.6. Notice that the mechanical responses are linear with respect to the oscillating strain at $\gamma_0 = 0.01$ and non-linear at $\gamma_0 = 0.1$. In the same figures, we also show the shear moduli $G'_{\rm eq}$ and $G''_{\rm eq}$ in the equilibrium state to clarify the effects caused by the steady shear flow with $\dot{\gamma}_s = 10^{-4}$ or 10^{-2}. In addition, we plotted two time scales τ_α and τ_β. The time scale τ_α is the α-relaxation time shown in Fig. 4.2(b), and the time scale τ_β is called as the β relaxation time. As is well known, supercooled liquids have these two characteristic time

scales, a slow τ_α and a fast τ_β time component, which can be captured by two-point correlation functions [32]. The value τ_α was influenced by the steady shear, i.e., τ_α is the function of $\dot{\gamma}_s$, as in Fig. 4.2(b), whereas the value τ_β was almost unchanged since τ_β is much short time scale and comparable to the so-called Einstein period.

The shear moduli $G'_{\rm eq}$ and $G''_{\rm eq}$ in Figs. 4.3 and 4.5 show the typical linear viscoelastic behaviors of supercooled liquids [82]. At low frequencies ω, $G''_{\rm eq}$ is larger than $G'_{\rm eq}$, which means liquid-like behaviors. As the frequency ω gets large, $G'_{\rm eq}$ gets larger than $G''_{\rm eq}$, which means solid-like behaviors. The time scale of the crossover from liquid-like to solid-like behaviors is around the α-relaxation time τ_α in the equilibrium state. Notice that τ_α indicated in Figs. 4.3 and 4.5 are the values in the sheared state, not the equilibrium state. At the large amplitude $\gamma_0 = 0.1$ of the oscillating strain (non-linear regime), this time scale of the crossover becomes shorter than that at the small amplitude $\gamma_0 = 0.01$ (linear regime), as we can see from 4.4 or 4.6. Thus, the larger oscillating strain makes the supercooled liquid more liquid-like, which has been also observed in supercooled polymer melt [133; 134].

In the following, we examined the effects due to the steady shear flow with $\dot{\gamma}_s = 10^{-4}$ (weak shear flow) and $\dot{\gamma}_s = 10^{-2}$ (strong shear flow) by comparing $G'^{ij}_{\dot{\gamma}_s}$ and $G''^{ij}_{\dot{\gamma}_s}$ with $G'_{\rm eq}$ and $G''_{\rm eq}$.

(i) Weakly sheared state (Figs. 4.3 and 4.4)

As in Figs. 4.3 and 4.4, although we can recognize the effects due to the steady shear flow at the very low frequencies $\omega < \tau_\alpha^{-1}$, these effects are small. In the whole frequency ω region except for $\omega < \tau_\alpha^{-1}$, all $G'^{ij}_{\dot{\gamma}_s}$ and $G''^{ij}_{\dot{\gamma}_s}$ values almost coincide with $G'_{\rm eq}$ and $G''_{\rm eq}$. Thus, the weak steady shear flow with $\dot{\gamma}_s = 10^{-4}$ makes only small effects on the mechanical responses in the very low frequency region $\omega < \tau_\alpha^{-1}$.

(ii) Strongly sheared state (Figs. 4.5 and 4.6)

As in Figs. 4.5 and 4.6, the strong steady shear flow with $\dot{\gamma}_s = 10^{-2}$ influences the mechanical responses a lot compared to the weak steady shear flow with $\dot{\gamma}_s = 10^{-4}$, as can be physically expected. We can easily recognize the effects due to the steady shear flow at the low frequencies $\omega < \tau_\alpha^{-1}$ for all $G'^{ij}_{\dot{\gamma}_s}$ and $G''^{ij}_{\dot{\gamma}_s}$, whereas at the very high frequencies $\omega > \tau_\beta^{-1}$, these effects are not observed. From Figs. 4.5 and 4.6, we can find two remarkable results. First, two components, xz and yz, of $G'^{ij}_{\dot{\gamma}_s}$ and $G''^{ij}_{\dot{\gamma}_s}$ coincide with each other surprisingly well even at the low frequencies $\omega < \tau_\alpha^{-1}$ where the large effects due to the steady shear flow are observed

(see the upper and lower triangles in Figs. 4.5 and 4.6). Despite the strong steady shear flow, two of the stress responses, $\delta\sigma_{xz}$ to $\delta\gamma_{xz}$ and $\delta\sigma_{yz}$ to $\delta\gamma_{yz}$, are the same. This result demonstrates the isotropic feature of this system. Second, the behaviors of the xy component of $G'^{ij}_{\dot{\gamma}_s}$ and $G''^{ij}_{\dot{\gamma}_s}$ are quite different from those of the xz and yz components (see the circles in Figs. 4.5 and 4.6). The xy component becomes smaller than the xz and yz components at the low frequencies ω. In addition, as ω decreases, the storage modulus $G'^{xy}_{\dot{\gamma}_s}$ decreases much more rapidly than $G'^{xz}_{\dot{\gamma}_s}$ and $G'^{yz}_{\dot{\gamma}_s}$. At low frequencies ω, $G'^{xy}_{\dot{\gamma}_s}$ takes on negative values (data are not shown in Figs. 4.5 and 4.6). Thus, due to the steady shear flow, the mechanical properties of the xy component is notably different from those of the other components. We will demonstrate the origin of this difference between the xy component and the other xz and yz components by means of the constitutive equation later in Sec. 4.3.B. It should be mentioned that similar behaviors of $G'^{xy}_{\dot{\gamma}_s}$ and $G''^{xy}_{\dot{\gamma}_s}$ have also been experimentally observed in polymer solutions under steady shear flows [115; 123], where $G'^{xy}_{\dot{\gamma}_s}$ and $G''^{xy}_{\dot{\gamma}_s}$ are called as parallel moduli.

4.3.B Constitutive equation

We attempted to construct a constitutive equation describing our simulation results and obtained the following equation:

$$\begin{aligned} \boldsymbol{\sigma}_\alpha + \tau_\alpha(\dot{\boldsymbol{\gamma}})\frac{d\boldsymbol{\sigma}_\alpha}{dt} &= \eta_\alpha(\dot{\boldsymbol{\gamma}})\dot{\boldsymbol{\gamma}}, \\ \boldsymbol{\sigma}_\beta + \tau_\beta\frac{d\boldsymbol{\sigma}_\beta}{dt} &= \eta_\beta\dot{\boldsymbol{\gamma}}, \end{aligned} \tag{4.5}$$

where $\boldsymbol{\sigma} = \boldsymbol{\sigma}_\alpha + \boldsymbol{\sigma}_\beta$ is the stress tensor, and $\boldsymbol{\gamma}$ is the strain tensor. $\tau_\alpha(\dot{\boldsymbol{\gamma}})$ and $\eta_\alpha(\dot{\boldsymbol{\gamma}})$ are functions of $\boldsymbol{\gamma}$ as

$$\begin{aligned} \tau_\alpha(\dot{\boldsymbol{\gamma}}) &= \frac{\tau_{\alpha 0}}{1+\mu(\dot{\gamma}^{xy2}+\dot{\gamma}^{xz2}+\dot{\gamma}^{yz2})^{\nu/2}}, \\ \eta_\alpha(\dot{\boldsymbol{\gamma}}) &= \frac{\eta_{\alpha 0}}{1+\mu(\dot{\gamma}^{xy2}+\dot{\gamma}^{xz2}+\dot{\gamma}^{yz2})^{\nu/2}}. \end{aligned} \tag{4.6}$$

It was reported that the linear viscoelastic properties of supercooled liquids can be well described by Maxwell model with two characteristic time scales τ_α and τ_β [82]. In our constitutive equation (4.5), the non-linearity due to the steady shear flow or the large amplitude of the oscillating strain are embedded in the two parameters $\tau_\alpha(\dot{\boldsymbol{\gamma}})$ and $\eta_\alpha(\dot{\boldsymbol{\gamma}})$. The parameters τ_β and η_β remain constant since according to our MD simulation results, the non-linearities are not observed in the region of τ_β and faster than τ_β time scale, as in Figs. 4.3-4.6. We can rewrite the equation regarding $\boldsymbol{\sigma}_\alpha$ in

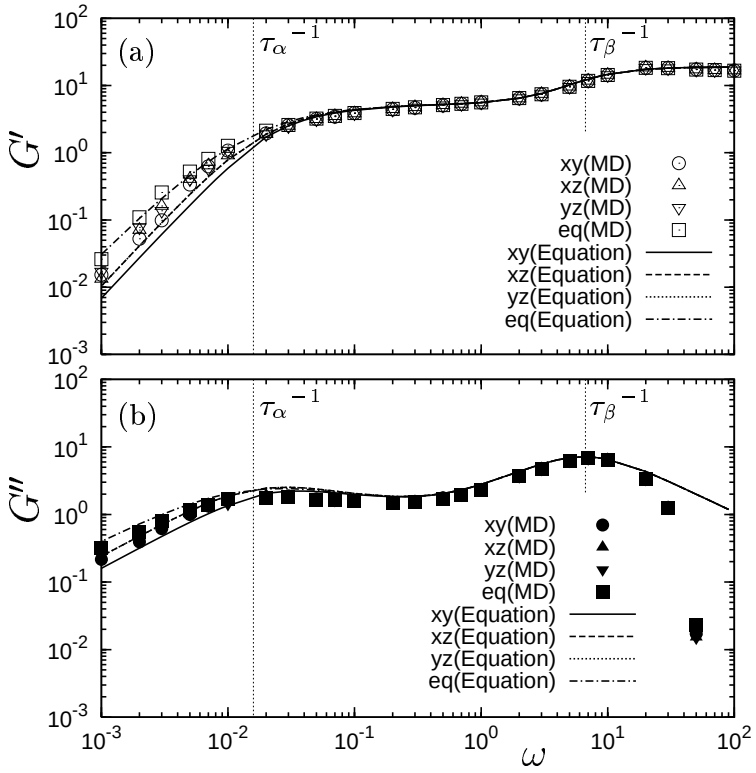

Figure 4.3: The shear moduli (a) $G'^{ij}_{\dot{\gamma}_s}$ and (b) $G''^{ij}_{\dot{\gamma}_s}$ versus ω. $\dot{\gamma}_s = 10^{-4}$ (weakly sheared state) and $\gamma_0 = 10^{-2}$ (linear regime). We also show $G'_{\rm eq}$ and $G''_{\rm eq}$ in the equilibrium state. The symbols and lines represent the results of MD simulations and the constitutive equation (4.5), respectively. The labels "xy", "xz", and "yz" denote $ij = xy$, xz, and yz, respectively, and the label "eq" denotes the equilibrium state.

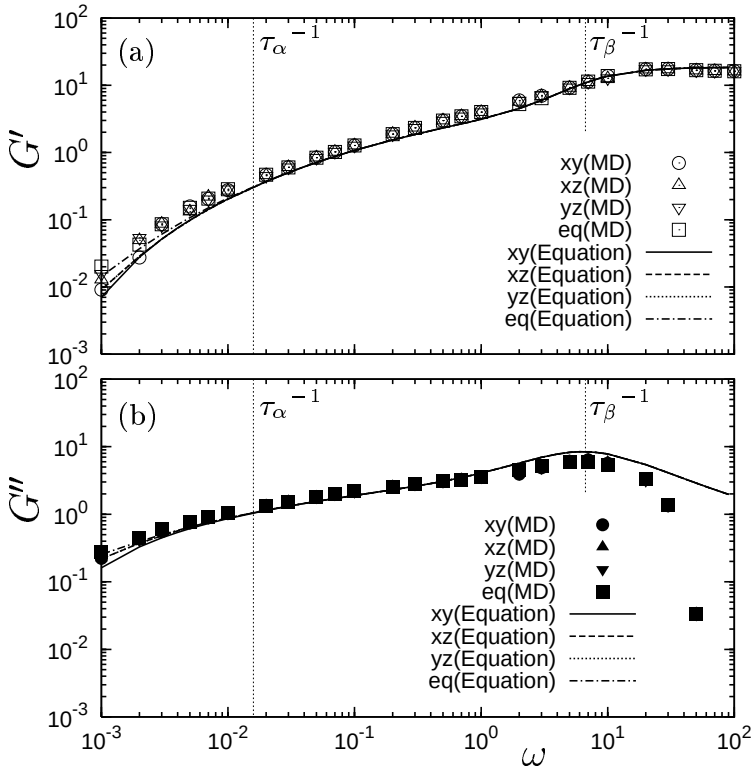

Figure 4.4: The shear moduli (a) $G'^{ij}_{\dot{\gamma}_s}$ and (b) $G''^{ij}_{\dot{\gamma}_s}$ versus ω. $\dot{\gamma}_s = 10^{-4}$ (weakly sheared state) and $\gamma_0 = 10^{-1}$ (non-linear regime). See the caption of Fig. 4.3.

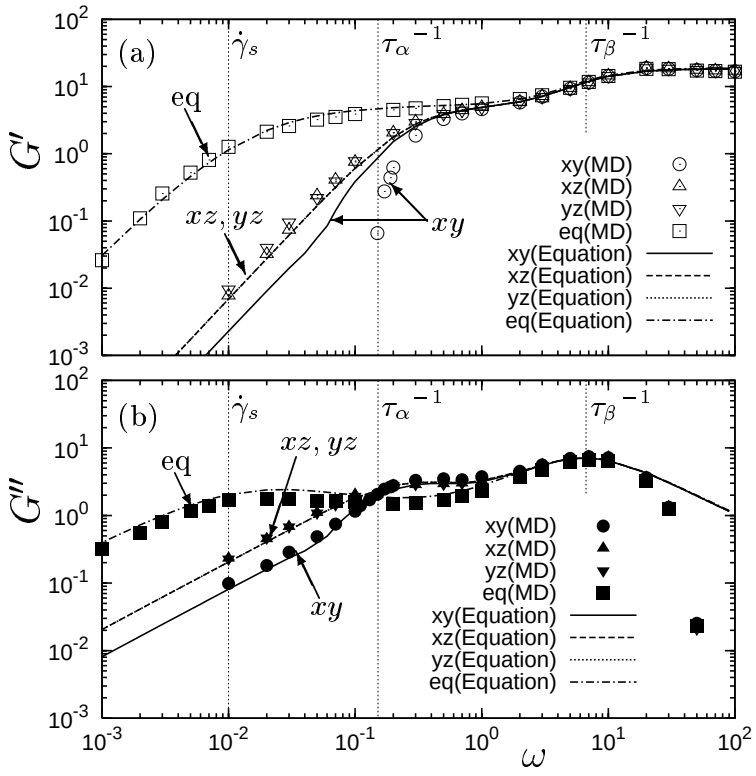

Figure 4.5: The shear moduli (a) $G'^{ij}_{\dot{\gamma}_s}$ and (b) $G''^{ij}_{\dot{\gamma}_s}$ versus ω. $\dot{\gamma}_s = 10^{-2}$ (strongly sheared state) and $\gamma_0 = 10^{-2}$ (linear regime). See the caption of Fig. 4.3.

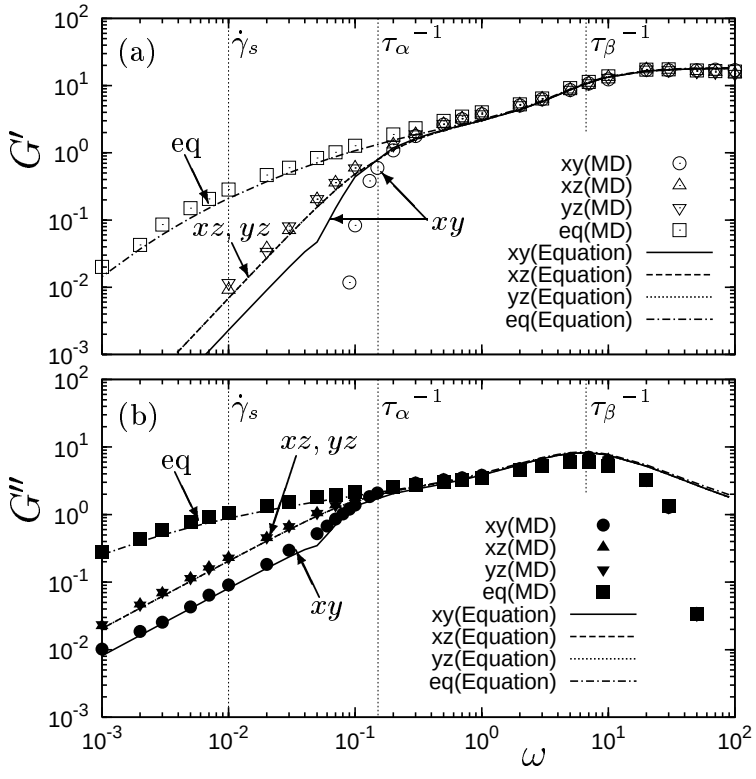

Figure 4.6: The shear moduli (a) $G'^{ij}_{\dot{\gamma}_s}$ and (b) $G''^{ij}_{\dot{\gamma}_s}$ versus ω. $\dot{\gamma}_s = 10^{-2}$ (strongly sheared state) and $\gamma_0 = 10^{-1}$ (non-linear regime). See the caption of Fig. 4.3.

Eq. (4.5) as

$$\mu(\dot{\gamma}^{xy2}+\dot{\gamma}^{xz2}+\dot{\gamma}^{yz2})^{\nu/2}\boldsymbol{\sigma}_\alpha+\boldsymbol{\sigma}_\alpha+\tau_{\alpha 0}\frac{d\boldsymbol{\sigma}_\alpha}{dt}=\eta_{\alpha 0}\dot{\boldsymbol{\gamma}}. \tag{4.7}$$

According to the above equation (4.7), we can consider that the constitutive equation consists of a Maxwell model and a nonlinear term. The non-linear term is the first term of the left-hand side and represents the non-linearity due to the steady shear flow or the large amplitude of the oscillating strain. We stress that this non-linear term is isotropic with respect to the strain tensor $\dot{\boldsymbol{\gamma}}$ and reflects the isotropic feature observed in MD simulations, i.e., the shear responses of the xz and yz components coincide with each other.

The constitutive Eq. (4.5) and Eq. (4.6) have six parameters: $\eta_{\alpha 0}$, $\tau_{\alpha 0}$, μ, ν, η_β, and τ_β. The four parameters, $\eta_{\alpha 0}$, $\tau_{\alpha 0}$, η_β, and τ_β, characterize the linear viscoelastic properties, and the remaining two parameters, μ and ν, characterize the non-linear properties. The four parameters ($\eta_{\alpha 0}$, $\tau_{\alpha 0}$, η_β, and τ_β) can be determined from $G'_{\rm eq}$ and $G''_{\rm eq}$ shown in Figs. 4.3 and 4.5, and we obtained $\eta_{\alpha 0}=430$, $\tau_{\alpha 0}=85$, $\eta_\beta=2.0$, and $\tau_\beta=0.15$. On the other hand, the two parameters (μ and ν) can be determined from the shear-rate dependencies of $\eta(\dot{\gamma}_s)$ and $\tau_\alpha(\dot{\gamma}_s)$ shown in Fig. 4.2. When we consider only a steady shear flow with $\dot{\gamma}_s$, the values η_α and τ_α can be obtained from Eq. (4.6) as

$$\begin{aligned}\tau_\alpha(\dot{\gamma}_s)&=\frac{\tau_{\alpha 0}}{1+\mu\dot{\gamma}_s^\nu},\\ \eta_\alpha(\dot{\gamma}_s)&=\frac{\eta_{\alpha 0}}{1+\mu\dot{\gamma}_s^\nu},\end{aligned} \tag{4.8}$$

which produce the shear-thinning behavior. Thus, we determined the parameters, μ and ν, by fitting Eq. (4.8) to the data of $\eta(\dot{\gamma}_s)$ and $\tau_\alpha(\dot{\gamma}_s)$ in Fig. 4.2, and we obtained $\mu=500$ and $\nu=0.7$. It should be noted that in the case of supercooled liquids, we can consider the shear viscosity as $\eta=\eta_\alpha+\eta_\beta\simeq\eta_\alpha$, since the slower relaxation time is extremely larger than the faster one [32; 47; 74].

Figure 4.3-4.6 also shows the results of the shear moduli $G'^{ij}_{\dot{\gamma}_s}$ and $G''^{ij}_{\dot{\gamma}_s}$ obtained from the constitutive Eq. (4.5) and Eq. (4.6). By comparing the lines (constitutive equation) with the symbols (MD simulation) shown in Fig. 4.3-4.6, we can see that the constitutive equation reflects the results of the MD simulations in both the quiescent equilibrium state and the sheared non-equilibrium state. In addition, the constitutive equation can catch not only the linear responses to the oscillating strains (the amplitude $\gamma_0=0.01$) but also the non-linear stress responses ($\gamma_0=0.1$). We also checked the validity of the constitutive equation at larger amplitudes of $\gamma_0=0.2$, 0.3, and 0.5. We stress that the constitutive Eq. (4.5) and Eq. (4.6) are much simpler than those for typical complex fluids such as polymer solutions [82], and much more interestingly, even in the strongly

sheared state, the mechanical responses can be fit well by this simple constitutive equation.

As mentioned in Sec. 4.3.A, $G'^{xy}_{\dot{\gamma}_s}$ and $G''^{xy}_{\dot{\gamma}_s}$ are much different from the other xz and yz components at the low frequencies ω in the strongly sheared state (see Figs. 4.5 and 4.6). We examined this difference between the xy component and the other xz and yz components by using the constitutive Eq. (4.5) and Eq. (4.6). Note that at the low frequencies, the stress tensor $\boldsymbol{\sigma}$ can be written as $\boldsymbol{\sigma} = \boldsymbol{\sigma}_\alpha + \boldsymbol{\sigma}_\beta \simeq \boldsymbol{\sigma}_\alpha$, so in the following, we consider $\boldsymbol{\sigma}_\alpha$ as the stress tensor $\boldsymbol{\sigma}$. To reveal the effects due to the steady shear flow, we analyzed the constitutive equation with the condition $\gamma_0\omega \ll \dot{\gamma}_s$. This condition, $\gamma_0\omega \ll \dot{\gamma}_s$, means that the shear rate of the steady shear flow is much larger than that of the oscillating strain and holds well at the low frequencies ω. In result, the following two equations were obtained: Eq. (4.9) for the xy component and Eq. (4.10) for the xz and yz components.

$$\mu\dot{\gamma}_s{}^{\nu}\delta\sigma^{xy} + \delta\sigma^{xy} + \tau_{\alpha 0}\frac{d\delta\sigma^{xy}}{dt} = \eta_0\delta\dot{\gamma}^{xy} - \mu\nu\dot{\gamma}_s{}^{\nu-1}\sigma_s\delta\dot{\gamma}^{xy}. \tag{4.9}$$

$$\mu\dot{\gamma}_s{}^{\nu}\delta\sigma^{ij} + \delta\sigma^{ij} + \tau_{\alpha 0}\frac{d\delta\sigma^{ij}}{dt} = \eta_0\delta\dot{\gamma}^{ij}, \qquad (ij = xz,\ yz). \tag{4.10}$$

Here, $\delta\dot{\gamma}^{ij} = \gamma_0\omega\cos\omega t$. Note that the equations for the xz and yz components are exactly identical, which arises from constitutive equation being isotropic with respect to the strain tensor $\boldsymbol{\gamma}$. By comparing Eqs. (4.9) and (4.10), we see that the difference between the xy component and the other xz and yz components originates from the second term of the right-hand side of Eq. (4.9), i.e., the "$\dot{\gamma}_s^{\nu}\delta\dot{\gamma}^{xy}$" term. This term arises from the coupling between the driving shear flow $\dot{\gamma}_s$ and the oscillating strain $\delta\dot{\gamma}^{xy}$. In the xz and yz components, such a coupling does not appear because the driving shear flow and the oscillating strain are different components. However, in the xy component, the driving shear flow $\dot{\gamma}_s$ and the oscillating strain $\delta\dot{\gamma}^{xy}$ are the same components, and the coupling term "$\dot{\gamma}_s^{\nu}\delta\dot{\gamma}^{xy}$" arises, which is the origin of the difference between the xy component and the other xz and yz components.

As we mentioned, there are some studies investigating the mechanical responses of polymer solutions under a steady shear flow [84; 115; 121; 123], where the responses $\delta\sigma^{xy}$ to $\delta\gamma^{xy}$ and $\delta\sigma^{yz}$ to $\delta\gamma^{yz}$ have been examined. Note that in their studies, the responses $\delta\sigma^{xy}$ to $\delta\gamma^{xy}$ and $\delta\sigma^{yz}$ to $\delta\gamma^{yz}$ are called as the parallel superposition and orthogonal superposition, respectively. It was reported that the steady shear flow can make the effect called as the convective constraint release effect [115] or can induce the anisotropic mobility [121], which both accelerate the relaxation time of polymer dynamics. These are similar effects as that made by the non-linear term of the constitutive Eq.

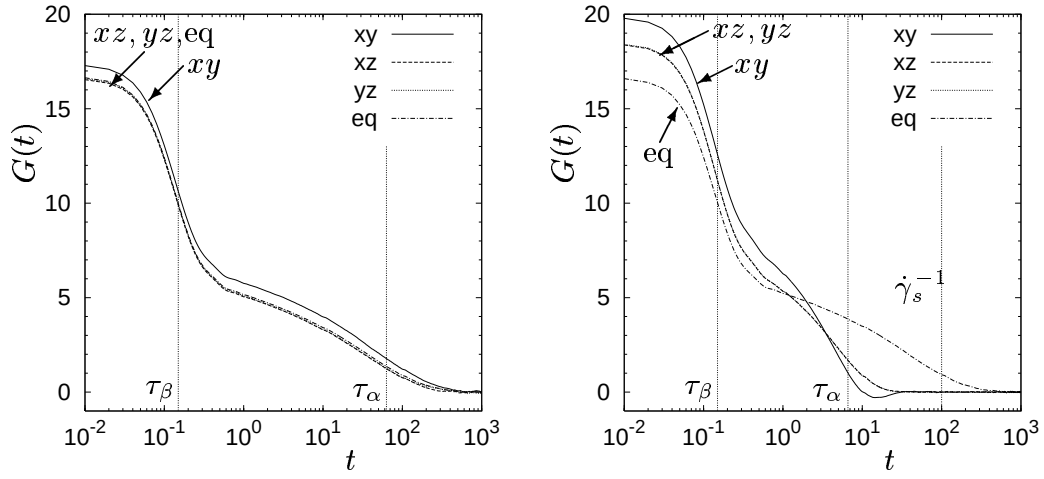

(a) $\dot{\gamma}_s = 10^{-4}$ (b) $\dot{\gamma}_s = 10^{-2}$

Figure 4.7: The shear stress correlation function $G^{ij}_{\dot{\gamma}_s}$. (a) $\dot{\gamma}_s = 10^{-4}$ (weakly sheared state) and (b) $\dot{\gamma}_s = 10^{-2}$ (strongly sheared state). We also show $G_{\rm eq}$ in the equilibrium state. The labels "xy", "xz", and "yz" denote $ij = xy$, xz, and yz, respectively, and the label "eq" denotes the equilibrium state.

(4.5) and Eq. (4.6) in the way that they all accelerate the relaxation times. However, in polymer solutions, the origin of the difference between the xy component and the yz component is still not clear. Furthermore, to our best knowledge, there are no studies investigating mechanical responses of polymer solutions for the xz component. It can be expected that the mechanical responses of polymer solutions in the xz and yz components are different on the contrary to glassy systems exhibiting the surprisingly same responses.

4.3.C Stress fluctuations in sheared states

We next examined the shear stress fluctuations in the sheared states. We calculated the correlation functions, $G^{xy}_{\dot{\gamma}_s}$, $G^{xz}_{\dot{\gamma}_s}$, and $G^{yz}_{\dot{\gamma}_s}$, of the shear stress fluctuations, defined as

$$G^{ij}_{\dot{\gamma}_s}(t) = \frac{V}{T}\left\langle \delta\sigma^{ij}(t)\delta\sigma^{ij}(0)\right\rangle_{\dot{\gamma}_s}, \qquad (ij = xy,\ xz,\ yz), \tag{4.11}$$

where $\delta\sigma^{ij}$ represents the shear stress fluctuations in the ij component of the stress tensor $\boldsymbol{\sigma}$, and $\langle\rangle_{\dot{\gamma}_s}$ denotes the ensemble average in the sheared non-equilibrium state.

Figure 4.7 shows the functions $G^{xy}_{\dot{\gamma}_s}$, $G^{xz}_{\dot{\gamma}_s}$, and $G^{yz}_{\dot{\gamma}_s}$ for $\dot{\gamma}_s = 10^{-4}$ (weakly sheared state) in (a) and $\dot{\gamma}_s = 10^{-2}$ (strongly sheared state) in (b). In the same figures, the function $G_{\rm eq}$ in the equilibrium state is also plotted.

(i) Weakly sheared state (Fig. 4.7(a))

As in Fig. 4.7(a), while we can recognize that $G^{xy}_{\dot{\gamma}_s}$ behaves a little differently from $G_{\rm eq}$, $G^{xz}_{\dot{\gamma}_s}$ and $G^{yz}_{\dot{\gamma}_s}$ coincide with $G_{\rm eq}$. Thus, like the mechanical responses shown in Figs. 4.3 and 4.4, the shear stress fluctuations are also caused only small effects on by the weak steady shear flow with $\dot{\gamma}_s = 10^{-4}$.

(ii) Strongly sheared state (Fig. 4.7(b))

We can easily recognize that all $G^{ij}_{\dot{\gamma}_s}$ relax rapidly compared to $G_{\rm eq}$ due to the steady shear flow, as in Fig. 4.7(b). The strong steady shear flow with $\dot{\gamma}_s = 10^{-2}$ causes large effects on the shear stress fluctuations as well as the mechanical responses. It should be noted that even for the small times $t < \tau_\beta$, all $G^{ij}_{\dot{\gamma}_s}$ values differ from $G_{\rm eq}$, which means that the strong steady shear flow with $\dot{\gamma}_s = 10^{-2}$ affects the fluctuations even at $t < \tau_\beta$, time scales much smaller than $\dot{\gamma}_s^{-1} = 10^2$. A similar result has been observed in sheared foam [100]. This trend is different than those of the responses $G'^{ij}_{\dot{\gamma}_s}$ and $G''^{ij}_{\dot{\gamma}_s}$ shown in Figs. 4.5 and 4.6, where at short time scales ($\omega > \tau_\beta^{-1}$), all $G'^{ij}_{\dot{\gamma}_s}$ and $G''^{ij}_{\dot{\gamma}_s}$ values coincide with $G'_{\rm eq}$ and $G''_{\rm eq}$, i.e., the effects due to the steady shear flow are not observed. Fig. 4.7(b) also shows that $G^{xz}_{\dot{\gamma}_s}$ and $G^{yz}_{\dot{\gamma}_s}$ are identical, while $G^{xy}_{\dot{\gamma}_s}$ behaves quite differently and has even negative values. This situation is also observed for the responses $G'^{ij}_{\dot{\gamma}_s}$ and $G''^{ij}_{\dot{\gamma}_s}$ in Figs. 4.5 and 4.6. The coincidence of the values of $G^{xz}_{\dot{\gamma}_s}$ and $G^{yz}_{\dot{\gamma}_s}$ demonstrates isotropic fluctuations, and such isotropic fluctuations have been also observed in the two-point correlation functions and the mean square displacement [17; 90; 131]. In contrast, the different behavior of $G^{xy}_{\dot{\gamma}_s}$ demonstrates an anisotropy, which has also been detected in the four-point correlation functions [46]. It has been reported that $G^{xy}_{\dot{\gamma}_s}$ does not decay monotonically and has negative values in sheared foam [100], which is consistent with our result.

4.3.D Violation of fluctuation-dissipation theorem

Finally, we investigated the relations between the response functions and the correlation functions, which are of great interest and importance [7; 8; 13; 14; 26; 54; 56; 78; 100; 116; 121; 135]. When we use $G'^{ij}_{\dot{\gamma}_s}$ and $G''^{ij}_{\dot{\gamma}_s}$ as the response functions, the associated correlation function is the Fourier transformation of $G^{ij}_{\dot{\gamma}_s}$, defined as

$$
\begin{aligned}
G'^{ij}_{{\rm cor},\dot{\gamma}_s}(\omega) &= \omega \int_0^\infty G^{ij}_{\dot{\gamma}_s}(t)\sin(\omega t)dt, \\
G''^{ij}_{{\rm cor},\dot{\gamma}_s}(\omega) &= \omega \int_0^\infty G^{ij}_{\dot{\gamma}_s}(t)\cos(\omega t)dt,
\end{aligned}
\tag{4.12}
$$

where the subscript "cor" denotes the correlation function. We note that the response functions have to be $G'^{ij}_{\dot{\gamma}_s}$ and $G''^{ij}_{\dot{\gamma}_s}$ at the small amplitude $\gamma_0 = 0.01$ of the oscillating strain, i.e., the linear responses with respect to the oscillating strain.

Figures 4.8 and 4.9 show the correlation functions $G'^{ij}_{\mathrm{cor},\dot{\gamma}_s}$ and $G''^{ij}_{\mathrm{cor},\dot{\gamma}_s}$ with the response functions $G'^{ij}_{\dot{\gamma}_s}$ and $G''^{ij}_{\dot{\gamma}_s}$ at $\dot{\gamma}_s = 10^{-4}$ (weakly sheared state) and $\dot{\gamma}_s = 10^{-2}$ (strongly sheared state), respectively. The correlation and response functions in the equilibrium state are also shown in the same figures. As well demonstrated in Figs. 4.8 and 4.9, we can see that the response function and the correlation function coincide with each other in the equilibrium state, which means that the FDT holds. In contrast, as in Figs. 4.8 and 4.9, the response function and the correlation function do not coincide in the non-equilibrium sheared states, and therefore, the FDT is violated. The violation is much large in the strong sheared case (see Fig. 4.9). Notice that the FDT is violated even at the high frequencies $\omega > \tau_\beta^{-1}$, because the correlation functions of the shear stress fluctuations behave differently from the equilibrium one even at $t < \tau_\beta$ as shown in Fig. 4.7 although the responses in the sheared state coincide with the equilibrium one as shown in Fig. 4.3 and 4.5. The violation of the FDT is physically interpreted as entropy production [54; 116], a steady-state probability current [26], or other related physical quantities. Recent works have strived to provide a unifying framework for this phenomenon [7; 8].

To examine the concept of an effective temperature [13; 14; 56; 78; 100; 135], we defined the frequency-dependent effective temperatures T'_{eff} and T''_{eff} as

$$\begin{aligned} \frac{T'_{\mathrm{eff}}(\omega)}{T} &= \frac{G'^{ij}_{\mathrm{cor},\dot{\gamma}_s}(\omega)}{G'^{ij}_{\dot{\gamma}_s}(\omega)}, \\ \frac{T''_{\mathrm{eff}}(\omega)}{T} &= \frac{G''^{ij}_{\mathrm{cor},\dot{\gamma}_s}(\omega)}{G''^{ij}_{\dot{\gamma}_s}(\omega)}. \end{aligned} \tag{4.13}$$

Note that the effective temperatures T'_{eff} and T''_{eff} are defined from different observables, the storage modulus and the loss modulus, respectively. Figure 4.10 and 4.11 show the frequency ω dependencies of T'_{eff} and T''_{eff} at $\dot{\gamma}_s = 10^{-4}$ (weakly sheared state) and $\dot{\gamma}_s = 10^{-2}$ (strongly sheared state), respectively. In the equilibrium state, T'_{eff} and T''_{eff} are exactly the same as the temperature $T = 0.306$ for all frequencies ω, as is well demonstrated in Figs. 4.10 and 4.11. Thus, the temperature T exactly relates the response function to the correlation function. However, in the non-equilibrium state, both T'_{eff} and T''_{eff} differ from $T = 0.306$. As in Fig. 4.11, in the strong sheared case, T'_{eff} and T''_{eff} differ largely from $T = 0.306$. If the concept of an effective temperature

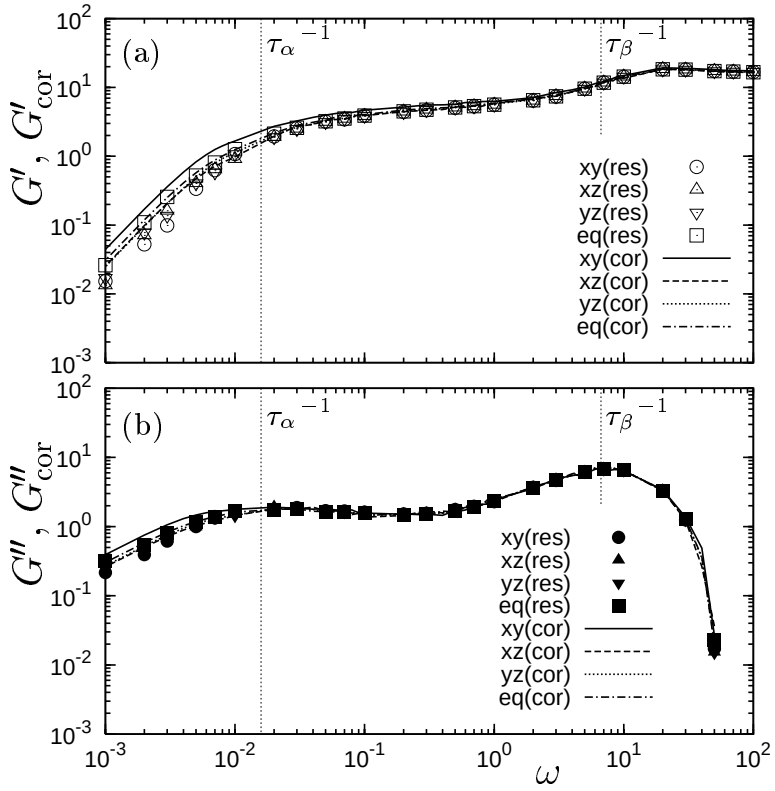

Figure 4.8: The response and correlation functions (a) $G'^{ij}_{\dot\gamma_s}$ and $G'^{ij}_{{\rm cor},\dot\gamma_s}$ and (b) $G''^{ij}_{\dot\gamma_s}$ and $G''^{ij}_{{\rm cor},\dot\gamma_s}$ versus ω. $\dot\gamma_s = 10^{-4}$ (weakly sheared state). We also show the functions in the equilibrium state. The symbols and lines represent the response functions and the correlation functions, respectively. The labels "res" and "cor" correspond to the response function and the correlation function, respectively. See also the caption of Fig. 4.3 for the labels "xy", "xz", "yz", and "eq".

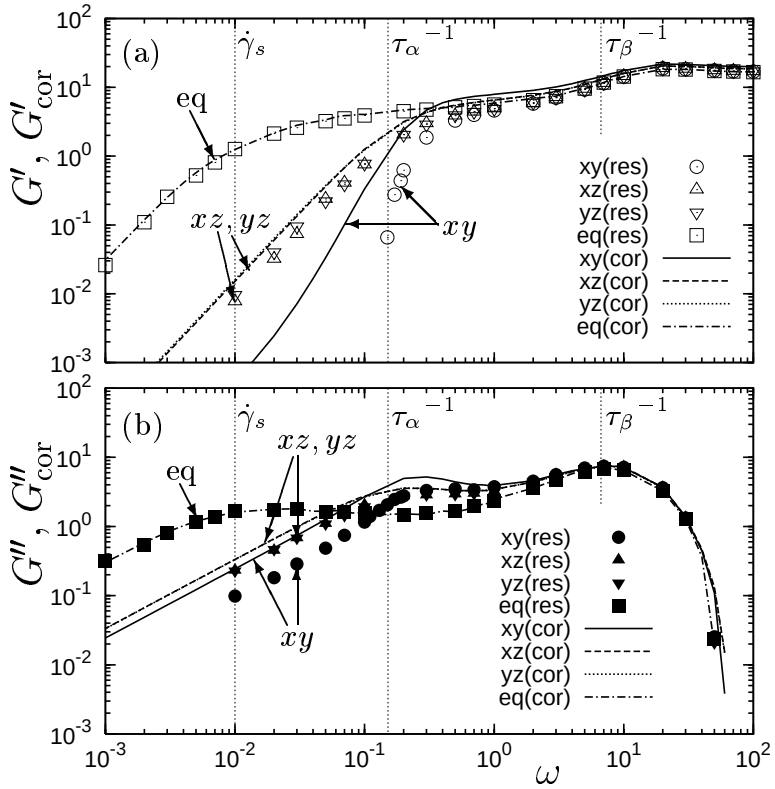

Figure 4.9: The response and correlation functions (a) $G'^{ij}_{\dot\gamma_s}$ and $G'^{ij}_{{\rm cor},\dot\gamma_s}$ and (b) $G''^{ij}_{\dot\gamma_s}$ and $G''^{ij}_{{\rm cor},\dot\gamma_s}$ versus ω. $\dot\gamma_s = 10^{-2}$ (strongly sheared state). See the caption of Fig. 4.8.

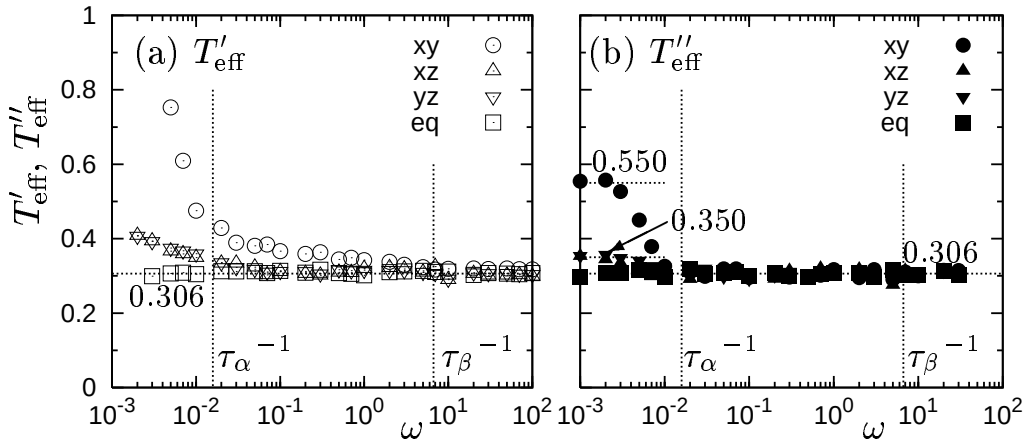

Figure 4.10: The effective temperatures (a) $T'_{\rm eff}$ and (b) $T''_{\rm eff}$ versus ω. $\dot{\gamma}_s = 10^{-4}$ (weakly sheared state).

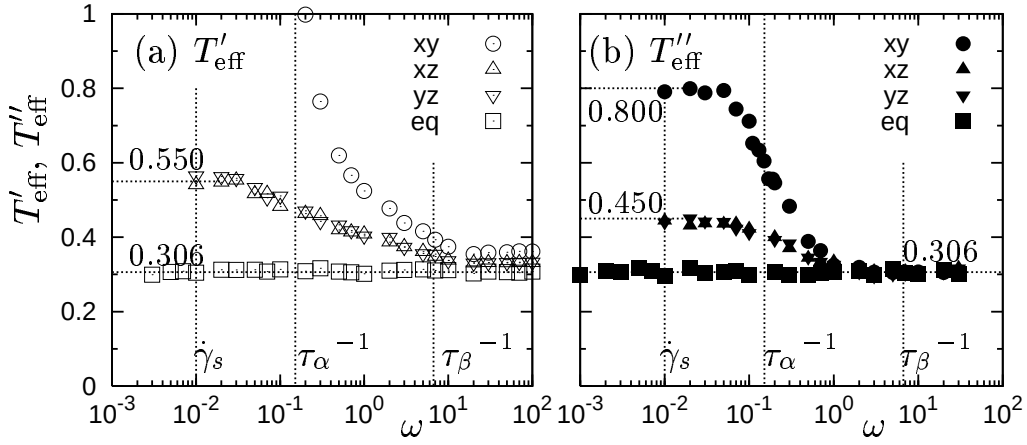

Figure 4.11: The effective temperatures (a) $T'_{\rm eff}$ and (b) $T''_{\rm eff}$ versus ω. $\dot{\gamma}_s = 10^{-2}$ (strongly sheared state).

is valid, then, at low frequencies ω (long time scales), $T'_{\rm eff}$ and $T''_{\rm eff}$ should coincide with each other and have the same value for all components $ij = xy,\ xz$, and yz, i.e., one scalar quantity should relate the response function and the correlation function of any observable and any component. However, as shown in Figs. 4.10 and 4.11, $T'_{\rm eff}$ and $T''_{\rm eff}$ differ from each other and have different values between components. Note that $T'_{\rm eff}$ of the xy component has negative values at low ω because of the negative $G'^{ij}_{\dot{\gamma}_s}$ (data are not shown in Figs. 4.10 and 4.11). This result indicates that the use of only one effective temperature (one scalar quantity) cannot completely characterize the relationship between the response functions and the correlation functions and calls for further improvement and modification to the concept of an effective temperature. For the supercooled liquid, it is notable that the effective temperatures $T'_{\rm eff}$ and $T''_{\rm eff}$ have the same values for the xz

and yz components over all ω. This feature is considered as a characteristic of glassy systems. In general, the effective temperature may depend on the direction or the component of the observable, which has recently been observed in sheared colloidal suspensions [135].

In addition, the behaviors of $T'_{\rm eff}$ and $T''_{\rm eff}$ notably differ from each other over the entire domain of ω. $T''_{\rm eff}$ coincides with $T = 0.306$ at high $\omega > \tau_\beta^{-1}$, and as ω decreases, $T''_{\rm eff}$ starts to deviate from $T = 0.306$ near $\omega = \tau_\alpha^{-1}$ and approaches higher values: 0.350 for the xz and yz components and 0.550 for the xy component in the weakly sheared case (see Fig. 4.10) and 0.450 for the xz and yz components and 0.800 for the xy component in the strongly sheared case (see Fig. 4.11). This behavior of $T''_{\rm eff}$ is consistent with previous results [13; 14; 78; 135], i.e., the effective temperature can be equivalent to the bath temperature at short times (high ω) and a higher temperature at long times (low ω). However, $T'_{\rm eff}$ is slightly higher than T and does not coincide with T even at high $\omega > \tau_\beta^{-1}$. As ω decreases, $T'_{\rm eff}$ begins to increase near $\omega = \tau_\beta^{-1}$, a much shorter time scale compared with $\omega = \tau_\alpha^{-1}$. In addition, $T'_{\rm eff}$ for the xy component does not approach a positive value. These behaviors of $T'_{\rm eff}$ are clearly observed in the strongly sheared case (Fig. 4.11(a)). In the weakly sheared case (Fig. 4.10(a)), $T'_{\rm eff}$ of the xy component behaves in the manner described above, whereas $T'_{\rm eff}$ for the xz and yz components behave like $T''_{\rm eff}$. These results for $T'_{\rm eff}$ are inconsistent with previous results [13; 14; 78; 135]. Therefore, the effective temperature measured in previous works [13; 14; 78; 135] may be physically similar to $T''_{\rm eff}$ but different from $T'_{\rm eff}$.

In order to examine whether the effective temperature measured in previous works [13; 14; 78; 135] is quantitatively same as $T''_{\rm eff}$ or not, we investigated the mechanical response to a small constant shear strain. At time $t = 0$, the constant small shear strain $\delta\gamma^{ij} = 0.01$ was applied on the sheared supercooled liquid. Note that the response is linear with respect to the shear strain $\delta\gamma^{ij} = 0.01$. We calculated the response $\delta\sigma^{ij}$ by using MD simulation, and then the susceptibility was obtained as

$$\chi^{ij}_{\dot\gamma_s}(t) = \frac{\left\langle \delta\sigma^{ij}(t) - \delta\sigma^{ij}(0) \right\rangle_{\dot\gamma_s}}{\delta\gamma^{ij}}, \tag{4.14}$$

where $\langle\rangle_{\dot\gamma_s}$ denotes the ensemble average in the sheared non-equilibrium state. In the equilibrium situation, the following relation (4.15) holds between the susceptibility and the correlation function.

$$\chi_{\rm eq}(t) = \frac{1}{T}(G_{\rm eq}(0) - G_{\rm eq}(t)). \tag{4.15}$$

Eq. (4.15) indicates that the temperature T can be obtained as (minus) the inverse slope of the susceptibility-correlation function plot. On the other hand, in the non-equilibrium situation, the

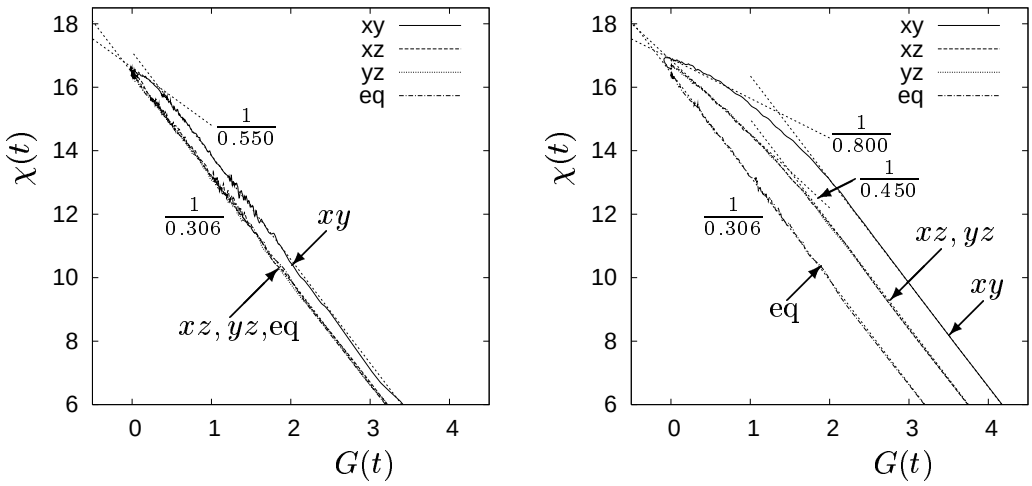

(a) $\dot{\gamma}_s = 10^{-4}$ (b) $\dot{\gamma}_s = 10^{-2}$

Figure 4.12: The susceptibility $\chi^{ij}_{\dot{\gamma}_s}(t)$ versus the shear stress correlation function $G^{ij}_{\dot{\gamma}_s}(t)$. (a) $\dot{\gamma}_s = 10^{-4}$ (weakly sheared state) and (b) $\dot{\gamma}_s = 10^{-2}$ (strongly sheared state). We also show $\chi_{\rm eq}(t)$ versus $G_{\rm eq}(t)$ in the equilibrium state. The labels "xy", "xz", and "yz" denote $ij = xy$, xz, and yz, respectively, and the label "eq" denotes the equilibrium state. In the figures, the slopes are also written.

effective temperature is defined as the inverse slope of the susceptibility-correlation function plot for long times [13; 14; 78; 135], as in Eq. (4.16).

$$\chi^{ij}_{\dot{\gamma}_s}(t) = \frac{1}{T_{\rm eff}}(G^{ij}_{\dot{\gamma}_s}(0) - G^{ij}_{\dot{\gamma}_s}(t)). \tag{4.16}$$

Figure 4.12 shows the susceptibility-correlation function plot for $ij = xy$, xz, and yz components in the sheared state. In the same figure, the susceptibility-correlation function plot in the equilibrium state is also plotted. In the equilibrium state, the inverse slope is exactly $T = 0.306$ in the whole region. On the contrary, in the sheared non-equilibrium state, the inverse slopes for long times take values higher than $T = 0.306$, and these values coincide well with $T''_{\rm eff}(\omega)$ at low frequencies: 0.550 for the xy component in the weakly sheared case (see Fig. 4.12(a)) and 0.450 for the xz and yz components and 0.800 for the xy component in the strongly sheared case (see Fig. 4.12(b)). Note that in the weakly sheared case, the inverse slopes for the xz and yz components can be 0.350 ($T''_{\rm eff}(\omega)$ at low ω), although we cannot distinguish such slope numerically. Thus, we can conclude that the effective temperature $T_{\rm eff}$ used in previous works [13; 14; 78; 135] and $T''_{\rm eff}$ are quantitatively same. The effective temperatures $T_{\rm eff}$ and $T''_{\rm eff}$ can be mathematically connected because responses to a small constant strain and an oscillating strain can be connected by the Fourier transformation.

4.4 Conclusion

We examined the mechanical responses of a supercooled liquid in sheared states. We first applied a steady shear flow to drive the supercooled liquid into a non-equilibrium state. Then an oscillating strain was applied on the non-equilibrium supercooled liquid. Both the linear responses and the non-linear responses to the oscillating strains were investigated. As can be expected, the weak steady shear flow caused small effects on the mechanical responses to the oscillating strains, whereas the strong steady shear flow caused large effects on the mechanical responses. For the components differing from that of the driving shear flow, the same responses were obtained, which demonstrates the isotropic feature of supercooled liquids. In contrast, for the same component as that of the driving shear flow, the responses are quite different from those of the other components. This difference arises from the coupling between the steady shear flow and the oscillating shear strain. We constructed the constitutive Eq. (4.5) and Eq. (4.6) for supercooled liquids and demonstrated that even in the strongly sheared state or even for the non-linear responses, the mechanical responses can be fit well by these equations. The constitutive equation is much simpler than those for typical complex fluids such as polymer solutions [82], which demonstrate much simple mechanical properties of supercooled liquids.

We next examined the shear stress fluctuations in the sheared non-equilibrium states. As are the mechanical responses, the shear stress fluctuations are caused large effects on by the strong steady shear flow, whereas the weak steady shear flow causes small effects. Similar to mechanical responses, for the components differing from that of the driving shear flow, the same correlations of the shear stress fluctuations were observed. This result demonstrates the isotropic fluctuations of this system, which have been also observed in two-point correlation functions or mean square displacements [17; 90; 131]. In contrast, for the same component as that of the driving shear flow, the correlations are quite different from those of the other components, which demonstrates the anisotropic fluctuations of the system. Anisotropic fluctuations have been also found in four-point correlation function [46].

Finally, we examined a violation of the FDT in the sheared states [7; 8; 26; 54; 116; 121]. While the FDT holds in the equilibrium state, the FDT are violated in the sheared non-equilibrium states. Especially the strong shear flow makes the FDT largely violated. We explored the validity of the concept of an effective temperature [13; 14; 56; 78; 100; 135]. We defined two frequency-dependent

effective temperatures based on the storage modulus and the loss modulus and found that the use of only one effective temperature cannot completely characterize the relationship between the response functions and the correlation functions. The effective temperature based on the loss modulus is quantitatively same as that measured in previous works [13; 14; 78; 135].

As we investigated in this work, supercooled liquids have simple non-equilibrium properties that are not observed in typical complex fluids such as polymer solutions [82; 84; 115; 123]. Owing to such simplicity, supercooled liquids (or glassy systems) composed of spherical or low-molecular-weight molecules may be excellent materials for investigating non-equilibrium statistical mechanics.

Chapter 5

Acoustic properties of a supercooled liquid

5.1 Introduction

The dynamics of supercooled liquids, including the slowing down, the two step relaxation, the heterogeneous dynamics, and so on, have been the focus of interest for a long time [32; 37]. One of the important dynamical properties is the sound wave propagation [53; 63], which is the collective motion of atoms. Whereas the longitudinal sound waves can propagate in both solids and liquids, the transverse sound waves can propagate in solids but not in liquids. One of the characteristics of solids is that they can support the transverse modes, which phenomenologically leads to a finite shear modulus at zero frequency. However, at sufficiently short wavelengths and high frequencies, liquids can also support propagating transverse modes for considerable distances before decaying. This has been experimentally demonstrated for many liquids [55; 66]. Even simple monatomic liquids can support propagating elastic transverse modes with atomic-scale wavelengths.

In contrast to normal liquids, supercooled liquids sustain the transverse sound waves even at long wavelengths and low frequencies due to the viscoelastic property. As well known, supercooled liquids exhibit the viscoelastic property, i.e., not only liquid-like viscous nature but also solid-like elastic nature, similar to complex fluids such as polymer solutions [82]. As the temperature decreases, the structural relaxation time becomes dramatically large, which indicates an increase in the solid-like nature. The large structural relaxation time supports the transverse sound waves to propagate in the supercooled liquids. In fact, several researches estimated the length scale l_t, called as the hydrodynamic length [95], as the largest wavelength that the transverse modes can exist in liquids by means of molecular-dynamics (MD) simulation [95] and mode-coupling theory (MCT) [2; 29; 30], and it was reported that the value l_t increases dramatically with decreasing the temperature and becomes extremely large in the supercooled state, which means that the transverse sound waves can propagate even at long wavelengths and low frequencies.

It is possible to predict the behavior of the sound waves propagating in the materials by means of the continuum mechanics [38; 53; 109; 124]. This approach, however, is difficult to perform because the appropriate constitutive equation is necessary to characterize the mechanical properties of the

materials. In our previous study [94] (Chapter 4), we successfully constructed a two-mode Maxwell model as the constitutive equation for the supercooled liquids. This constitutive equation can describe the shear stress responses of the supercooled liquid quite well in not only the quiescent equilibrium state but also the sheared non-equilibrium state (see Chapter 4). We are therefore able to examine the behavior of the transverse sound wave by means of the continuum mechanics with this constitutive equation. In this work, we attempted to explain physically the behavior of the transverse sound wave in the framework of the continuum mechanics. The most recent works [47; 48] found out that the shear viscosity of the supercooled liquid depends notably on the wavenumber (the distance scale). This result physically demonstrated the spatial nonlocality of the viscous transport, which is also observed in complex fluids such as entangled polymer solutions [43; 44; 45]. We expect that the effect due to the lengthscale dependence of the viscosity can be observed in the propagation of the transverse sound waves.

In the present study, we examined the behavior of the transverse sound wave in the supercooled liquid by means of MD simulations. The dispersion relation and the sound attenuation time constant were estimated by calculating the transverse current spectrum. To interpret the simulation results physically, we also investigated the propagation of the transverse sound wave by using the continuum mechanics with the constitutive equation obtained in the previous study [93] (Chapter 4). The aim of the present study is to explain the behavior of the transverse sound wave in the framework of the continuum mechanics. We also extended the constitutive equation to the finite wavenumber case by using the wavenumber dependent viscosity and shear modulus [38; 53]. This extension allowed us to describe the sound waves with short wavelengths and high frequencies.

The paper is organized as follows. In Sec. 5.2, we briefly review our MD simulation. We also define the density and current correlation functions and their Fourier transforms in this section. In Sec. 5.3, we present our results. We first present simulation results of the transverse sound waves in the quiescent equilibrium and sheared non-equilibrium sates, and then the predictions of continuum mechanics are presented. In Sec. 5.4, we summarize our result.

5.2 Simulation model and correlation functions of density and current

5.2.A Simulation model

We performed MD simulations in three dimensions. Our simulation model is a mixture of two different size atomic species, 1 and 2, with $N_1 = 50,000$ and $N_2 = 50,000$ particles. The particles interact via the soft-sphere potential $v_{ab}(r) = \epsilon(\sigma_{ab}/r)^{12}$ with $\sigma_{ab} = (\sigma_a + \sigma_b)/2$, where r is the distance between two particles, σ_a is the particle size, and $a, b \in 1, 2$. The interaction was truncated at $r = 3\sigma_{ab}$. We took the mass ratio to be $m_2/m_1 = 2$ and the size ratio to be $\sigma_2/\sigma_1 = 1.2$. This diameter ratio avoided system crystallization and ensured that an amorphous supercooled state formed at low temperatures [89]. In this work, we measured space, time, and temperature by σ_1, $\tau_0 = (m_1\sigma_1^2/\epsilon)^{1/2}$, and ϵ/k_B, respectively. The particle density was fixed at a value of $\rho = (N_1 + N_2)/V = 0.8$, where the system length was 50.0. The temperature was set to be $T = 0.772,\ 0.306,\ 0.289$, and 0.267. The freezing point of the corresponding one-component model is around $T = 0.772$ ($\Gamma_{\text{eff}} = 1.15$) [89]. Here, Γ_{eff} is a single parameter characterizing this soft-sphere liquid model, called as the effective density. At $T = 0.267$ ($\Gamma_{\text{eff}} = 1.50$), the system is in a highly supercooled state. Simulations were carried out in not only the quiescent equilibrium state but also the sheared non-equilibrium state. In the equilibrium state, we integrated the Newtonian equations of motion with the periodic boundary condition. On the other hand, in the sheared state, we integrated the so-called SLLOD equations of motion with the Lees-Edwards periodic boundary condition [39]. The Lees-Edwards periodic boundary condition maintained a steady shear flow. We set the x axis and the y axis along the flow direction and the velocity gradient direction of the steady shear flow, respectively. The mean velocity profile is $\langle \boldsymbol{v} \rangle = \dot{\gamma} y \boldsymbol{e}_x$, where $\boldsymbol{e}_x$ is the unit vector in x direction. The temperature was kept at a desired value using a Gaussian constraint thermostat in the sheared non-equilibrium state [39]. The details of this simulation model are found in previous works [75; 90; 131].

5.2.B Density and current correlation functions

In this section, we consider only the sheared situation with the shear rate $\dot{\gamma}$. However, when the shear rate is set to be $\dot{\gamma} = 0$, then the situation directly reduces to the equilibrium situation. The

mass density and the associate mass current [53] are defined as

$$\begin{aligned}\hat{\rho}(\boldsymbol{r},t) &= \sum_{j=1}^{N} m_j \delta(\boldsymbol{r}-\boldsymbol{r}_j(t)),\\ \hat{\boldsymbol{j}}(\boldsymbol{r},t) &= \sum_{j=1}^{N} m_j \delta\boldsymbol{v}_j(t)\delta(\boldsymbol{r}-\boldsymbol{r}_j(t)),\end{aligned} \tag{5.1}$$

with Fourier components

$$\begin{aligned}\rho_{\boldsymbol{k}}(t) &= \sum_{j=1}^{N} m_j \exp(-i\boldsymbol{k}\cdot\boldsymbol{r}_j(t)),\\ \boldsymbol{j}_{\boldsymbol{k}}(t) &= \sum_{j=1}^{N} m_j \delta\boldsymbol{v}_j(t)\exp(-i\boldsymbol{k}\cdot\boldsymbol{r}_j(t)),\end{aligned} \tag{5.2}$$

where $\delta\boldsymbol{v}_j(t) = \boldsymbol{v}_j(t) - \dot{\gamma}y_j(t)\boldsymbol{e}_x$ is the velocity deviations relative to mean Couette flow of the particle j. Each Fourier component of the current can be separated into the longitudinal part $\boldsymbol{j}_{l\boldsymbol{k}}$ and the transverse part $\boldsymbol{j}_{t\boldsymbol{k}}$ as

$$\begin{aligned}\boldsymbol{j}_{l\boldsymbol{k}}(t) &= (\hat{\boldsymbol{k}}\cdot\boldsymbol{j}_{\boldsymbol{k}}(t))\hat{\boldsymbol{k}},\\ \boldsymbol{j}_{t\boldsymbol{k}}(t) &= \boldsymbol{j}_{\boldsymbol{k}}(t) - (\hat{\boldsymbol{k}}\cdot\boldsymbol{j}_{\boldsymbol{k}}(t))\hat{\boldsymbol{k}},\end{aligned} \tag{5.3}$$

where $\hat{\boldsymbol{k}} = \boldsymbol{k}/k$ is the unit vector in $\boldsymbol{k}$ direction. The longitudinal component $\boldsymbol{j}_{l\boldsymbol{k}}$ is related to the mass density $\rho_{\boldsymbol{k}}$ via the continuity equation:

$$\frac{d\rho_{\boldsymbol{k}(-t)}(t)}{dt} + i\boldsymbol{k}(-t)\cdot\boldsymbol{j}_{l\boldsymbol{k}(-t)}(t) = 0, \tag{5.4}$$

where $\boldsymbol{k}(t)$ is the time-dependent wave vector [90] defined as

$$\boldsymbol{k}(t) = \boldsymbol{k} + \dot{\gamma}tk_x\boldsymbol{e}_y, \tag{5.5}$$

and $\boldsymbol{e}_y$ is the unit vector in y direction.

Then, the correlation functions of the density $\rho_{\boldsymbol{k}}(t)$, the longitudinal current $\boldsymbol{j}_{l\boldsymbol{k}}(t)$, and the transverse current $\boldsymbol{j}_{t\boldsymbol{k}}(t)$ are defined as

$$\begin{aligned}F(\boldsymbol{k},t) &= \frac{1}{N}\left\langle \rho_{\boldsymbol{k}(-t)}(t)\rho_{-\boldsymbol{k}}(0)\right\rangle,\\ C_l(\boldsymbol{k},t) &= \frac{k(-t)k(0)}{N}\left\langle \boldsymbol{j}_{l\boldsymbol{k}(-t)}(t)\cdot\boldsymbol{j}_{l-\boldsymbol{k}}(0)\right\rangle,\\ C_t(\boldsymbol{k},t) &= \frac{k(-t)k(0)}{N}\left\langle \boldsymbol{j}_{t\boldsymbol{k}(-t)}(t)\cdot\boldsymbol{j}_{t-\boldsymbol{k}}(0)\right\rangle.\end{aligned} \tag{5.6}$$

We also define the Fourier transforms of the correlation functions as

$$\begin{aligned}S(\boldsymbol{k},\omega) &= \frac{1}{2\pi}\int_{-\infty}^{\infty} F(\boldsymbol{k},t)\exp(i\omega t)dt,\\ C_l(\boldsymbol{k},\omega) &= \frac{1}{2\pi}\int_{-\infty}^{\infty} C_l(\boldsymbol{k},t)\exp(i\omega t)dt,\\ C_t(\boldsymbol{k},\omega) &= \frac{1}{2\pi}\int_{-\infty}^{\infty} C_t(\boldsymbol{k},t)\exp(i\omega t)dt.\end{aligned} \tag{5.7}$$

The function $S(\boldsymbol{k},\omega)$ is the so-called dynamical structure factor [53]. The density correlation function and the longitudinal current correlation function are related through the continuity equation (5.4) and comparable with each other:

$$\begin{aligned} \frac{d^2F(\boldsymbol{k},t)}{dt^2} &= -C_l(\boldsymbol{k},t), \\ \omega^2 S(\boldsymbol{k},\omega) &= C_l(\boldsymbol{k},\omega). \end{aligned} \tag{5.8}$$

We are able to examine the behaviors of the longitudinal and transverse sound waves by means of the current spectra $C_l(\boldsymbol{k},\omega)$ and $C_t(\boldsymbol{k},\omega)$, respectively. The behaviors of the sound waves are characterized by the dispersion relations and the sound attenuations, which can be both evaluated by means of $C_l(\boldsymbol{k},\omega)$ and $C_t(\boldsymbol{k},\omega)$ [53; 63]. As we mentioned, we focus on the transverse sound wave in the present study.

5.3 Results

5.3.A Acoustic properties in equilibrium state

We first examined the behavior of the transverse sound wave in the quiescent equilibrium state. Figures 5.1 show the Fourier transform $C_t(\boldsymbol{k},\omega)$ of the transverse current autocorrelation function. The temperatures are $T = 0.772$, 0.306, 0.289, and 267. In Fig. 5.1, $C_t(\boldsymbol{k},\omega)$ is normalized by the value $C_t(\boldsymbol{k},t=0)$. We can clearly recognize the peak line in the region between the wavenumber $k = 0$ and 3 for the transverse current spectrum. This peak line gives the dispersion relationship [53; 63]. From Fig. 5.1, the dispersion relationship is well approximated by $\omega = c_s k$, i.e., the linear relationship, at the small wavenumbers k (long distance scales). In addition to the dispersion relationship, we can also calculate the inverse of the attenuation time constant τ_k from the half-width of the peak value of the current spectrum. Note that the attenuation coefficient Γ_k is defined as τ_k^{-1} divided by k^2. These two quantities, the dispersion relationship and the attenuation time constant, describe the characteristics of plane wave propagating through materials. We have to mention that several studies [62; 64; 83; 96] found the finite size effects in the β relaxation regime, i.e., the time region at which the sound wave propagate. They have found the artificial oscillating behaviors of the density correlation functions in *ortho*−terphenyl [83], amorphous SiO_2 [64], and two dimensional soft-sphere liquid [62; 96]. However, in the present study, we used three dimensional soft-sphere liquid, as described in Sec. 5.2, and found no finite size effects or no artificial oscillations. Therefore, our results were not influenced by finite size effects and produced the physically correct behavior of the sound wave.

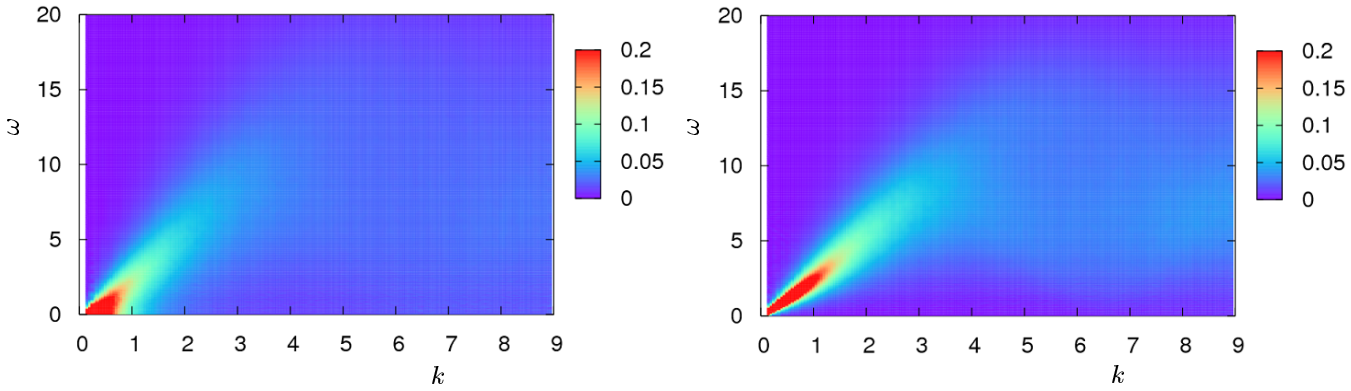

(a) $C_t(k,\omega)/C_t(k,t=0)$ at $T = 0.772$

(b) $C_t(k,\omega)/C_t(k,t=0)$ at $T = 0.306$

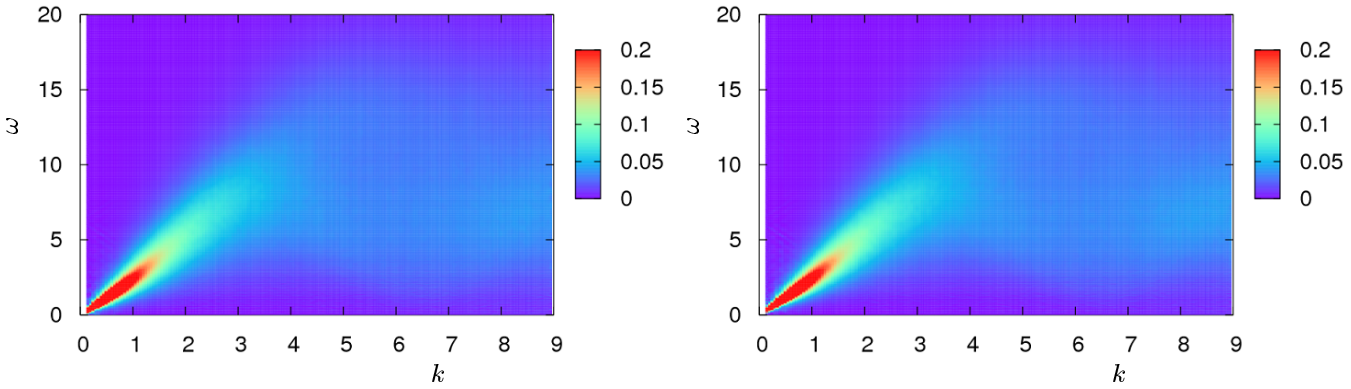

(c) $C_t(k,\omega)/C_t(k,t=0)$ at $T = 0.289$

(d) $C_t(k,\omega)/C_t(k,t=0)$ at $T = 0.267$

Figure 5.1: The Fourier transform $C_t(k,\omega)$ of the transverse current autocorrelation function. $C_t(k,\omega)$ is normalized by $C_t(k,t=0)$. The temperature T is 0.772 in (a), 0.306 in (b), 0.289 in (c), and 0.267 in (d).

We show the dispersion relationship $\omega = \omega(k)$ of the transverse sound wave in Fig. 5.2. The straight line $\omega = c_s k$ can be clearly fitted at low wavenumbers k. This linear relationship is characteristic of the dispersion relationship of phonons in crystalline structures. Therefore, the sound speed c_s can be determined from the gradient of the linear relationship [53; 63]. At low temperatures $T = 0.306 - 0.267$, the sound speed c_s is nearly constant, $c_s \simeq 2.4$, which agree with the previous result [63]. As we mentioned previously, the transverse sound wave cannot exist in liquids at short wavenumbers k and low frequencies ω. In fact, the transverse dispersion relation $\omega = \omega(k)$ starts from the finite wavenumber k, which is clearly recognized at the high temperature $T = 0.772$, i.e., the transverse dispersion relation starts from around $k = 0.4$ (see Fig. 5.2(a)). It has to be noted that several studies [50; 51; 52; 112; 130] performed normal mode analysis on quenched amorphous solids and examined the dispersion relationships of the sound waves. In Ref.

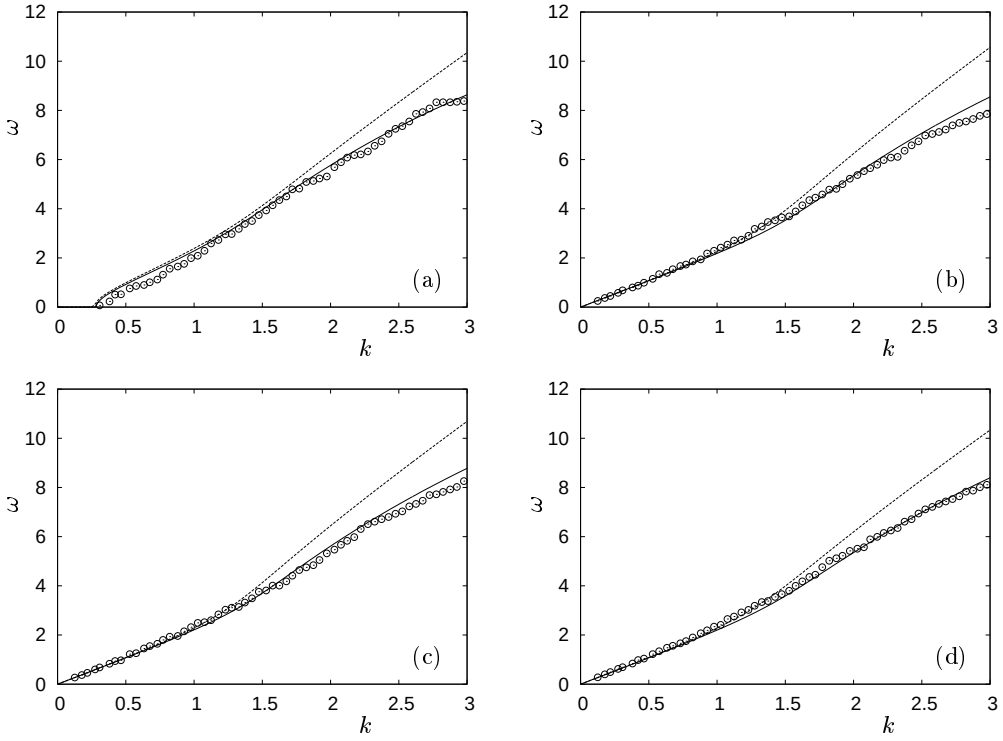

Figure 5.2: The dispersion relation $\omega = \omega(k)$ of the transverse sound wave. The temperature T is (a) 0.772, (b) 0.306, (c) 0.289, and (d) 0.267. The circles represent simulation results. The dashed line and the solid line are predictions of the continuum mechanics (see text in Sec. 5.3.C).

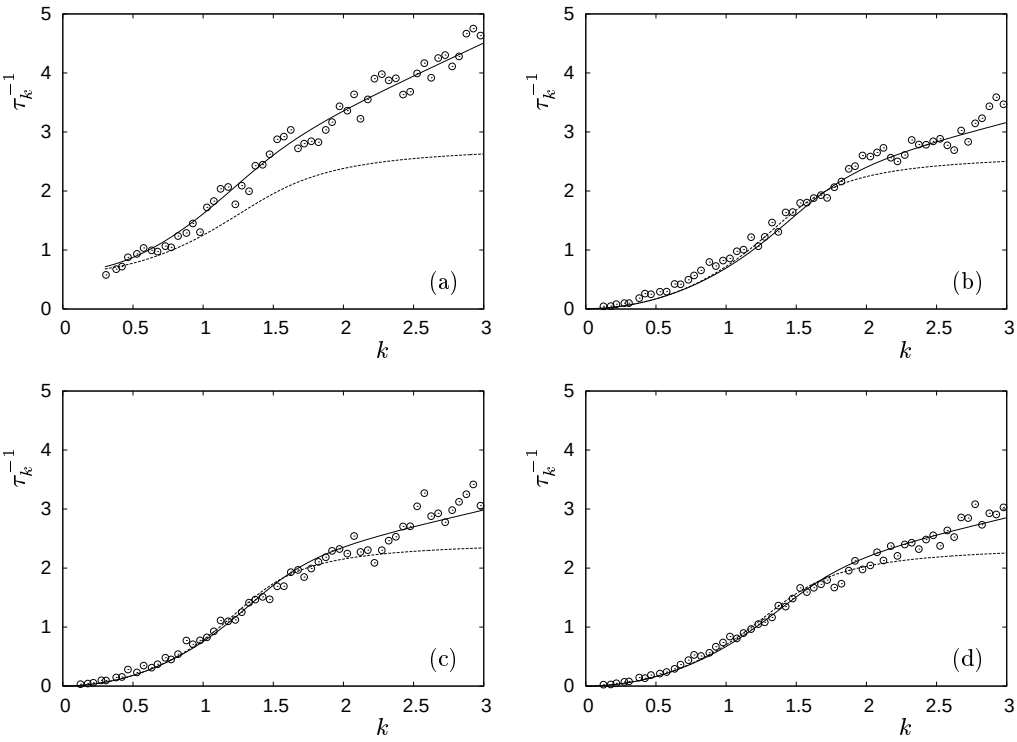

Figure 5.3: The inverse τ_k^{-1} of the sound attenuation time constant versus the wavenumber k. The temperature T is (a) 0.772, (b) 0.306, (c) 0.289, and (d) 0.267. The circles represent simulation results. The dashed line and the solid line are predictions of the continuum mechanics (see text in Sec. 5.3.C).

[130], normal mode analysis was performed on the same model liquid as the present one. Our results are quite similar as these results of quenched amorphous solids except that the transverse dispersion relation starts from the finite wavenumber k in supercooled liquids and the zero wavenumber $k = 0$ in amorphous solids, since the quenched amorphous solids can support the transverse sound wave to propagate in the hydrodynamic limit $k \to 0$ similar to the crystalline solids.

Figure 5.3 shows the wavenumber k dependence of the inverse τ_k^{-1} of the attenuation time constant. In the supercooled state $T = 0.306-0.267$, the value τ_k^{-1} is very small at low wavenumbers k (long distance scales), as in Fig. 5.3. This is due to the viscoelastic property of the supercooled liquid. The large structural relaxation time supports the transverse sound wave to propagate for long distances. On the other hand, at large wavenumbers k (short distance scales), τ_k^{-1} becomes large, so the transverse sound modes with large wavenumbers attenuate fast. As we mentioned, the previous study [130] examined the behaviors of the sound waves in the quenched amorphous solids by using the same model liquid as ours. According to Ref. [130] and our results, not only the sound speed but also the attenuation time constant of the transverse sound wave have quite similar values in the quenched amorphous solid and the supercooled liquid, interestingly. Thus, the transverse sound wave propagates in the same way through the amorphous solid and the supercooled liquid.

5.3.B Acoustic properties in sheared non-equilibrium state

Next, we investigated the acoustic properties of the supercooled liquid in the sheared non-equilibrium state. Figures 5.4 shows the Fourier transform $C_t(\boldsymbol{k}, \omega)$ of the transverse current autocorrelation function in the sheared non-equilibrium state. It has to be stressed that the function $C_t(\boldsymbol{k}, \omega)$ is almost independent of the direction of the wave vector $\boldsymbol{k}$ even in the sheared situation. The function $C_t(\boldsymbol{k}, \omega)$ generally depends on the direction of $\boldsymbol{k}$ under sheared condition. However, we numerically checked that even in the strongly sheared state, the current correlation function $C_t(\boldsymbol{k}, t)$ does not depend on the direction of $\boldsymbol{k}$ within numerical errors, i.e., $C_t(\boldsymbol{k}, t)$ is isotropic with respect to $\boldsymbol{k}$. Similar isotropic natures were already found in the density correlation functions and the mean square displacements [17; 90; 131]. We also checked such the isotropy in the longitudinal current correlation function $C_l(\boldsymbol{k}, t)$. Thus, we conclude that the Fourier transforms $C_l(\boldsymbol{k}, \omega)$ and $C_t(\boldsymbol{k}, \omega)$ of $C_l(\boldsymbol{k}, t)$ and $C_t(\boldsymbol{k}, t)$ are also isotropic with respect to $\boldsymbol{k}$, which means that the acoustic properties of supercooled liquids are isotropic even under the sheared situation.

Owing to the isotropic natures, we were able to plot $C_t(\boldsymbol{k}, \omega)$ as function of the wavenumber

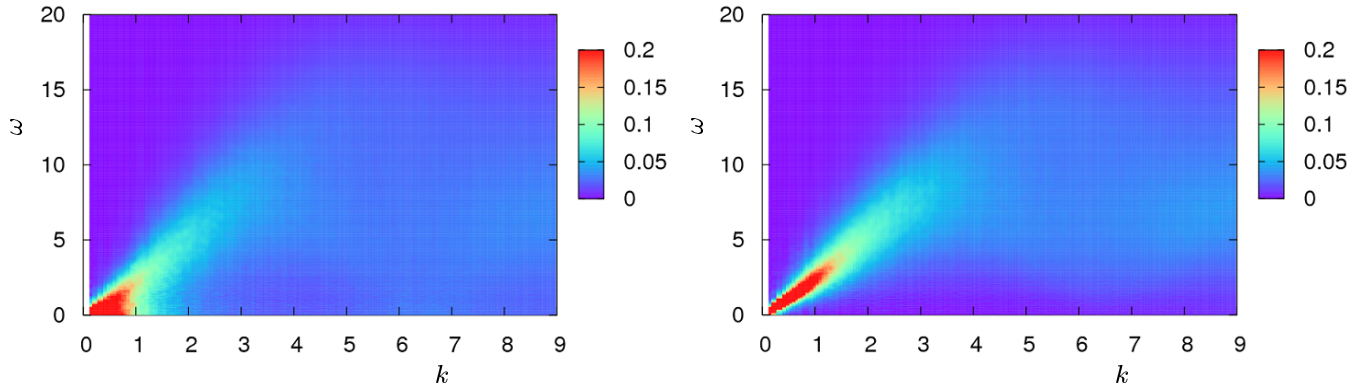

(a) $C_t(k,\omega)/C_t(k,t=0)$ at $\dot{\gamma}=10^{-1}$

(b) $C_t(k,\omega)/C_t(k,t=0)$ at $\dot{\gamma}=10^{-3}$

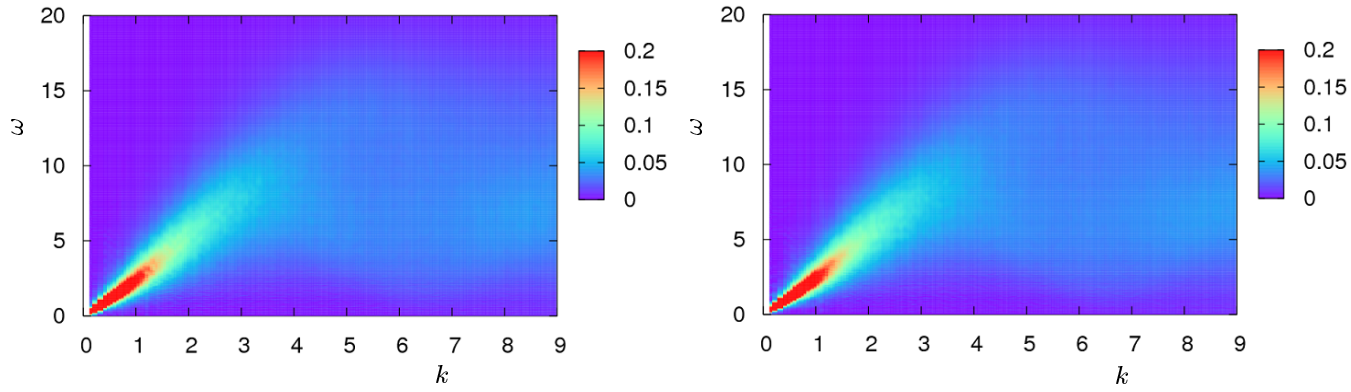

(c) $C_t(k,\omega)/C_t(k,t=0)$ at $\dot{\gamma}=10^{-4}$

(d) $C_t(k,\omega)/C_t(k,t=0)$ at $\dot{\gamma}=10^{-5}$

Figure 5.4: The Fourier transform $C_t(k,\omega)$ of the transverse current autocorrelation function. $C_t(k,\omega)$ is normalized by $C_t(k,t=0)$. The shear rate $\dot{\gamma}$ is 10^{-1} in (a), 10^{-3} in (b), 10^{-4} in (c), and 10^{-5} in (d).

k, instead of the wave vector $\boldsymbol{k}$, in Fig. 5.4. As in the equilibrium case, we can easily recognize the locations of the peaks in the region between the wavenumber $k=0$ and 3, which leads to the dispersion relationship $\omega=\omega(k)$. The inverse τ_k^{-1} of the attenuation time constant can be also calculated from the half-width of the peak value of the current spectrum. Figures 5.5 and 5.6 show the dispersion relationship $\omega=\omega(k)$ and the inverse τ_k^{-1} of the attenuation time constant, respectively. The temperature is $T=0.267$, and the shear rates are $\dot{\gamma}=10^{-1}$, $\dot{\gamma}=10^{-3}$, $\dot{\gamma}=10^{-4}$, and 10^{-5}. At the shear rates $\dot{\gamma}=10^{-3}-10^{-5}$, the sound speed c_s, calculated from the slop of the dispersion relation at low wavenumbers k, is nearly constant, $c_s\simeq 2.4$, which is the same value as in the equilibrium state. The sound speed is therefore nearly independent of not only the temperature T but also the shear rate $\dot{\gamma}$ at low temperatures and low shear rates. Comparing Figs. 5.5 and 5.6 with Figs. 5.2 and 5.3, we can see that both the dispersion relationship and the attenuation

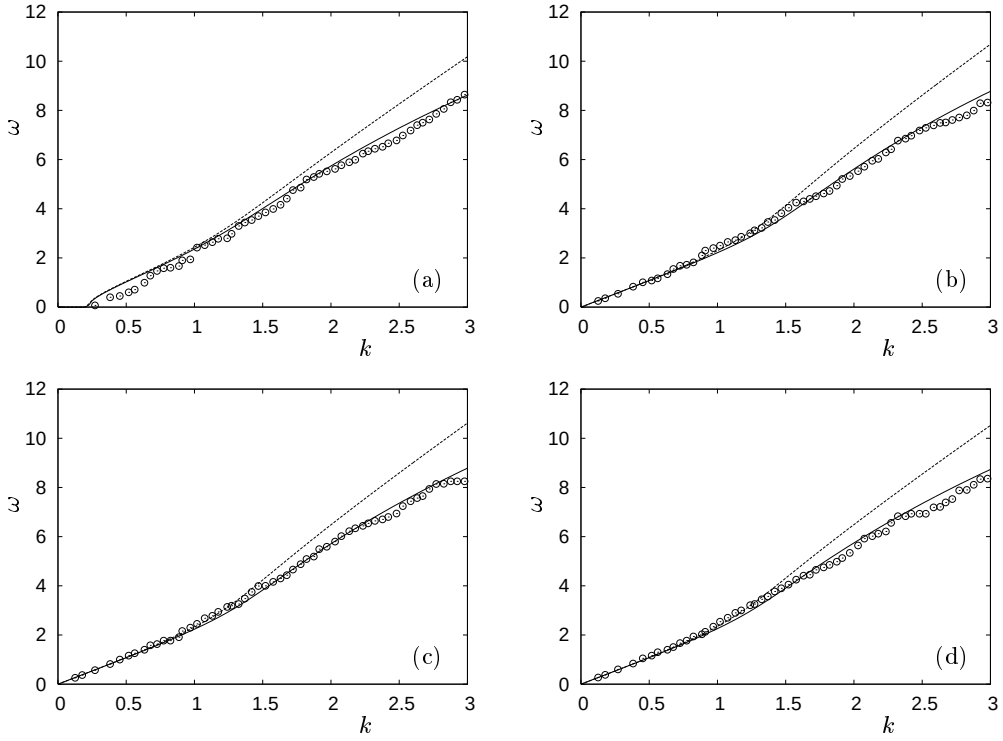

Figure 5.5: The dispersion relation $\omega = \omega(k)$ of the transverse sound wave. The temperature is $T = 0.267$. The shear rate $\dot{\gamma}$ is (a) 10^{-1}, (b) 10^{-3}, (c) 10^{-4}, and (d) 10^{-5}. The circles represent simulation results. The dashed line and the solid line are predictions of the continuum mechanics (see text in Sec. 5.3.C).

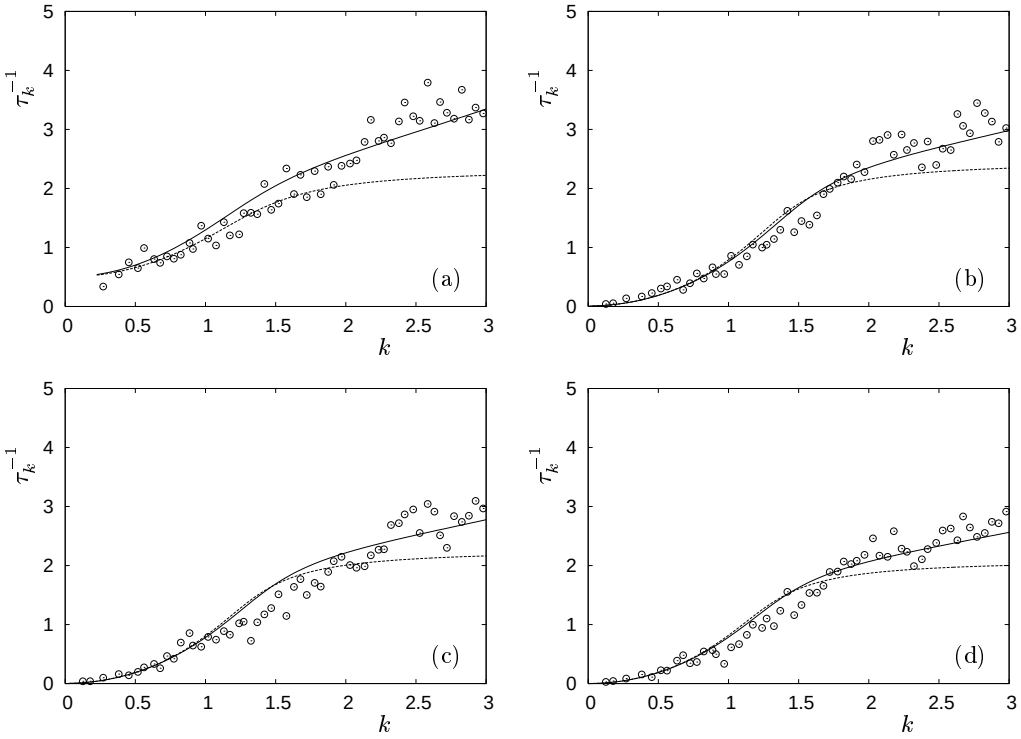

Figure 5.6: The inverse τ_k^{-1} of the sound attenuation time constant versus the wavenumber k. The temperature is $T = 0.267$. The shear rate $\dot{\gamma}$ is (a) 10^{-1}, (b) 10^{-3}, (c) 10^{-4}, and (d) 10^{-5}. The circles represent simulation results. The dashed line and the solid line are predictions of the continuum mechanics (see text in Sec. 5.3.C).

time constant under the strong shear flow ($\dot{\gamma} = 10^{-1}$) are similar to those in the high temperature state $T = 0.772$ rather than in the low temperature states $T = 0.306 - 0.267$. In addition, it is clearly observed that the transverse dispersion relation starts from the finite wavenumber around $k = 0.3$ at the high shear rate case $\dot{\gamma} = 0.1$, which is similar to the result of $T = 0.772$ in Fig. 5.2(a). Thus, due to the shear flow, the acoustic properties become close to those with the higher temperature. This result may have things common with the concept of an effective temperature [13; 56; 78; 100; 135]: the sheared non-equilibrium state can be described by the equilibrium state with the higher temperature, denoted as the effective temperature T_{eff}.

5.3.C Prediction of continuum mechanics

In this section, we examined the behavior of the transverse sound wave by means of the continuum mechanics. In our previous study [94] (Chapter 4), we successfully constructed the following two-mode Maxwell model equation (see Eqs. (4.5) and (4.6) in Chapter 4):

$$\begin{aligned} \boldsymbol{\sigma}_\alpha + \tau_\alpha \frac{d\boldsymbol{\sigma}_\alpha}{dt} &= \eta_\alpha \dot{\boldsymbol{\gamma}}, \\ \boldsymbol{\sigma}_\beta + \tau_\beta \frac{d\boldsymbol{\sigma}_\beta}{dt} &= \eta_\beta \dot{\boldsymbol{\gamma}}, \end{aligned} \tag{5.9}$$

where $\boldsymbol{\sigma} = \boldsymbol{\sigma}_\alpha + \boldsymbol{\sigma}_\beta$ is the stress tensor, and $\boldsymbol{\gamma}$ is the strain tensor. Note that $\boldsymbol{\sigma}_\alpha$ and $\boldsymbol{\sigma}_\beta$ are a slower component and a faster component of the stress tensor. Here, we neglect the nonlinear effect, i.e., we set the parameters τ_α and η_α to be constant, because the sound wave can be examined by the linearized equation. We can use the same constitutive equation (5.9) even for the sheared non-equilibrium situation by setting τ_α and η_α to be values in the sheared state. In the present work, the continuum mechanics approach was taken by using the constitutive equation (5.9). We assumed that the transverse sound wave propagates in the y direction. The displacement vector has only the x component, u_x, and the strain tensor has only xy component, $\gamma^{xy} = \partial u_x / \partial y$. The stress tensor has only the xy component due to the strain γ^{xy}. In the following, we denote the x component of the displacement vector as u and the xy component of the stress tensor as $\sigma = \sigma_\alpha + \sigma_\beta$. Then, the linearized continuum equation of the momentum is written as:

$$\begin{aligned} \rho \frac{\partial^2 u}{\partial t^2} &= \frac{\partial (\sigma_\alpha + \sigma_\beta)}{\partial y}, \\ \sigma_\alpha + \tau_\alpha \frac{\partial \sigma_\alpha}{\partial t} &= \eta_\alpha \frac{\partial^2 u}{\partial t \partial y}, \\ \sigma_\beta + \tau_\beta \frac{\partial \sigma_\beta}{\partial t} &= \eta_\beta \frac{\partial^2 u}{\partial t \partial y}, \end{aligned} \tag{5.10}$$

where ρ is the mass density. We are able to examine the behavior of the transverse sound wave in both the equilibrium state and the sheared non-equilibrium state by using the equation (5.10). To solve the equation (5.10), the form of the solution was set as

$$\begin{aligned} u(t,y) &= u_0(k,\tilde{\omega})\exp(i(ky-\tilde{\omega}t)), \\ \sigma_\alpha(t,y) &= \sigma_{\alpha 0}(k,\tilde{\omega})\exp(i(ky-\tilde{\omega}t)), \\ \sigma_\beta(t,y) &= \sigma_{\beta 0}(k,\tilde{\omega})\exp(i(ky-\tilde{\omega}t)). \end{aligned} \tag{5.11}$$

This solution means the propagating wave with the wavenumber k. The value $\tilde{\omega}$ is generally the complex number, and the real part and the imaginary part of $\tilde{\omega}$ mean the frequency and the attenuation rate of the wave, respectively. When we substituted the equation (5.11) into the equation (5.10), then the following cubic equation regarding $\tilde{\omega}$ was obtained:

$$\tilde{\omega}^3 + i\left(\frac{1}{\tau_\alpha}+\frac{1}{\tau_\beta}\right)\tilde{\omega}^2 - \left(\frac{1}{\tau_\alpha\tau_\beta}+\frac{G_\infty}{\rho}k^2\right)\tilde{\omega} - i\left(\frac{\eta}{\tau_\alpha\tau_\beta\rho}k^2\right) = 0, \tag{5.12}$$

where $G_\infty = \dfrac{\eta_\alpha}{\tau_\alpha}+\dfrac{\eta_\beta}{\tau_\beta}$ is the instantaneous shear modulus, and $\eta = \eta_\alpha + \eta_\beta$ is the shear viscosity [94]. The cubic equation (5.12) regarding $\tilde{\omega}$ has the three solutions $\tilde{\omega} = a - ib,\ a + ib$, and $-ic$, where a, b, and c are real numbers. The first two solutions $\omega = a \pm ib$ indicates the transverse sound wave, and a and b are the frequency and the attenuation rate, respectively. Thus, the dispersion relation and the sound attenuation time constant are written as $\omega = a(k)$ and $\tau_k = b(k)^{-1}$.

The equation (5.12) can be considered to have four parameters τ_α, $G_\alpha = \eta_\alpha/\tau_\alpha$, τ_β, and $G_\beta = \eta_\beta/\tau_\beta$. Note that G_α is the so called plateau modulus [48]. According to Ref. [47; 48], these four parameters can depend on the wavenumber k (distance scale). However, we first set these parameters to be constant. Parameters were set to be values at the wavenumber $k = 0$, indicated by the arrows in Figs. 5.7 and 5.8. Note that the values, τ_α, G_α, τ_β, and G_β, were determined as fitting parameters in this study, however, they are comparable with values determined in our previous study [94] (Chapter 4) as well as in Refs. [47; 48]. Figures 5.2 and 5.3 show the results of the continuum mechanics in the quiescent equilibrium situation by the dashed lines. Comparing the symbols (simulations) and the dashed lines (continuum mechanics), we easily see that the continuum mechanics catch the simulation results well at the small wavenumbers k (long distance scale). This makes sense since the continuum descriptions are exact at the hydrodynamic limit $k \ll 1$. At low temperatures $T = 0.306 - 0.267$, the dispersion relation is predicted as $\omega = \sqrt{G_\alpha/\rho}k$ at small wavenumbers k and low frequencies ω, which means that the sound speed is determined by the plateau modulus G_α, not by the instantaneous shear modulus G_∞. On the other hand, at high

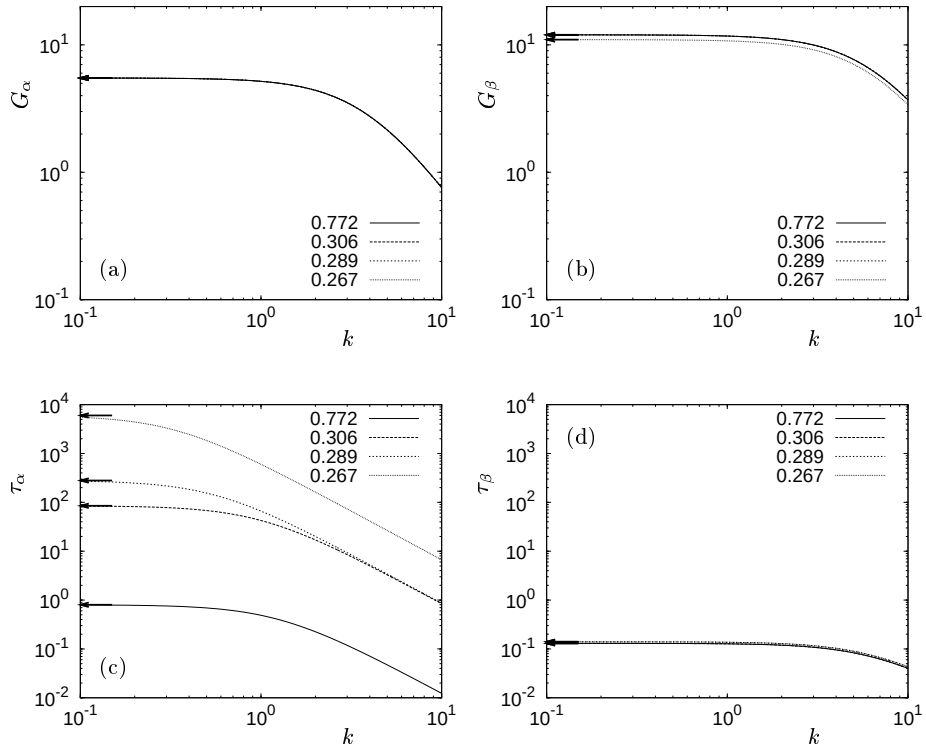

Figure 5.7: The wavenumber dependences of the parameters, τ_α, G_α, τ_β, and G_β, in the equilibrium state: (a) G_α, (b) G_β, (c) τ_α, and (d) τ_β. The temperatures are $T = 0.772,\ 0.306,\ 0.289$, and 0.267. The arrows indicate the values at the wavenumber $k = 0$.

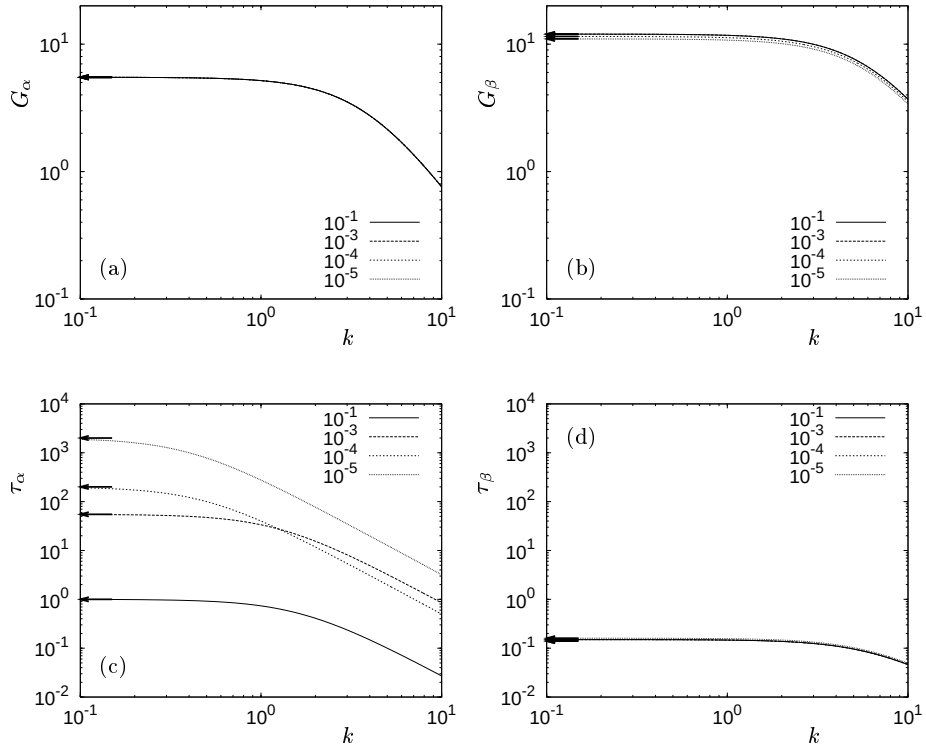

Figure 5.8: The wavenumber dependences of the parameters, τ_α, G_α, τ_β, and G_β, in the sheared non-equilibrium state: (a) G_α, (b) G_β, (c) τ_α, and (d) τ_β. The temperature is $T = 0.267$, and the shear rates are $\dot{\gamma} = 10^{-1},\ 10^{-3},\ 10^{-4}$, and 10^{-5}. The arrows indicate the values at the wavenumber $k = 0$.

wavenumbers k and high frequencies ω, the continuum mechanics predict the dispersion relation $\omega = \sqrt{G_\infty/\rho}k$. As in Fig. 5.2, the slope of the dispersion relation changes around $k \simeq 1.5$ at low temperatures $T = 0.306 - 0.267$. This tendency is consistent with simulation results, although the results of the simulations and the continuum mechanics do not coincide quantitatively with each other. At large wavenumbers k and high frequencies ω, the instantaneous shear modulus G_∞ determines the sound speed instead of the plateau modulus G_α. Furthermore, in the supercooled states $T = 0.306 - 0.267$, the inverse τ_k^{-1} of the sound attenuation time constant is quite small at small wavenumbers k, as shown in Fig. 5.3. This is due to the large relaxation time τ_α. In fact, the inverse of the sound attenuation time constant is predicted as $\tau_k^{-1} \simeq (2\tau_\alpha)^{-1}$ at $k \ll 1$. As the wavenumber k gets large, τ_k^{-1} increases since the relaxation time change from the larger τ_α to the smaller τ_β. At large wavenumbers k, the continuum mechanics predict $\tau_k^{-1} \simeq (2\tau_\beta)^{-1}\left(1 - \dfrac{G_\alpha}{G_\infty}\right)$ which is quite larger than $(2\tau_\alpha)^{-1}$. Simulation results exhibit the same tendency as the continuum mechanics. In addition to the equilibrium situation, we can consider the transverse sound wave in the sheared non-equilibrium situation in the same way. Figures 5.5 and 5.6 show the results of the continuum mechanics in the sheared non-equilibrium situation. The continuum mechanics catch the simulation results at low wavenumbers k even in the sheared state. As we explained above, the continuum mechanics predict well simulation results. However, there are some quantitative differences between simulation results and continuum mechanics at large wavenumbers k. To solve the discrepancies, we next considered the wavenumber dependences of the four parameters, τ_α, G_α, τ_β, and G_β.

Before going further, we examined the maximum length scale that the transverse mode exists, which is called as hydrodynamic length l_t [95]. As in Fig. 5.2, the dispersion relation starts from around $k = 0.4$ at the high temperature $T = 0.772$, whereas at low temperatures $T = 0.306 - 0.267$, the dispersion relation starts from nearly $k = 0$. Therefore, the hydrodynamic length l_t becomes very large at low temperatures, which is consistent with previous studies [2; 29; 30; 95]. Several works [68; 95; 105] suggested that the length l_t can be related to the size ξ of the cooperatively rearranging regions [1] or the heterogeneous dynamics [16]. However, the relationship between these two length scales l_t and ξ still remains elusive [68; 95]. We quantified the hydrodynamic length l_t by using the continuum mechanics, i.e., the equation (5.12), and l_t is predicted as $l_t \simeq 2\sqrt{G_\alpha/\rho}\tau_\alpha \sim \tau_\alpha$. The same result is predicted in the sheared situation. On the other hand, in our previous studies [92; 93], the correlation length ξ of the heterogeneous dynamics was estimated as

$\xi \sim \tau_\alpha^{0.1}$. Therefore, according to these results, we can conclude that two length scales l_t and ξ have no relationships with each other. The increase of the hydrodynamic length l_t is directly related to the slow dynamics, i.e., the increase of the relaxation time τ_α.

We next considered the wavenumber dependences of the four parameters, τ_α, G_α, τ_β, and G_β. As we explained, the results of the simulations (circles) and the continuum mechanics (dashed lines) are qualitatively same but quantitatively different at large wavenumbers k in Figs. 5.2, 5.3, 5.5, and 5.6. The recent study [47; 48] revealed that the shear viscosity and the shear modulus depend on the wavenumber k. It is therefore expected that the differences between the simulations and the continuum mechanics are due to lack of such the wavenumber dependences. In this study, we considered that the four parameters, τ_α, G_α, τ_β, and G_β, depend on the wavenumber k as the simple Ornstein-Zernike form:

$$\begin{aligned}
\tau_\alpha(k) &= \frac{\tau_{\alpha k0}}{1+k^2\xi_{\tau_\alpha}^2}, \\
G_\alpha(k) &= \frac{G_{\alpha k0}}{1+k^2\xi_{G_\alpha}^2}, \\
\tau_\beta(k) &= \frac{\tau_{\beta k0}}{1+k^2\xi_{\tau_\beta}^2}, \\
G_\beta(k) &= \frac{G_{\alpha k0}}{1+k^2\xi_{G_\beta}^2},
\end{aligned} \tag{5.13}$$

where ξ_{τ_α}, ξ_{G_α}, ξ_{τ_β}, and ξ_{G_β} are the length scales for τ_α, G_α, τ_β, and G_β, respectively. This dependent form was found in Refs. [47; 48]. Note that the values $\eta_\alpha(k)$ and $\eta_\beta(k)$ are written as $\eta_\alpha(k) = G_\alpha(k)\tau_\alpha(k)$ and $\eta_\beta(k) = G_\beta(k)\tau_\beta(k)$, respectively. To set the parameters, τ_α, G_α, τ_β, and G_β, as in Eq. (5.13) means to extend the constitutive equation (5.9) to the finite wavenumber case as follows:

$$\begin{aligned}
\boldsymbol{\sigma}_\alpha(k) + \tau_\alpha(k)\frac{d\boldsymbol{\sigma}_\alpha(k)}{dt} &= \eta_\alpha(k)\dot{\boldsymbol{\gamma}}(k), \\
\boldsymbol{\sigma}_\beta(k) + \tau_\beta(k)\frac{d\boldsymbol{\sigma}_\beta(k)}{dt} &= \eta_\beta(k)\dot{\boldsymbol{\gamma}}(k),
\end{aligned} \tag{5.14}$$

where $\boldsymbol{\sigma}(k) = \boldsymbol{\sigma}_\alpha(k) + \boldsymbol{\sigma}_\beta(k)$ is the Fourier component of the stress tensor, and $\boldsymbol{\gamma}$ is the Fourier component of the strain tensor.

Figures 5.7 and 5.8 show the wavenumber dependences of τ_α, G_α, τ_β, and G_β that we considered in the present study. The values of τ_β and G_β characterizing the faster component of the constitutive equation (5.9) depend weakly on the wavenumber k. The plateau modulus G_α also exhibit weak dependence, which was demonstrated in Refs. [47; 48]. Compared with G_α, τ_β, and G_β, the value τ_α depend on the wavenumber k strongly. We note that τ_α is different from the so-called α-relaxation time determined from the density correlation functions, although both are comparable

at small wavenumbers k. We determined the dispersion relation and the sound attenuation time constant by solving the equation (5.12) with Eq. (5.13). Figures 5.2 and 5.3 shows the results by the solid lines, which coincide well with the simulation results even at large wavenumbers k. In addition, the results for the sheared non-equilibrium situation are also shown in Figs. 5.5 and 5.6, which demonstrate that the predictions of the continuum mechanics are also quantitatively same as the simulation results. Therefore, we can conclude that the continuum mechanics approach with the wavenumber dependences of the shear viscosity and modulus predicts the behavior of the transverse sound wave well even at large wavenumbers (short wavelengths). Our result indicates that the wavenumber dependences of the shear viscosity and the shear modulus can be observed in the propagation of the sound waves with short wavelengths.

5.4 Conclusion

In this work, we examined the transverse sound wave propagating through the supercooled liquid in not only the quiescent equilibrium state but also the sheared non-equilibrium state. We used two methods: MD simulations and the continuum mechanics. Here, the continuum mechanics were used with the two-mode Maxwell model equation [94] which can describe the mechanical properties of the supercooled liquid well (as shown in Chapter 4). The results of the simulations and the continuum mechanics coincide well with each other, and therefore, continuum mechanics allowed us to explain physically the behavior of the transverse sound wave. The continuum mechanics can predict the transverse sound mode even in the sheared non-equilibrium case in the same way as the equilibrium case. The shear flow makes the acoustic properties become close to those with the higher temperature, which may have things common with the concept of an effective temperature [13].

The behavior of the transverse sound wave is characterized by the dispersion relation $\omega = \omega(k)$ and the sound attenuation time constant τ_k. At small wavenumbers and low frequencies, the dispersion relation is written as $\omega = \sqrt{G_\alpha/\rho}k$, which indicates that the sound speed is $c_s = \sqrt{G_\alpha/\rho}$ and is determined by the plateau modulus G_α rather than the instantaneous modulus G_∞. As the wavenumber gets large, the slope of the dispersion relation, i.e., the sound speed, changes from $c_s = \sqrt{G_\alpha/\rho}$ to $\sqrt{G_\infty/\rho}$, so the sound speed is determined by the instantaneous modulus G_∞ at large wavenumbers. The inverse τ_k^{-1} of the attenuation time constant is very small at small wavenumbers. This means that the transverse sound wave attenuate very slowly and propagate

for long distances, which results from the large relaxation time τ_α of the supercooled liquid. In contrast, τ_k^{-1} is large at large wavenumbers, so the transverse sound wave decays fast. This is due to the small relaxation time τ_β. As the wavenumber and the frequency increase, the relaxation time changes from the slower time τ_α to the faster time τ_β, which leads to the increase of the attenuation rate. Furthermore, by using the continuum mechanics, we also estimated the hydrodynamic length l_t as the maximum wavelength that the transverse mode can exist [95]. We obtained $l_t \sim \tau_\alpha$, which means that l_t is directly related to the slow dynamics, i.e., the increase of the relaxation time τ_α, and has no relation with the correlation length of the cooperatively rearranging regions [1] or the heterogeneous dynamics [16].

At large wavenumbers, the effects of the wavenumber dependences of the shear viscosity and the shear modulus [47; 48] were observed. By considering the wavenumber-dependent shear viscosity and shear modulus, the continuum mechanics can describe quantitatively quite well the behavior of the transverse sound wave even with large wavenumbers and high frequencies. The shear viscosity and the shear modulus decrease with increasing the wavenumber [47; 48]. Due to the decrease of the shear modulus, the slope of the dispersion relation decreases at large wavenumbers, i.e., the sound speed decreases. The decrease of the shear viscosity causes the increase of the attenuation rate (the inverse τ_k^{-1} of the sound attenuation) and makes the transverse sound mode decay faster. Supercooled liquids exhibit the nonlocal nature of viscous transport similar to complex fluids such as entangled polymer solutions [43; 44; 45]. Our results revealed that the effects of such nonlocality can be observed in the propagation of the transverse sound wave with small wavelengths and high frequencies.

Chapter 6

General conclusion

Molecular dynamics simulations were performed on a supercooled model liquid in three dimensions, and extensive and long-duration trajectory data were obtained. By using the trajectory data, the dynamical properties of the supercooled liquid were investigated: the dynamical heterogeneities (**Chapter 2** and **3**), the mechanical properties (**Chapter 4**), and the acoustic properties (**Chapter 5**). The supercooled liquid can be driven into the non-equilibrium state by applying a steady shear flow. In addition to the quiescent equilibrium state, such the sheared non-equilibrium state was also considered to broadly understand the dynamical properties of the supercooled liquid.

In **Chapter 2**, the dynamical heterogeneity in the equilibrium situation was investigated. The property of dynamical heterogeneity can be characterized by three quantities: the correlation length $\xi_4(t)$, the intensity $\chi_4(t)$, and the lifetime $\tau_{\mathrm{hetero}}(t)$. Using a single order parameter representing particle dynamics and its correlation functions, all three quantities were consistently evaluated in two time intervals $t = \tau_\alpha$ (the α-relaxation time) and τ_{ngp} (the time at which the non-Gaussian parameter $\alpha_2(t)$ of the Van Hove self-correlation function is maximized). As the temperature T decreased, the lifetime $\tau_{\mathrm{hetero}}(t)$ increased dramatically, whereas the correlation length $\xi_4(t)$ and the intensity $\chi_4(t)$ increased slowly or reached a plateau compared with $\tau_{\mathrm{hetero}}(t)$. For the time interval $t = \tau_\alpha$, $\chi_4(\tau_\alpha) \sim \xi_4(\tau_\alpha)^{3.2}$ and $\tau_{\mathrm{hetero}}(\tau_\alpha) \sim \xi_4(\tau_\alpha)^{10.8}$ or $\tau_{\mathrm{hetero}}(\tau_\alpha) \sim \exp(k\xi_4(\tau_\alpha)^{1.3})$ were obtained as the scaling relationships between the three quantities: $\xi_4(\tau_\alpha)$, $\chi_4(\tau_\alpha)$, and $\tau_{\mathrm{hetero}}(\tau_\alpha)$. Furthermore, the lifetime $\tau_{\mathrm{hetero}}(t)$ was investigated in further detail. Examination of the time-interval t dependence of the lifetime $\tau_{\mathrm{hetero}}(t)$ resulted in the following relationship: as the time interval t increased, $\tau_{\mathrm{hetero}}(t)$ monotonically became longer and reached a plateau at the relaxation time of the two-point density correlation function. At the large time intervals where $\tau_{\mathrm{hetero}}(t)$ reached a plateau, the heterogeneities were greatly weakened, and the heterogeneous dynamics migrated in space with a diffusion mechanism like that of the particle density.

In **Chapter 3**, the dynamical heterogeneity in the sheared non-equilibrium state was examined. Extension of the correlation functions of the particle dynamics (the four-point correlation functions), which were used in **Chapter 2**, was performed to the sheared condition. The three quantities (the

correlation length $\xi_4(t)$, the intensity $\chi_4(t)$, and the lifetime $\tau_{\mathrm{hetero}}(t)$) were quantified by using the extended correlation functions and the method similar to that applied in **Chapter 2**. Two time intervals ($t = \tau_\alpha$ and τ_{ngp}) were used to define the local dynamics. All three quantities decreased as the shear rate $\dot{\gamma}$ of the steady shear flow increased. For the time interval $t = \tau_\alpha$, the three quantities were found to decrease according to $\xi_4(\tau_\alpha) \sim \dot{\gamma}^{-0.08}$, $\chi_4(\tau_\alpha) \sim \dot{\gamma}^{-0.26}$, and $\tau_{\mathrm{hetero}}(\tau_\alpha) \sim \dot{\gamma}^{-0.88}$. The steady shear flow suppressed the heterogeneous structure as well as the lifetime of the dynamical heterogeneity. In addition, the results indicated that the α-relaxation time τ_α dependencies of the three quantities coincided with those under the equilibrium conditions. For the time interval of $t = \tau_\alpha$, the scaling relationships in both the equilibrium and the non-equilibrium states were the same. This discovery means that all three quantities that characterize the dynamical heterogeneity can be mapped onto the corresponding values in the equilibrium state through the α-relaxation time τ_α.

In **Chapter 4**, the shear stress responses and fluctuations in the quiescent equilibrium state and the sheared non-equilibrium state were examined. Even in the strongly sheared state, the supercooled liquid exhibited surprisingly simple shear stress responses to oscillating shear strains, which were well described by a simple constitutive equation, i.e., a two-mode Maxwell model equation. The same responses and fluctuation correlations were obtained for the components that differed from that of the driving shear flow, which demonstrates the highly isotropic feature of supercooled liquids. In contrast, for the same component as that of the driving shear flow, the responses and the fluctuations were significantly different from those of the other components, which demonstrates the anisotropic feature of supercooled liquids. Furthermore, a violation of the fluctuation-dissipation theorem was examined, and the concept of an effective temperature was tested. The results indicated that the use of only one effective temperature cannot completely characterize the relationship between the response functions and the correlation functions. Further improvement and modification was required, which resulted in the concept of an effective temperature. In this work, supercooled liquids were demonstrated to have simple non-equilibrium mechanical properties that are never observed in typical complex fluids in which the driving shear flow induces anisotropic dynamics or a structural change.

In **Chapter 5**, the behavior of the transverse sound wave in the equilibrium state and the sheared non-equilibrium state were investigated by two methods: MD simulations and the continuum mechanics. Here, the continuum mechanics were applied with the two-mode Maxwell model

equation which is the constitutive equation constructed in **Chapter 4**. The results of the simulations and the continuum mechanics coincided quantitatively well with each other in both the equilibrium state and the sheared non-equilibrium state. It is therefore possible to explain physically the behavior of the transverse sound wave in the framework of the continuum mechanics. The transverse sound wave showed the two propagation modes due to the two modes of the constitutive equation. At large wavelengths and low frequencies, the transverse sound wave decayed very slowly and propagated for long distances, and its sound speed was determined by the plateau modulus G_α. On the other hand, at short wavelengths and high frequencies, the transverse mode attenuated fast, and its sound speed was controlled by the instantaneous shear modulus G_∞. Furthermore, it was demonstrated that the nonlocal nature of the viscous transport, i.e., the wavenumber dependences of the shear viscosity and the shear modulus, makes effects on the behavior of the transverse sound wave with short wavelengths and high frequencies.

Two major topics were the focus of this dissertation. The first topic was growing length and time scales in supercooled liquids, which was examined in **Chapter 2** and **3**. Although the glass transition is distinct from the critical phenomenon, there are some phenomenological analogies between the glass transition and the critical phenomenon [16; 37; 131]. In the critical phenomenon, the length and time scales diverge as the temperature T approaches the critical point T_c. Therefore, similar to the critical phenomenon, there may exist the length and time scales in the glass transition phenomenon, which diverge as the temperature T reaches the glass transition point T_g. As the growing time scale, the α-relaxation time τ_α is well known. In **Chapter 2**, the correlation length ξ_4 and the lifetime τ_{hetero} were successfully extracted from the dynamical heterogeneities as the growing length scale and time scale, respectively. Both the length scale ξ_4 and the time scale τ_{hetero} increased as the temperature T decreased. In addition, in **Chapter 3**, the length scale ξ_4 and the time scale τ_{hetero} in the sheared non-equilibrium situation were successfully extracted. The scaling relation between the length scale ξ_4 and the time scale τ_{hetero}, similar to the critical phenomenon, were obtained. Interestingly, the same scaling relation was observed in the sheared non-equilibrium state. Note that the hydrodynamic length l_t obtained in **Chapter 5** was directly associated with the slow dynamics, i.e., the structural relaxation time τ_α, so the two length scales ξ_4 and l_t have no relation with each other. According to the results, the dynamical heterogeneity is expected to influence the drastic change of the dynamics due to decreased temperatures and increased shear rates. However, the role of the dynamical heterogeneity in the dynamics change

or the glass transition remains unclear and elusive. In addition, there is still no proper theory to bridge between an increased length scale (ξ_4) and increased time scales ($\tau_{\rm hetero}$ and τ_α).

The second topic focused upon in this thesis is non-equilibrium properties, which were investigated in **Chapter 3**, **4**, and **5**. Understanding the non-equilibrium properties of supercooled liquids is important for not only a broader understanding of the glass transition phenomenon and but also non-equilibrium statistical mechanics. A steady shear flow can drive supercooled liquids into the non-equilibrium state. The mechanical and acoustic properties of the supercooled liquids were found to be highly isotropic regardless of such the anisotropic situation (**Chapter 4** and **5**). The validity of the mapping concept was also numerically demonstrated: the quantities in the sheared non-equilibrium state were mapped onto those in the equilibrium state through the α-relaxation time τ_α. The mapping concept is valid for a wide range of quantities: the viscosity η, the diffusion constant D [131; 132], the correlation length ξ_4, the intensity χ_4, and the lifetime $\tau_{\rm hetero}$ of the dynamical heterogeneity (**Chapter 3**). The constitutive Eq. (4.5) and Eq. (4.6) (**Chapter 4**), describing the mechanical properties of supercooled liquids, were also mapped through τ_α. Furthermore, the dispersion relation and the attenuation time constant of the transverse sound wave (**Chapter 5**) can also be mapped because they can be derived from the constitutive Eq. (4.5) and Eq. (4.6) in both the equilibrium state and the sheared non-equilibrium state. Therefore, the mapping concept can be applied to a variety of situations for the dynamical heterogeneities, the mechanical properties, and the acoustic properties. The results regarding the isotropy and the mapping concept demonstrated the simple non-equilibrium properties of the supercooled liquid, which are characteristic of supercooled liquids and are not observed in typical complex fluids, such as polymeric solutions. The isotropy and the mapping concept also support strongly the concept of an effective temperature: the effective temperature $T_{\rm eff}$ plays a role as the temperature T in the non-equilibrium situation. The results of the mapping concept suggest that the α-relaxation time τ_α can behave similarly to the temperature-like role in the non-equilibrium situation. However, there are also difficulties and problems regarding scalar mapping, which are described as follows. Anisotropies were detected in the four-point correlation functions [46] and the stress correlation fluctuations (**Chapter 4**), although the supercooled liquids hardly show any anisotropy in the density correlation functions and the mean square displacement [17; 90; 131] as well as the current correlation functions (**Chapter 5**). This observation indicates that the non-equilibrium state cannot be completely mapped on the equilibrium state. Furthermore, it was reported that the effective

temperature T_{eff}, which was evaluated from the response and correlation functions, can depend on the observable [13; 56; 78; 100; 135]. It was also found that one effective temperature cannot completely characterize the relationships between the stress response functions and the stress correlation functions (**Chapter 4**). Therefore, further investigations are required for the mapping concept and the concept of an effective temperature and to understand the non-equilibrium properties of the supercooled liquids.

The dynamics of supercooled liquids and the related phenomena of the glass transition have been the focus of research and of great importance for many years. However, many of the phenomena are still under discussion. The author hopes that this work will contribute to the understanding of the mechanism of the glass transition and development of the physics of glass.

Bibliography

1. G. Adam and J. H. Gibbs, On the temperature dependence of cooperative relaxation properties in glass-forming liquids, *J. Chem. Phys.* **43**, 139 (1965).

2. R. Ahluwalia and S. P. Das, Growing length scale related to the solidlike behavior in a supercooled liquid, *Phys. Rev. E* **57**, 5771 (1998).

3. M. P. Allen and D. J. Tildesley, *Computer Simulation of Liquids*, Oxford University Press, Oxford (1986).

4. C. A. Angell, Structural instability and relaxation in liquid and glassy phases near the fragile liquid limit, *J. Non-Cryst. Solids* **102**, 205 (1988).

5. C. A. Angell, Relaxation in liquids, polymers and plastic crystals - strong/fragile patterns and problems, *J. Non-Cryst. Solids* **131-133**, 13 (1991).

6. C. A. Angell, K. L. Ngai, G. B. McKenna, P. F. McMillan, and S. W. Martin, Relaxation in glassforming liquids and amorphous solids, *J. Appl. Phys.* **88**, 3113 (2000).

7. M. Baiesi, E. Boksenbojm, and B. Wynants, Nonequilibrium linear response for markov dynamics, ii: Inertial dynamics, *J. Stat. Phys.* **139**, 492 (2010).

8. M. Baiesi, C. Maes, and B. Wynants, Nonequilibrium linear response for markov dynamics, i: Jump processes and overdamped diffusions, *J. Stat. Phys.* **137**, 1094 (2009).

9. R. Böhmer, G. Hinze, G. Diezemann, B. Geil, and H. Sillescu, Dynamic heterogeneity in supercooled ortho-terphenyl studied by multidimensional deuteron nmr, *Europhys. Lett.* **36**, 55 (1996).

10. B. Bernu, J. P. Hansen, Y. Hiwatari, and G. Pastore, Soft-sphere model for the glass transition in binary alloys: Pair structure and self-diffusion, *Phys. Rev. A* **36**, 4891 (1987).

11. B. Bernu, Y. Hiwatari, and J. P. Hansen, A molecular dynamics study of the glass transition in binary mixtures of soft spheres, *J. Phys. C: Solid State Phys.* **18**, L371 (1985).

12. L. Berthier, Time and length scales in supercooled liquids, *Phys. Rev. E* **69**, 020201(R) (2004).

13. L. Berthier and J.-L. Barrat, Nonequilibrium dynamics and fluctuation-dissipation relation in a sheared fluid, *J. Chem. Phys.* **116**, 6228 (2002).

14. L. Berthier, J.-L. Barrat, and J. Kurchan, A two-time-scale, two-temperature scenario for nonlinear rheology, *Phys. Rev. E* **61**, 5464 (2000).

15. L. Berthier, G. Biroli, J. P. Bouchaud, L. Cipelletti, D. El Masri, D. L'Hote, F. Ladieu, and M. Pierno, Direct experimental evidence of a growing length scale accompanying the glass transition, *Science* **310**, 1797 (2005).

16. L. Berthier, G. Biroli, J.-P. Bouchaud, L. Cipelletti, and W. van Saarloos, *Dynamical Heterogeneities in Glasses, Colloids, and Granular Media*, Oxford University Press, Oxford (2011).

17. R. Besseling, E. R. Weeks, A. B. Schofield, and W. C. K. Poon, Three-dimensional imaging of colloidal glasses under steady shear, *Phys. Rev. Lett.* **99**, 028301 (2007).

18. R. B. Bird, R. C. Armstrong, and O. Hassager, *Dynamics of polymetric liquids*, volume 1, John Wiley and Sons, New York, second edition (1987).

19. R. B. Bird, W. E. Stewart, and E. N. Lightfoot, *Transport Phenomena*, John Wiley and Sons, New York, second edition (2002).

20. G. Biroli and J. P. Bouchaud, Diverging length scale and upper critical dimension in the mode-coupling theory of the glass transition, *Europhys. Lett.* **67**, 21 (2004).

21. G. Biroli, J. P. Bouchaud, K. Miyazaki, and D. R. Reichman, Inhomogeneous mode-coupling theory and growing dynamic length in supercooled liquids, *Phys. Rev. Lett.* **97**, 195701 (2006).

22. E. Bouchbinder and J. S. Langer, Shear-transformation-zone theory of linear glassy dynamics, *Phys. Rev. E* **83**, 061503 (2011).

23. J. M. Brader, M. SiebenbKürger, M. Ballauff, K. Reinheimer, M. Wilhelm, S. J. Frey, F. Weysser, and M. Fuchs, Nonlinear response of dense colloidal suspensions under oscillatory shear: Mode-coupling theory and fourier transform rheology experiments, *Phys. Rev. E* **82**, 061401 (2010).

24. A. Cavagna, Supercooled liquids for pedestrians, *Phys. Rep.* **476**, 51 (2009).

25. D. Chandler, J. P. Garrahan, R. L. Jack, L. Maibaum, and A. C. Pan, Lengthscale dependence of dynamic four-point susceptibilities in glass formers, *Phys. Rev. E* **74**, 051501 (2006).

26. R. Chetrite and K. Gawedzki, Eulerian and lagrangian pictures of non-equilibrium diffusions, *J. Stat. Phys.* **137**, 890 (2009).

27. J. Colmenero, F. Alvarez, and A. Arbe, Self-motion and the α relaxation in a simulated glass-forming polymer: Crossover from gaussian to non-gaussian dynamic behavior, *Phys. Rev. E* **65**, 041804 (2002).

28. C. Dalle-Ferrier, C. Thibierge, C. Alba-Simionesco, L. Berthier, G. Biroli, J. P. Bouchaud, F. Ladieu, D. L'Hôte, and G. Tarjus, Spatial correlations in the dynamics of glassforming liquids: Experimental determination of their temperature dependence, *Phys. Rev. E* **76**, 041510 (2007).

29. S. P. Das, Dynamic length scales and feedback from long-time structural relaxation in a simple liquid, *J. Phys.: Condens. Matter* **12**, 6423 (2000).

30. S. P. Das, Elastic behavior in a supercooled liquid: Analysis of viscoelasticity using an extended mode coupling model, *Phys. Rev. E* **62**, 1670 (2000).

31. P. G. de Gennes, Liquid dynamics and inelastic scattering of neutrons, *Physica (Amsterdam)* **25**, 825 (1959).

32. P. G. Debenedetti and F. H. Stillinger, Supercooled liquids and the glass transition, *Nature (London)* **410**, 259 (2001).

33. B. Doliwa and A. Heuer, Cooperativity and spatial correlations near the glass transition: Computer simulation results for hard spheres and disks, *Phys. Rev. E* **61**, 6898 (2000).

34. B. Doliwa and A. Heuer, How do dynamic heterogeneities evolve in time?, *J. Non-Cryst. Solids* **307-310**, 32 (2002).

35. C. Donati, J. F. Douglas, W. Kob, S. J. Plimpton, P. H. Poole, and S. C. Glotzer, Stringlike cooperative motion in a supercooled liquid, *Phys. Rev. Lett.* **80**, 2338 (1998).

36. M. D. Ediger, Spatially heterogeneous dynamics in supercooled liquids, *Annu. Rev. Phys. Chem.* **51**, 99 (2000).

37. M. D. Ediger, C. A. Angell, and S. R. Nagel, Supercooled liquids and glasses, *J. Phys. Chem.* **100**, 13200 (1996).

38. P. A. Egelstaff, *An Introduction to the Liquid State*, Academic, London (1967).

39. D. J. Evans and G. Morriss, *Statistical Mechanics of Nonequilibrium Liquids*, Cambridge university press, New York, second edition (2008).

40. E. Flenner and G. Szamel, Lifetime of dynamic heterogeneities in a binary lennard-jones mixture, *Phys. Rev. E* **70**, 052501 (2004).

41. E. Flenner and G. Szamel, Dynamic heterogeneity in a glass forming fluid: Susceptibility, structure factor, and correlation length, *Phys. Rev. Lett.* **105**, 217801 (2010).

42. E. Flenner, M. Zhang, and G. Szamel, Analysis of a growing dynamic length scale in a glass-forming binary hard-sphere mixture, *Phys. Rev. E* **83**, 051501 (2011).

43. A. Furukawa, Dynamic critical phenomena of polymer solutions, *J. Phys. Soc. Jpn.* **72**, 1436 (2003).

44. A. Furukawa, Viscoelastic effect on hydrodynamic relaxation in polymer solutions, *J. Phys. Soc. Jpn.* **72**, 209 (2003).

45. A. Furukawa, Microrheology of entangled polymer solutions, *J. Chem. Phys.* **121**, 9716 (2004).

46. A. Furukawa, K. Kim, S. Saito, and H. Tanaka, Anisotropic cooperative structural rearrangements in sheared supercooled liquids, *Phys. Rev. Lett.* **102**, 016001 (2009).

47. A. Furukawa and H. Tanaka, Nonlocal nature of the viscous transport in supercooled liquids: Complex fluid approach to supercooled liquids, *Phys. Rev. Lett.* **103**, 135703 (2009).

48. A. Furukawa and H. Tanaka, Direct evidence of heterogeneous mechanical relaxation in supercooled liquids, *Phys. Rev. E* **84**, 061503 (2011).

49. S. C. Glotzer, Spatially heterogeneous dynamics in liquids: insights from simulation, *J. Non-Cryst. Solids* **274**, 342 (2000).

50. G. S. Grest, S. R. Nagel, and A. Rahman, Longitudinal and transverse excitations in a glass, *Phys. Rev. Lett.* **49**, 1271 (1982).

51. J. Hafner, Diffuse umklapp scattering in amorphous metals, *J. Phys. C: Solid State Phys.* **14**, L287 (1981).

52. J. Hafner and M. Krajci, Propagating and localized vibrational modes in ni-zr glasses, *J. Phys.: Condens. Matter* **6**, 4631 (1994).

53. J. P. Hansen and I. R. McDonald, *Theory of Simple Liquids*, Academic, London, third edition (2006).

54. T. Harada and S.-I. Sasa, Equality connecting energy dissipation with a violation of the fluctuation-response relation, *Phys. Rev. Lett.* **95**, 130602 (2005).

55. G. Harrison, *The Dynamic Properties of Supercooled Liquids*, Academic, New York (1976).

56. T. K. Haxton and A. J. Liu, Activated dynamics and effective temperature in a steady state sheared glass, *Phys. Rev. Lett.* **99**, 195701 (2007).

57. C. Heussinger, L. Berthier, and J-L. Barrat, Superdiffusive, heterogeneous, and collective particle motion near the fluid-solid transition in athermal disordered materials, *Europhys. Lett.* **90**, 20005 (2010).

58. C. Heussinger, P. Chaudhuri, and J-L. Barrat, Fluctuations and correlations during the shear flow of elastic particles near the jamming transition, *Soft matter* **6**, 3050 (2010).

59. Y. Hiwatari, H. Matsuda, T. Ogawa, N. Ogita, and A. Ueda, Molecular dynamics studies on the soft-core model, *Prog. Theor. Phys.* **52**, 1105 (1974).

60. Y. Hiwatari, J. Matsui, T. Muranaka, and T. Odagaki, The applicability of the soft core model of fluids to dynamical properties of simple liquids —the velocity autocorrelation function—, *Prog. Theor. Phys.* **53**, 915 (1975).

61. Y. Hiwatari, J. Matsui, T. Muranaka, and T. Odagaki, Molecular dynamics studies of the low-temperature amorphous soft-core systems, *J. Phys. Soc. Jpn.* **47**, 733 (1979).

62. Y. Hiwatari, J. Matsui, T. Muranaka, and T. Odagaki, Slow dynamics in supercooled fluids, *J. Mol. Liquids* **65-66**, 123 (1995).

63. Y. Hiwatari and H. Miyakawa, Molecular dynamics study of binary alloys near the glass transition, *J. Non-Cryst. Solids* **117-118**, 862 (1990).

64. J. Horbach, W. Kob, and K. Binder, Finite size effects in simulations of glass dynamics, *Phys. Rev. E* **54**, R5897 (1996).

65. M. M. Hurley and P. Harrowell, Kinetic structure of a two-dimensional liquid, *Phys. Rev. E* **52**, 1694 (1995).

66. S. A. Hutcheson and G. B. McKenna, The measurement of mechanical properties of glycerol, *m*-toluidine, and sucrose benzoate under consideration of corrected rheometer compliance: An in-depth study and review, *J. Phys. Chem.* **129**, 074502 (2008).

67. T. Iwashita, T. Kumagai, and R. Yamamoto, A direct numerical simulation method for complex modulus of particle dispersions, *Eur. Phys. J. E* **32**, 357 (2010).

68. G. Johnson, A. I. Mel'cuk, H. Gould, W. Klein, and R. D. Mountain, Molecular-dynamics study of long-lived structures in a fragile glass-forming liquid, *Phys. Rev. E* **57**, 5707 (1998).

69. S. Karmakar, C. Dasgupta, and S. Sastry, Analysis of dynamic heterogeneity in a glass former from the spatial correlations of mobility, *Phys. Rev. Lett.* **105**, 015701 (2010).

70. S. Karmakar, C. Dasgupta, and S. Sastry, Comment on "scaling analysis of dynamic heterogeneity in a supercooled lennard-jones liquid", *Phys. Rev. Lett.* **105**, 019801 (2010).

71. W. K. Kegel and A. van Blaaderen, Direct observation of dynamical heterogeneities in colloidal hard-sphere suspensions, *Science* **287**, 290 (2000).

72. K. Kim and S. Saito, Multiple time scales hidden in heterogeneous dynamics of glass-forming liquids, *Phys. Rev. E* **79**, 060501(R) (2009).

73. K. Kim and S. Saito, Multi-time density correlation functions in glass-forming liquids: Probing dynamical heterogeneity and its lifetime, *J. Chem. Phys.* **133**, 044511 (2010).

74. K. Kim and S. Saito, Role of the lifetime of dynamical heterogeneity in the frequency-dependent stokes-einstein relation of supercooled liquids, *J. Phys. Soc. Jpn* **79**, 093601 (2010).

75. K. Kim and R. Yamamoto, Apparent finite-size effects in the dynamics of supercooled liquids, *Phys. Rev. E* **61**, R41 (2000).

76. W. Kob and H. C. Andersen, Testing mode-coupling theory for a supercooled binary lennard-jones mixture i: The van hove correlation function, *Phys. Rev. E* **51**, 4626 (1995).

77. W. Kob and H. C. Andersen, Testing mode-coupling theory for a supercooled binary lennard-jones mixture. ii. intermediate scattering function and dynamic susceptibility, *Phys. Rev. E* **52**, 4134 (1995).

78. M. Krüger and M. Fuchs, Nonequilibrium fluctuation-dissipation relations of interacting brownian particles driven by shear, *Phys. Rev. E* **81**, 011408 (2010).

79. S. Kämmerer, W. Kob, and R. Schilling, Test of mode coupling theory for a supercooled liquid of diatomic molecules. i. translational degrees of freedom, *Phys. Rev. E* **58**, 2131 (1998).

80. N. Lačević, F. W. Starr, T. B. Schrøder, and S. C. Glotzer, Spatially heterogeneous dynamics investigated via a time-dependent four-point density correlation function, *J. Chem. Phys.* **119**, 7372 (2003).

81. S. Léonard and L. Berthier, Lifetime of dynamic heterogeneity in strong and fragile kinetically constrained spin models, *J. Phys.: Condens. Matter* **17**, S3571 (2005).

82. R. G. Larson, *The Structure and Rheology of Complex Fluids*, Oxford University Press, Oxford (1999).

83. L. J. Lewis and G. Wahnström, Molecular-dynamics study of supercooled *ortho*-terphenyl, *Phys. Rev. E* **50**, 3865 (1994).

84. X. Li and S.-Q. Wang, Studying steady shear flow characteristics of entangled polymer solutions with parallel mechanical superposition, *Macromolecules* **43**, 5904 (2010).

85. A. J. Liu and S. R. Nagel, Nonlinear dynamics: Jamming is not just cool any more, *Nature* **396**, 21 (1998).

86. H. A. Makse and J. Kurchan, Testing the thermodynamic approach to granular matter with a numerical model of a decisive experiment, *Nature (London)* **415**, 614 (2002).

87. A. H. Marcus, J. Schofield, and S. A. Rice, Experimental observations of non-gaussian behavior and stringlike cooperative dynamics in concentrated quasi-two-dimensional colloidal liquids, *Phys. Rev. E* **60**, 5725 (1999).

88. K. Martens, E. Bertin, and M. Droz, Dependence of the fluctuation-dissipation temperature on the choice of observable, *Phys. Rev. Lett.* **103**, 260602 (2009).

89. H. Miyagawa and Y. Hiwatari, Molecular-dynamics study of the glass transition in a binary soft-sphere model, *Phys. Rev. A* **44**, 8278 (1991).

90. K. Miyazaki, D. R. Reichman, and R. Yamamoto, Supercooled liquids under shear: Theory and simulation, *Phys. Rev. E* **70**, 011501 (2004).

91. H. Mizuno and R. Yamamoto, Lifetime of dynamical heterogeneity in a highly supercooled liquid, *Phys. Rev. E* **82**, 030501(R) (2010).

92. H. Mizuno and R. Yamamoto, Dynamical heterogeneity in a highly supercooled liquid: Consistent calculations of correlation length, intensity, and lifetime, *Phys. Rev. E* **84**, 011506 (2011).

93. H. Mizuno and R. Yamamoto, Dynamical heterogeneity in a highly supercooled liquid under a sheared situation, *arXiv:1111.5912* (2011).

94. H. Mizuno and R. Yamamoto, Mechanical responses and stress fluctuations of a strongly sheared supercooled liquid, *arXiv:1108.4300* (2011).

95. R. D. Mountain, Length scales for fragile glass-forming liquids, *J. Chem. Phys.* **102**, 5408 (1995).

96. T. Muranaka and Y. Hiwatari, β relaxation in a highly supercooled state via molecular dynamics simulation, *Phys. Rev. E* **51**, R2735 (1995).

97. T. Narumi, S. V. Franklin, K. W. Desmond, M. Tokuyama, and E. R. Weeks, Spatial and temporal dynamical heterogeneities approaching the binary colloidal glass transition, *Soft matter* **7**, 1472 (2011).

98. K. N. Nordstrom, J. P. Gollub, and D. J. Durian, Dynamical heterogeneity in soft-particle suspensions under shear, *Phys. Rev. E* **84**, 021403 (2011).

99. C. S. O'Hern, A. J. Liu, and S. R. Nagel, Effective temperatures in driven systems: Static versus time-dependent relations, *Phys. Rev. Lett.* **93**, 165702 (2004).

100. I. K. Ono, C. S. O'Hern, D. J. Durian, S. A. Langer, A. J. Liu, and S. R. Nagel, Effective temperatures of a driven system near jamming, *Phys. Rev. Lett.* **89**, 095703 (2002).

101. A. Onuki, Phase transitions of fluids in shear flow, *J. Phys. Condens. Matter* **9**, 6119 (1997).

102. A. Onuki, *Phase Transition Dynamics*, Cambridge University Press, Cambridge, England (2002).

103. D. N. Perera and P. Harrowell, Consequences of kinetic inhomogeneities in glasses, *Phys. Rev. E* **54**, 1652 (1996).

104. D. N. Perera and P. Harrowell, Relaxation dynamics and their spatial distribution in a two-dimensional glass-forming mixture, *J. Chem. Phys.* **111**, 5441 (1999).

105. J. Petravic, Shear stress relaxation in liquids, *J. Chem. Phys.* **120**, 10188 (2004).

106. F. Q. Potiguar and H. A. Makse, Effective temperature and jamming transition in dense, gently sheared granular assemblies, *Eur. Phys. J. E* **19**, 171 (2006).

107. A. Rahman, Correlations in the motion of atoms in liquid argon, *Phys. Rev.* **136**, A405 (1964).

108. R. Richert, Heterogeneous dynamics in liquids: fluctuations in space and time, *J. Phys.: Condens. Matter* **14**, R703 (2002).

109. J. N. Roux, J. L. Barrat, and J. P. Hansen, Dynamical diagnostics for the glass transition in soft-sphere alloys, *J. Phys.: Condens. Matter* **1**, 7171 (1989).

110. E. Vidal Russell and N. E. Israeloff, Direct observation of molecular cooperativity near the glass transition, *Nature (London)* **408**, 695 (2000).

111. K. Schmidt-Rohr and H. W. Spiess, Nature of nonexponential loss of correlation above the glass transition investigated by multidimensional nmr, *Phys. Rev. Lett.* **66**, 3020 (1991).

112. H. R. Schober, Vibrations and relaxations in a soft sphere glass: boson peak and structure factors, *J. Phys.: Condens. Matter* **16**, S2659 (2004).

113. F. Sciortino, L. Fabbian, S. -H. Chen, and P. Tartaglia, Supercooled water and the kinetic glass transition. ii. collective dynamics, *Phys. Rev. E* **56**, 5397 (1997).

114. P. Sollich, Rheological constitutive equation for a model of soft glassy materials, *Phys. Rev. E* **58**, 738 (1998).

115. E. Somma, O. Valentino, G. Titomanlio, and G. Ianniruberto, Parallel superposition in entangled polydisperse polymer melts: Experiments and theory, *J. Rheol.* **51**, 987 (2007).

116. T. Speck and U. Seifert, Restoring a fluctuation-dissipation theorem in a nonequilibrium steady state, *Europhys. Lett.* **74**, 391 (2006).

117. R. S. L. Stein and H. C. Andersen, Scaling analysis of dynamic heterogeneity in a supercooled lennard-jones liquid, *Phys. Rev. Lett.* **101**, 267802 (2008).

118. G. Szamel and E. Flenner, Diverging length scale of the inhomogeneous mode-coupling theory: A numerical investigation, *Phys. Rev. E* **81**, 031507 (2010).

119. C. Toninelli, M. Wyart, L. Berthier, G. Biroli, and J. P. Bouchaud, Dynamical susceptibility of glass formers: Contrasting the predictions of theoretical scenarios, *Phys. Rev. E* **71**, 041505 (2005).

120. M. Tsamados, Plasticity and dynamical heterogeneity in driven glassy materials, *Eur. Phys. J. E* **32**, 165 (2010).

121. T. Uneyama, K. Horio, and H. Watanabe, Anisotropic mobility model for polymers under shear and its linear response functions, *Phys. Rev. E* **83**, 061802 (2011).

122. F. Varnik, Structural relaxation and rheological response of a driven amorphous system, *J. Chem. Phys.* **125**, 164514 (2006).

123. J. Vermant, L. Walker, P. Moldenears, and J. Mewis, Orthogonal versus parallel superposition measurements, *J. Non-Newtonian Fluid Mech.* **79**, 173 (1998).

124. C. H. Wang and Q. L. Liu, Rayleigh-brillouin scattering of transverse and longitudinal acoustic waves in a supercooled viscoelastic liquid, *J. Chem. Phys.* **78**, 4363 (1983).

125. C. Y. Wang and M. D. Ediger, How long do regions of different dynamics persist in supercooled *o*-terphenyl?, *J. Phys. Chem. B* **103**, 4177 (1999).

126. C. Y. Wang and M. D. Ediger, Lifetime of spatially heterogeneous dynamic domains in polystyrene melts, *J. Chem. Phys.* **112**, 6933 (2000).

127. E. R. Weeks, J. C. Crocker, A. C. Levitt, A. Schofield, and D. A. Weitz, Three-dimensional direct imaging of structural relaxation near the colloidal glass transition, *Science* **287**, 627 (2000).

128. A. Widmer-Cooper, P. Harrowell, and H. Fynewever, How reproducible are dynamic heterogeneities in a supercooled liquid?, *Phys. Rev. Lett.* **93**, 135701 (2004).

129. H. M. Wyss, K. Miyazaki, J. Mattsson, Z. Hu, D. R. Reichman, and D. A. Weitz, Strain-rate frequency superposition: A rheological probe of structural relaxation in soft materials, *Phys. Rev. Lett.* **98**, 238303 (2007).

130. R. Yamamoto and Y. Matsuoka, Dynamic heterogeneity in supercooled liquids studied by molecular dynamics, isoconfigurational ensemble, and normal mode analysis, *arXiv:0910.2535* (2009).

131. R. Yamamoto and A. Onuki, Dynamics of highly supercooled liquids: Heterogeneity, rheology, and diffusion, *Phys. Rev. E* **58**, 3515 (1998).

132. R. Yamamoto and A. Onuki, Heterogeneous diffusion in highly supercooled liquids, *Phys. Rev. Lett.* **81**, 4915 (1998).

133. S. Yasuda and R. Yamamoto, Rheological properties of polymer melt between rapidly oscillating plates: An application of multiscale modeling, *Europhys. Lett.* **86**, 18002 (2009).

134. S. Yasuda and R. Yamamoto, Multiscale modeling and simulation for polymer melt flows between parallel plates, *Phys. Rev. E* **81**, 036308 (2010).

135. M. Zhang and G. Szamel, Effective temperatures of a driven, strongly anisotropic brownian system, *Phys. Rev. E* **83**, 061407 (2011).

List of Publications

Chapter 2

Hideyuki Mizuno and Ryoichi Yamamoto, "Lifetime of dynamical heterogeneity in a highly supercooled liquid," *Phys. Rev. E* **82**, 030501(R) 1-4, (2010).

Hideyuki Mizuno and Ryoichi Yamamoto, "Dynamical heterogeneity in a highly supercooled liquid: Consistent calculations of correlation length, intensity, and lifetime," *Phys. Rev. E* **84**, 011506 1-11, (2011).

Chapter 3

Hideyuki Mizuno and Ryoichi Yamamoto, "Dynamical Heterogeneity in a Highly Supercooled Liquid under a Sheared Situation," *J. Chem. Phys.*, **submitted**.

Chapter 4

Hideyuki Mizuno and Ryoichi Yamamoto, "Mechanical Responses and Stress Fluctuations of a Strongly Sheared Supercooled Liquid," *Europhys. Lett.*, **to be published**.

Hideyuki Mizuno and Ryoichi Yamamoto, **in preparation**.

Chapter 5

Hideyuki Mizuno and Ryoichi Yamamoto, **to be submitted**.

Acknowledgements

First of all, I would like to express my deep gratitude to my supervisor Professor Ryoichi Yamamoto for his support and guidance and for letting me sample some of his great knowledge throughout my PhD course. I would also like to acknowledge Associate Professor Kunimasa Miyazaki, Dr. Kang Kim, Dr. Takuya Iwashita, Dr. Takashi Uneyama, Dr. Atsushi Ikeda, Mr. Takeshi Kuroiwa, and Associate Professor Shugo Yasuda for all their precious comments and advices.

I also want to thank my room-mate, Dr. Masayuki Uranagase, for his great kindness. I am indebted to Dr. Takahiro Murashima, Mr. Rei Tatsumi, and Mr. Shih Chun-Yu for daily lunch time. I am grateful to Mr. Adnan Hamid for daily coffee break. Thanks to them, I could enjoy my research life in the university.

In addition, I would like to show my sincerest appreciation to Ms. Misato Okumura, Mr. Hiroshi Yano, and Mr. Hirozumi Yoshida for their hearty help and encouragement. With their help, I could keep going forward. Finally, I wish to thank Ryoko Mizuno for being my sunshine whenever skies were gray.